UNIVERSITEIT VAN PRETORIA
UNIVERSITY OF PRETORIA
YUNIBESITHI YA PRETORIA

Department of Materials Science and Metallurgical Engineering

Back-annealing of hot dip galvanised strip steel microalloyed with vanadium

By

Johannes Sebastian Steyn

Supervised by Prof. Charles W Siyasiya

Co-supervised by Dr. Johan E Westraadt, Dr. Kevin M Banks and Prof. Roelf J Mostert

Submitted in partial fulfilment of the degree

Master of Engineering

in the Department of Materials Science and Metallurgical Engineering

Faculty of Engineering, Built Environment and Information Technology

University of Pretoria

Republic of South Africa

May 2024

Declaration by author

I Johannes Sebastian Steyn declare that this thesis, submitted in partial fulfilment of the requirements for the degree Master of Engineering (Metallurgical Engineering) from the University of Pretoria, is entirely my own work unless otherwise referenced or acknowledged. This document has not been submitted to any other academic institution for qualification.

Research outputs

STEYN Johannes Sebastian, BANKS Kevin Mark and SIYASIYA Charles Witness, “Back-Annealing of Hot Dip Galvanised Strip Steel Microalloyed with Vanadium”, THERMEC 2023 International Conference on Processing & Manufacturing of Advanced Materials Processing, Fabrication, Properties, Applications, 2 to 7 July 2023, Vienna, Austria.

J.S. Steyn, K.M. Banks, and C.W. Siyasiya. “Back-Annealing of Hot Dip Galvanised Strip Steel Microalloyed with Vanadium.” Materials Science Forum. Trans Tech Publications, Ltd., November 29, 2023.

Abstract

The steel market increasingly demands higher strength thinner products with reduced weight and decreased cost, in particular galvanised products for the roofing, automotive and solar industries, which are in high demand. A viable option to meet this demand is via back-annealing, also known as partial or recovery annealing, which consists of annealing cold-worked material at low temperatures. Back-annealing aims to only utilise the recovery process, i.e. to only restore a fraction of the elongation whilst retaining most of the strength obtained from cold-rolling. The targeted specification is EN 10346 S700GD, i.e. the desired properties are in the region of 800 MPa tensile strength and 10% total elongation. Therefore, the purpose of this study was to examine the viability of using V-N microalloying for high-strength recovery annealed steel.

In this work, back-annealing (recovery) was applied to heavily cold-worked low C-microalloyed V-N steels in an attempt to achieve a yield strength of 700 MPa and a minimum A80 elongation of 10%. Laboratory simulations of annealing during hot dip galvanising (HDG) were employed to compare recovery and recrystallisation kinetics of V-N, Nb-Ti and plain low C steel. Based on these results, industrial slabs were subjected to conventional hot rolling and back-annealing cycles during HDG. Precipitation in both V-N and Nb-Ti steels extended the back-annealing window by about 50 °C compared to low C steel. Initial hardening due to precipitation during annealing was observed in V-N and Nb-Ti steels. A temperature-time parameter M was used to compare the results. The M_{rs} (recrystallisation start) in both V-N and Nb-Ti steels was 20.1 compared to 18 in plain low C-Mn. The EN 10346 S700GD specification was achieved by subjecting low C-microalloyed V-N steel to low finishing rolling temperatures and coiling temperatures followed by back-annealing of the heavily cold-worked strip at an M value to prevent full recrystallisation. The V-N steel showed improved stability during annealing when compared to Nb-Ti, due to the unstable nature of the NbC precipitation during the back-annealing process. In other words, the V-N steel was found to be friendlier in terms of microstructural control in order to achieve consistent mechanical properties.

Acknowledgements

The author is grateful and would like to thank the following people and organisations:

- Vanitec and the University of Pretoria for financial support;
- Nelson Mandela University Centre for the HRTEM for electron microscopy work;
- Supervisor Prof. Charles Siyasiya for his guidance and knowledge;
- Co-supervisor Dr. Kevin Banks for constant motivation;
- Co-supervisor Dr. Johan Westraadt for the electron microscope work and teaching me many new concepts;
- Co-supervisor Prof. Roelf Mostert for his assistance with departmental administration and organising financial assistance;
- Industrial Minerals and Metals Research Institute (IMMRI) for the use of equipment
- Rorisang Maubane and Ruzanne Engelbreght from IMMRI for assistance with lab work, and Vinod Kurup for Thermo-Calc simulations;
- Line managers Frans Venter and Dirk Lourens at ArcelorMittal South Africa for their industrial knowledge and giving me time to work on my studies;
- My wife Lara for love, support and encouragement;
- My parents for making it all possible.

Contents

List of Figures

List of Tables

List of abbreviations

Abbreviation	Definition
ADF-STEM	annular dark field Scanning transmission electron microscopy
AsGG	abnormal subgrain growth
ASTM	American Society for Testing and Materials
BRT	bulk replication technique
BSE-SEM	back scatter electron scanning electron microscopy
EBSD	electron backscatter diffraction
ECCI	electron channelling contrast imaging
EFTEM	energy filtered transmission electron microscopy
FPPF	fundamental parameters line profile fitting
GNB	geometrically necessary dislocations
GOS	grain orientation spread
HAGB	high angle grain boundaries
HDG	hot dip galvanising
HR-EBSD	high resolution electron backscatter diffraction
HSLA	high strength low alloy
IDB	incidental dislocation boundaries
JMAK	Johnson-Mehl-Avrami-Kolmogorov
LAGB	low-angle grain boundaries
Nb(C,N)	niobium carbonitrides
NbC	niobium carbide
NIST	National Institute of Standards and Technology
PSN	particle-stimulated nucleation
SAE	Society of Automotive Engineers
SIBM	strain induced boundary migration
TEM	transmission electron microscopy
UTS	ultimate tensile strength
V(C,N)	vanadium carbonitrides
VC	vanadium carbide
XRD	X-ray diffraction

Chapter 1: Introduction

1.1 Background

Steel markets increasingly demand higher strength thinner products with reduced weight and decreased cost; in particular galvanised products for the roofing, automotive and solar industries, which are in high demand.

A viable option to meet this demand is via back-annealing, also known as partial or recovery annealing, which consists of annealing cold-worked material at low temperatures. Back-annealing aims to only utilise the recovery process, i.e. to only restore a fraction of the elongation whilst retaining most of the strength obtained from cold-rolling. Figure 1 shows various types of steels currently used in the automotive industry. The recovery annealed products fall in the region of 800 MPa tensile strength with 10% total elongation.

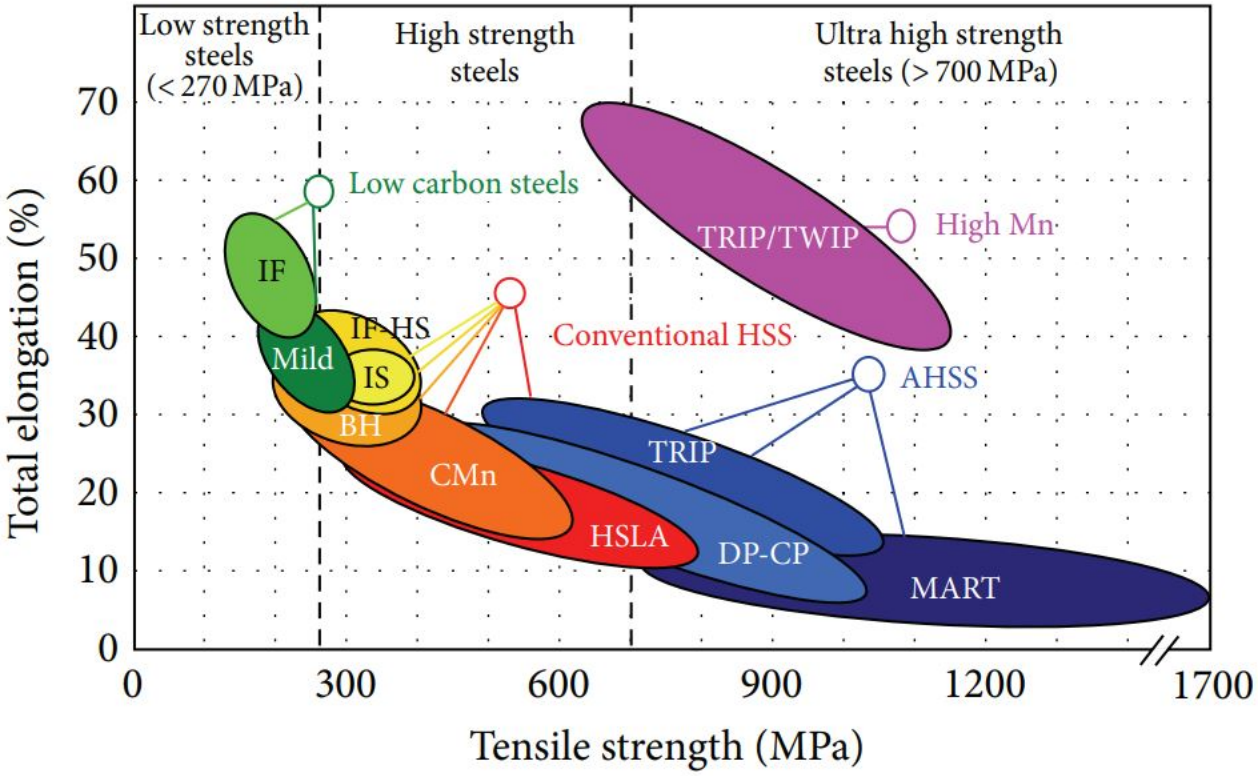

Figure 1: Strength and ductility of various types of steel in the automotive industry. [1]

The demand for spiral piping and simple construction beams for solar markets is driving research on weight reduction. The importance of increased strength while maintaining adequate ductility to form pipes is seen in Figure 2.

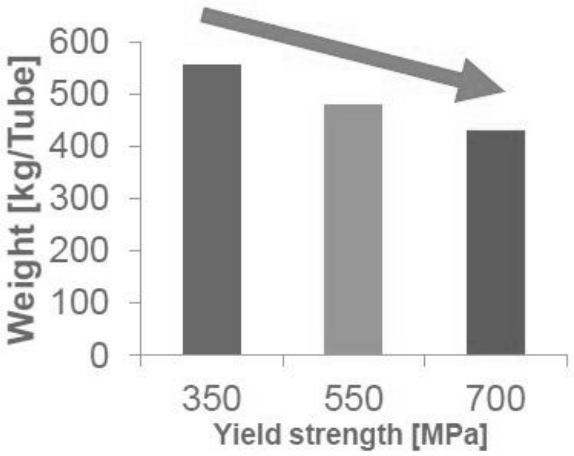

Figure 2: Decrease in mass for tubes used in the solar industry as a function of yield strength. [2]

1.2 Problem statement

It is well known that controlling the recovery window during the annealing process of both plain C and microalloyed strip steels is quite challenging [3]. In particular, plain low C steels have a narrower recovery process window. Small changes in time and temperature may result in variations of properties across the width and length of the material. However, the following factors can be optimised to extend the recovery window to longer times and higher temperatures:

- Amount of cold work prior to annealing;
- Chemistry, vis-à-vis microalloying with Nb and Ti or V or a combination of both to retard the restoration processes and;
- Hot rolling parameters, such as finishing and coiling temperatures maximise the precipitation of the carbonitrides in order to delay the restoration process.

Although recrystallisation is well understood, extensive studies into the metallurgical changes occurring during recovery in microalloyed steels are limited.

1.3 Objectives

The objectives of this study were as follows:

- To optimise the back-annealing processing conditions of the heavily cold-worked low C-Mn microalloyed V-N strip steels to achieve EN 10346 S700GD specification (0.2% yield strength $>$ 700 MPa, UTS: 750-910 MPa and $A_{80} > 10\%$);
- To understand the mechanisms influencing the kinetics of recovery and partial recrystallisation and;
- To compare low C-Mn-V-N steels' recovery window against plain low C and low C-Mn-Nb-Ti steels.

Chapter 2: Literature study

2.1 High strength low alloy steels

2.1.1 Strengthening mechanisms of vanadium, niobium and titanium in steels

HSLA (high strength low alloy) steels which are microalloyed with Nb, Ti and V result in dispersion strengthening and grain refinement. During hot rolling, the austenite grain size directly impacts the final ferrite grain size. Particles that remain undissolved during re-heating or precipitate during hot rolling limit grain growth of austenite and ferrite. For dispersion strengthening (restriction of dislocation movement), very fine particles ∼2-5 nm are required which can only be achieved with precipitation in ferrite i.e. during or after hot rolling [4].

The stability of the carbides and nitrides, particularly Ti, Nb and V at high temperatures results in dispersion strengthening. From Figure 3, it is seen that TiN can remain undissolved at re-heat temperatures >1200 °C making it the most stable carbonitride. V is significantly more soluble in austenite than Nb and Ti at a temperature as low as 1050 °C and this results in precipitation during later stages of hot rolling. Figure 3 gives a good indication of when microalloy carbides and nitrides are expected to precipitate. However, industrially, there are various other elements in steel that have an affinity for carbon and nitrogen which affects precipitation behaviour. To calculate solubility dependence on temperature, the Arrhenius relationship is used:

$$\log k_s = \log[M][X] = A - \frac{B}{T} \tag{1}$$

where k_s is the equilibrium constant, $[M]$ is the dissolved microalloy weight % and $[X]$ is the weight % carbon or nitrogen, A and B are constants, and T is the absolute temperature. Figure 3 is a compilation of various authors' results, which all contained a spread in the region of 150 °C.

All carbides and nitrides have a NaCl cubic structure [4] resulting in mutual solubility as shown by a ThermoCalc simulation on Nb-Ti-V steel in Figure 4, except for (V,Zr)N, because with V and Zr there is limited mutual solubility due to the large difference in atomic size. It should be noted that Al differs from microalloying elements due to the fact that it only forms a nitride with a hexagonal close-packed structure.

ThermoCalc precipitation simulations of carbonitrides on a 0.1% V steel are shown in Figure 5. An important aspect of V-microalloyed steel is the effect Mn has on increasing the activity coefficient of V while decreasing the activity coefficient of C. From Figure 5(b) the mole fraction N in V(C,N) shows that V precipitates in austenite as almost a pure nitride until practically all the N is consumed, followed by a gradual transition to mixed carbonitrides. As mentioned earlier, V is significantly more soluble in austenite than other microalloying elements, and this suggests that V carbide completely dissolves even at very low austenitising temperatures. Therefore, V carbonitrides will precipitate during, or even after austenite-ferrite transformation. The sudden increase in precipitation occurs due to the solubility drop

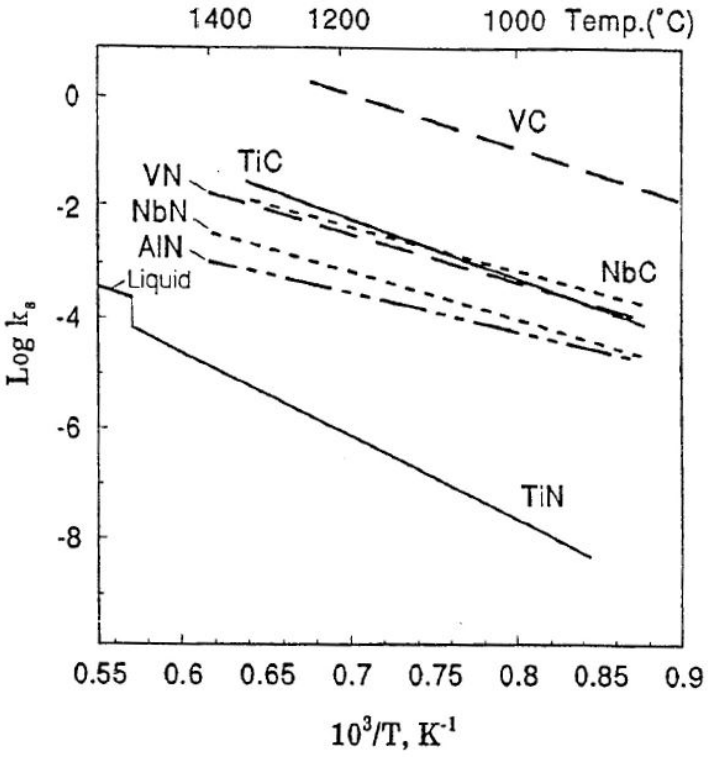

Figure 3: Simplified solubilities of microalloy carbides and nitrides. [5]

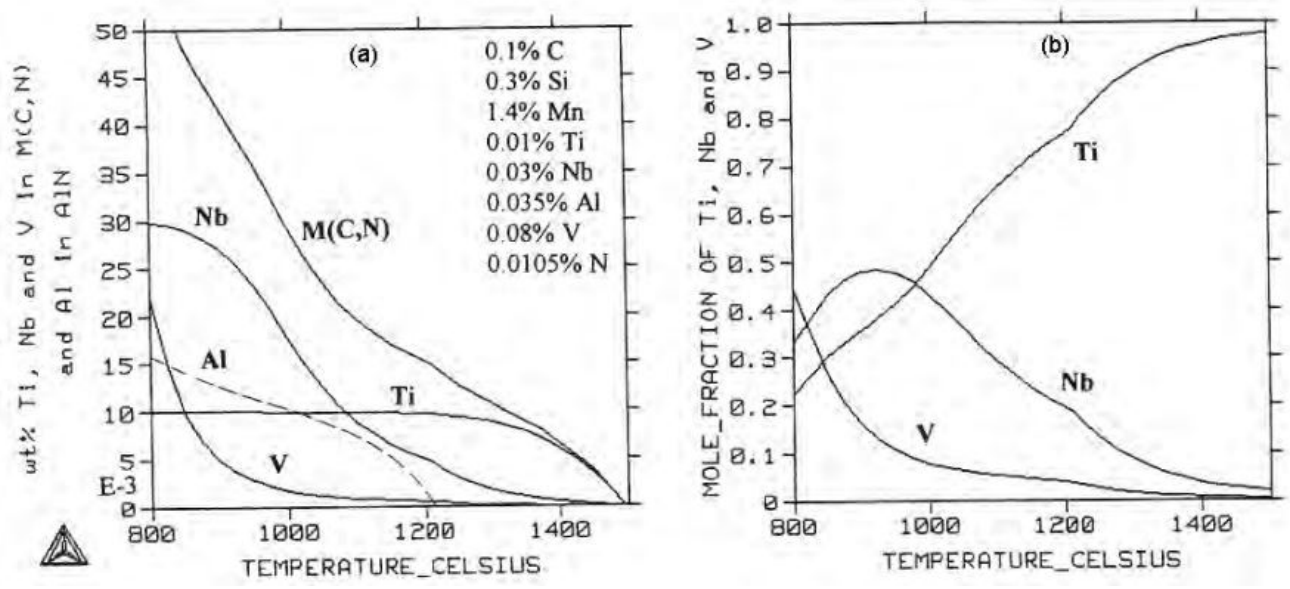

Figure 4: ThermoCalc simulation of carbonitride M(C,N) composition on multi-alloyed steel where M is Nb, Ti and V, (a) weight % and (b) mole fraction. [4]

of V carbonitrides in ferrite during the austenite-ferrite phase transformation. On the contrary, the Ti and Nb precipitation is limited during and after rolling due to stable carbonitrides precipitating at higher temperatures, Figure 4. This results in superior austenite grain refinement with Nb and Ti compared to V. However, the mill forces during the hot rolling process of the Nb and Ti steels are generally higher than for V steels [6].

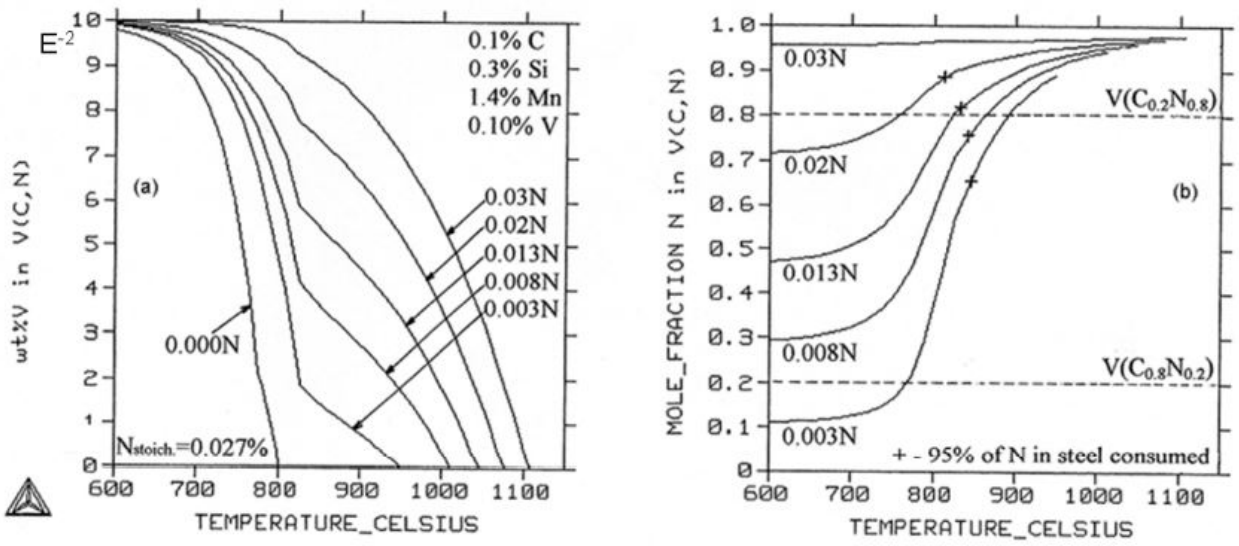

Figure 5: ThermoCalc simulation of carbonitride precipitation in a 0.10 % V steel for various nitrogen contents, (a) weight % V in V(C,N) and (b) mole fraction N in V(C,N). [4]

2.1.2 Hot rolling of strip steels

During the re-heating process before hot rolling, carbonitride phases rich in V typically dissolve. It's worth noting that V exhibits the highest solubility in austenite among all microalloying elements. In the subsequent hot rolling process, almost all of the V content is preserved for precipitation within ferrite, which results in effective grain refinement [4].

After hot rolling the strip is cooled to the desired temperature, and is tightly coiled, leading to a gradual cooling process. The choice of coiling temperature is important as it governs the size and distribution of precipitated particles [4][6]. Figure 6 illustrates the impact of coiling temperature on the hot-rolled yield strength of 0.12% V steel with varying nitrogen content. Higher coiling temperatures result in decreased strength due to larger precipitates and coarser ferrite. Conversely, low coiling temperatures restrict precipitation, retaining more V in solid solution due to slow diffusion at these temperatures. Consequently, the optimal yield strength is achieved at intermediate temperatures. For this specific alloy, the optimal coiling temperature was found to be 580 °C for all nitrogen contents [4].

The impact of transformation temperature and N levels on the precipitation strengthening of V-microalloyed steels is depicted in Figure 7, showing both isothermal (a) and continuous (b) transformation. Within this range of nitrogen content, a linear increase in strength is observed, as illustrated in Figure 7.

Examining Figure 7(b), it becomes evident that controlled rolling at low temperatures results in less strength gain compared to high-temperature rolling. This disparity is attributed to the strain-induced precipitation of V-nitrides in the austenite phase [5]. In the normalised condition, the strength significantly decreases due to the growing presence of large undissolved V-nitrides, which hinder the strengthening effect. This observation emphasises the critical role of both transformation temperature and nitrogen levels in shaping the mechanical properties of V-microalloyed steels.

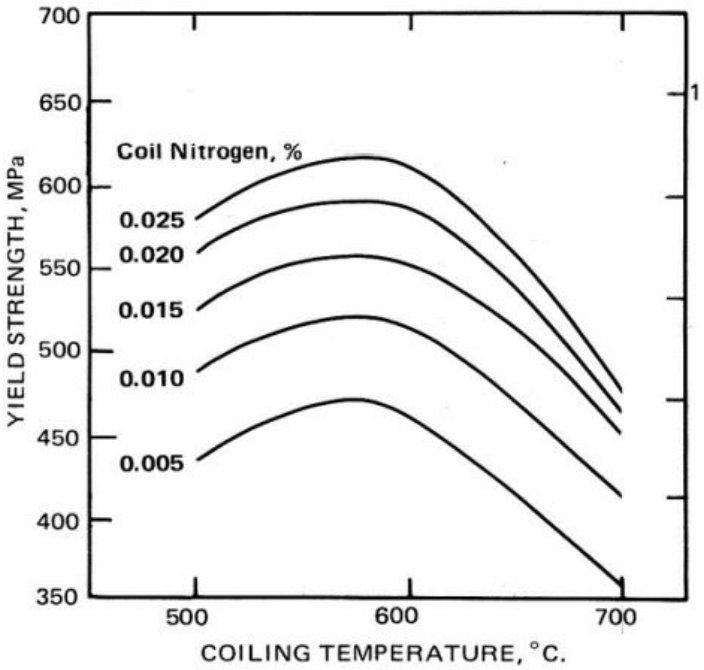

Figure 6: Coiling temperature vs. yield strength on 0.12% V steel with various N-level. [4]

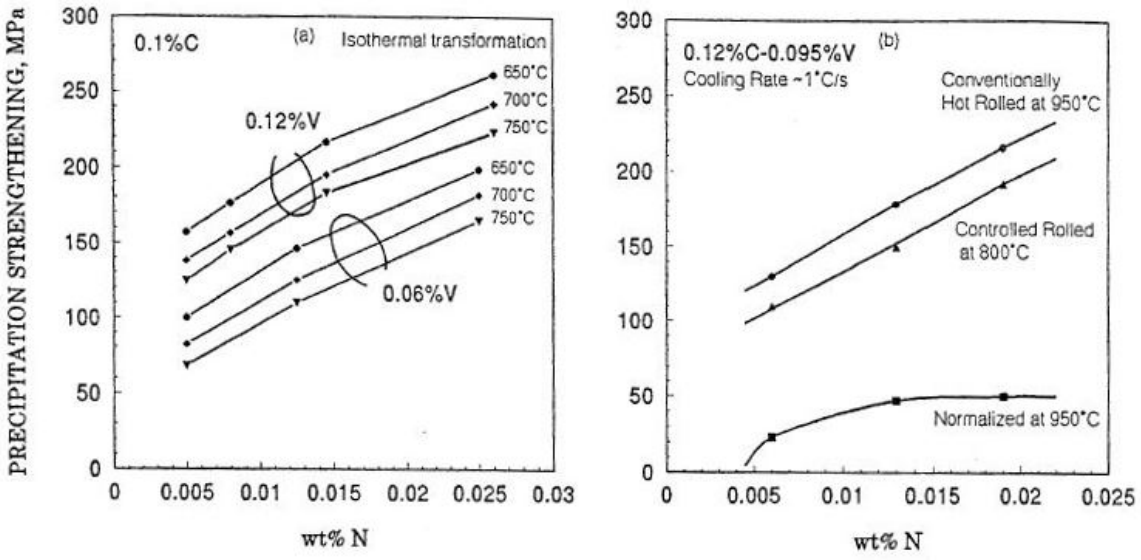

Figure 7: Effect of V, N and transformation temperature on precipitation strengthening of 0.1C% V-N steel after isothermal (a) and continuous (b) transformation. [5]

Incomplete precipitation during hot rolling leads to the presence of residual solutes, which subsequently precipitate during subsequent heating processes. A distinct secondary hardening peak becomes apparent in quenched materials within the temperature range of 550-650 °C [7]. This phenomenon is clearly illustrated in a Fe-1V-0.2C wt% quenched and tempered steel shown in Figure 8. Figure 8(a) showcases the formation of VC precipitates on dislocations at a temperature of 550 °C. The presence of these precipitates at this temperature indicates the onset of the secondary hardening process. Subsequently, in Figure 8(b), coarsening of these precipitates is observed at 700 °C.

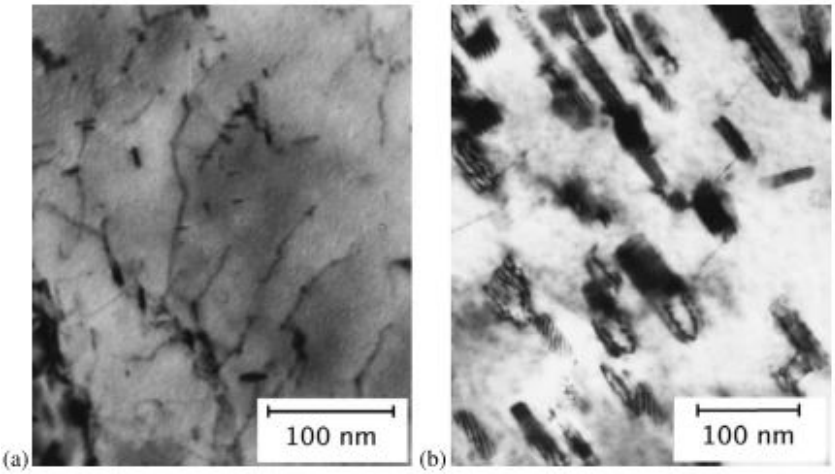

Figure 8: TEM micrograph of VC precipitates in a Fe-1V-0.2C quenched and tempered steel: (a) 550 °C 72 h, (b) 700 °C 50 h. [7]

2.2 Recovery and recrystallisation fundamentals

2.2.1 Energy of deformation

During the cold working of metal, the majority of energy is dissipated as heat, with a small fraction being stored within the structure as strain energy due to lattice defects. Dislocations are the primary source of this stored energy, except in cases of very low deformations, where other point defects like vacancies and interstitial atoms are significant. With higher amounts of deformation, the resulting higher dislocation density consumes these point defects. Additionally, the grain boundary area expands considerably with higher levels of deformation, resulting in a substantial increase in stored energy. Evidently, starting with a smaller initial grain size amplifies the stored energy within the structure [8].

The quantity of stored energy is dependent on the composition, initial structure, and the temperature at which cold work is carried out. Typically, the maximum stored energy falls within the range of 1-10% [9]. As the level of cold work intensifies, there is a corresponding increase in stored energy, although the rate of this increase diminishes.

The free energy of a deformed metal is greater than an annealed metal. From the general free energy equation:

$$\Delta G = \Delta H - T\Delta S \tag{2}$$

where ΔG signifies the change in free energy due to cold work, ΔH represents the stored strain energy or enthalpy, S denotes the entropy increase attributed to cold work, and T is the absolute temperature.

In practical scenarios, plastic deformation induces a rise in entropy, albeit small when compared to the increase in internal energy (strain energy). Consequently, the term $-T\Delta S$ in Equation (2) is often negligible. This simplification leads to Equation (3), where the increase in free energy is approximated as the stored energy [8]:

$$\Delta G \approx \Delta H \tag{3}$$

As a result of cold work's inherent complexity, numerous reactions take place within the structure. Many of these reactions involve atom and vacancy movements that are sensitive to temperature variations. Consequently, heating significantly accelerates the rate of softening processes [9].

It should be noted that knowledge of dislocation accumulation rates during deformation remains incomplete. This contributes to the complexity of quantitatively modelling recrystallisation and recovery processes [8][9].

The annealing behaviour of a material is heavily influenced by the stored energy and the spatial distribution of defects, particularly the homogeneity of stored energy at a local scale. This local distribution significantly impacts the nucleation of recrystallisation and the subsequent growth of new grains. Predicting annealing behaviour necessitates an understanding of defect distribution resulting from the deformation process.

An oversimplified approach to relating microstructure and stored energy assumes that a polycrystalline material comprises high-angle grain boundaries and two distinct components [10]:

- **Cells/subgrains:** These are typically equiaxed micron-sized volumes enclosed by geometrically necessary dislocations (GNB), known as dislocation walls. These walls consist of either tangled low-angle boundaries (cells) or well-ordered low-angle boundaries (subgrains), as illustrated in Figure 9(a) and (b).
- **Statistically stored dislocations (SSD):** These dislocations are distinct from those forming the walls mentioned above and are often referred to as incidental dislocation boundaries (IDB).

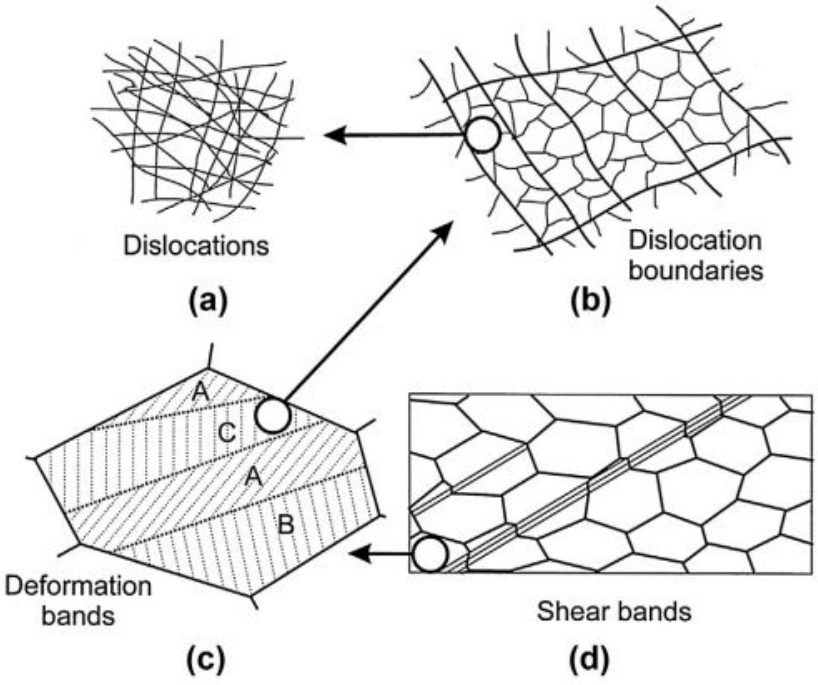

Figure 9: Schematic of polycrystal metal deforming by slip. (a) dislocations, (b) dislocation boundaries, (c) deformation bands, (d) grain scale shear bands. [8]

Advanced techniques such as electron microscopy enable the observation of subgrains and dislocations. Additionally, X-ray diffraction (XRD) methods can be employed to estimate subgrain/cell size and dislocation density, a topic elaborated in Section 2.4.7.

Referring again to Figure 9, it is essential to classify the hierarchy of a deformed metal based on its heterogeneity. Specifically focusing on moderate to high deformation scenarios in plane strain compression (e.g., rolling) and metals with moderate stacking fault energy (e.g., α-iron [8]):

- **Dislocations:** These exist as intricate tangles or random structures and are not confined within cell walls, Figure 9(a).
- **Cells/Subgrains:** These represent the smallest identifiable volume elements, Figure 9(b).
- **Deformation Bands:** On a larger scale, individual grains subdivide during deformation into regions of varying orientations. This subdivision arises from the inhomogeneous stresses of neighbouring grains during deformation and the intrinsic instability of grains under such conditions, Figure 9(c).
- **Shear Bands:** Intense shear deformation occurs on a polycrystalline metal inclined to the rolling plane. This phenomenon arises due to plastic instability and is equivalent to necking observed during tensile tests. Shear bands can traverse multiple grains and even extend across the entire specimen, as illustrated in Figure 9(d). Figure 10 provides an example of shear bands in 85% cold-worked iron.

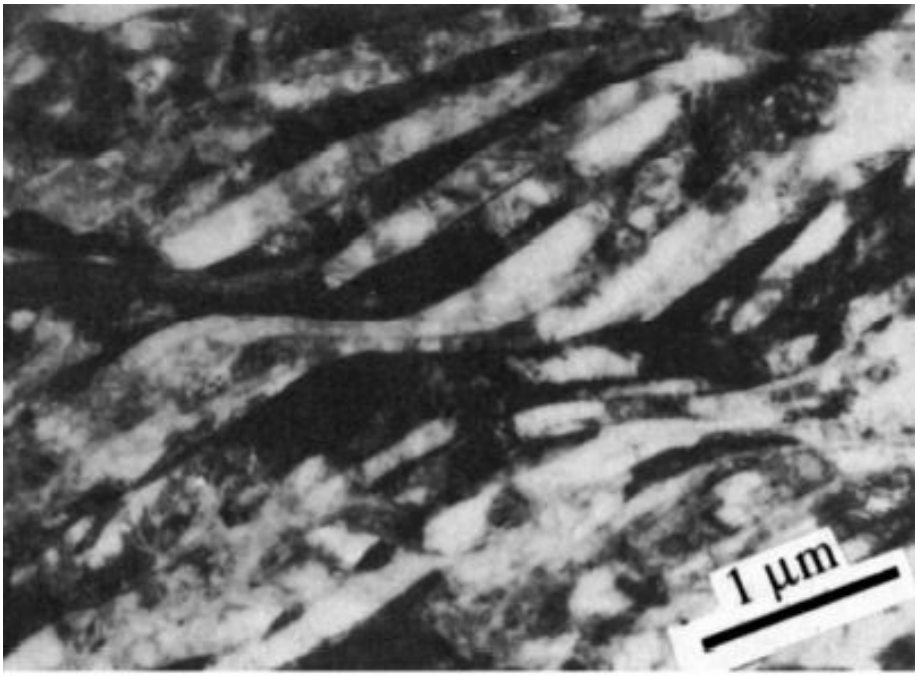

Figure 10: 85% cold work iron with visible shear bands. [8]

2.2.2 Deformation of two-phase alloys

Many metals contain dispersed second-phase particles that affect the deformation and the subsequent annealing behaviour. Aspects to consider of the second phase particles include [8]:

- Effect on dislocation density;
- Effect on the homogeneity of deformation, which affects the availability of sites and energy required for recrystallisation and;
- Deformation structure surrounding the particles and whether it can accelerate recrystallisation by particle-stimulated nucleation (PSN) or not.

During deformation, dislocation lines will bow around particles as seen in Figure 11. If the particle is strong enough, the dislocation will encircle the particle creating an Orowan loop. This results in extra dislocations generated in the form of Orowan loops. If the particle deforms, the dislocation will pass through by shearing the particle as illustrated in Figure 12. There are various factors that could affect whether a particle will deform *inter alia*: size, coherency and strength.

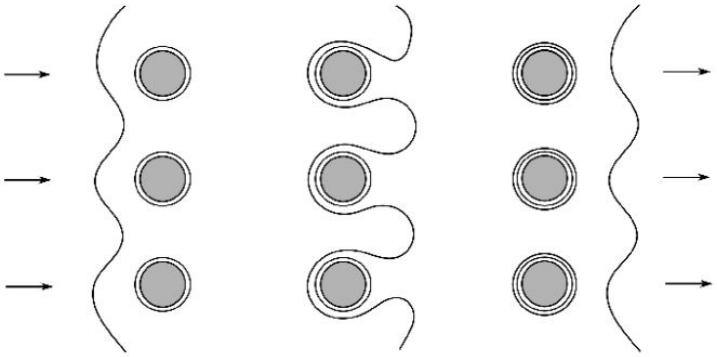

Figure 11: Schematic diagram showing the formation of Orowan loops around an incoherent particle. [11]

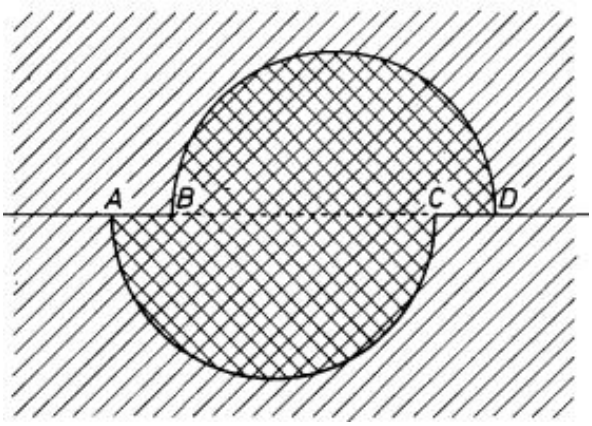

Figure 12: Schematic diagram showing particle shearing after dislocation has passed through it, the distance AB and CD equals the burger vector. [12]

2.2.3 Recovery process

Recovery is the changes in dislocation structure prior to recrystallisation, partially altering the properties to the softened state. Recovery can also be seen as the process before new strain-free recrystallised grains appear and involve no migration of high-angle grain boundaries (HAGB). Recovery consists of several stages which are shown schematically in Figure 13.

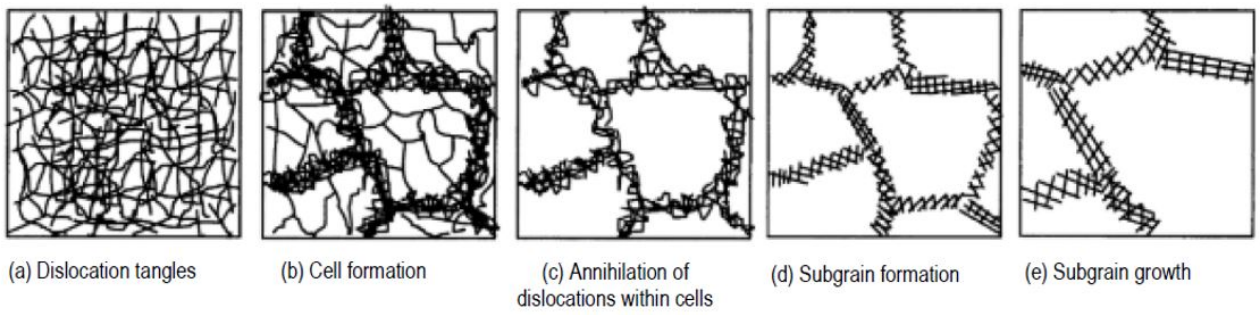

Figure 13: Schematic diagram showing the stages occurring during recovery. [8]

Recovery is influenced by various factors, including material type, purity, deformation amount, and deformation and annealing temperatures [8]. Generally, these stages occur in the order depicted in Figure 13, although there is often some overlap. Recovery and recrystallisation processes are closely related, both being driven by stored energy (Equation 2). It is possible that partial or no recovery precedes the recrystallisation process. However, once recrystallisation initiates, no more energy remains for recovery, as the deformed structure has been consumed. Hence, it is evident that recovery significantly influences recrystallisation kinetics.

The type of material significantly influences recovery kinetics, primarily due to the stacking fault energy. Recovery mostly involves dislocation movement and the extent to which dislocations can climb and cross-slip, controlling the rate of the recovery process. In materials with low stacking fault energies, little or no recovery will take place before recrystallisation. In materials like aluminium and α-iron, which have moderate to high stacking fault energies, substantial recovery can take place before recrystallisation.

The effect of solute atoms on recovery is challenging to quantify; these atoms alter the stacking fault energy and increase stored energy due to deformation. The interplay of retarding effects (dislocation pinning) and acceleration effects (increased stored energy) caused by solute atoms makes predicting recovery kinetics challenging [9].

During recovery, the changes in the microstructure are small and not easily observed by optical microscopy or simple methods such as hardness testing. Various other methods to measure recovery are discussed in Section 2.4.

2.2.4 Dislocations during recovery

During recovery, the energy from deformation is primarily lowered through dislocation annihilation and re-arrangement. In a simplified explanation, dislocations on the same plane with opposite signs annihilate through glide. Dislocations on different planes can also annihilate, but this process requires additional energy for climbing (dipole annihilation). Annihilation by glide can occur at very low temperatures and even during deformation (dynamic recovery), while climbing requires thermal activation and occurs at higher temperatures [10].

The kinetics of dislocation annihilation, whether edge, screw, or mixed, are complex, especially in polycrystals and materials with complex compositions. Several equations describe uniform dislocation recovery and can fit experimental observations. However, the main difficulties encountered include [10]:

- The complex relationship between mechanical properties and microstructure;
- Concurrent occurrence of dislocation re-arrangement and annihilation;
- The need for a more accurate definition of the effects of solutes and stacking fault energy on dislocation mobility;
- Non-homogeneous occurrence of recovery processes.

2.2.5 Polygonization

A recovery model known as polygonization represents a simple form of a plastically bent crystal. Figure 14 illustrates polygonization. Before recovery, there exists an excess of positive edge dislocations in active slip planes, carrying high strain energy. These dislocations re-arrange to achieve a lower energy state through the annihilation of opposite sign dislocations. The excess positive dislocations then align normally to the slip planes. This configuration of dislocations is termed low-angle grain boundaries (LAGB) [8].

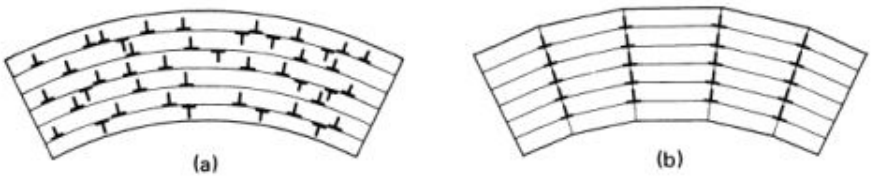

Figure 14: Schematic diagram of a bent crystal showing dislocation movement (a) after deformation (b) after annihilation and re-arrangement into lowest energy configuration. [9]

The edge dislocations that accumulate on the same slip plane within the strain fields are additive. However, the consideration of regions above and below the dislocation strain partly cancels out, as depicted in Figure 15. This process leads to a reduction in strain energy and the elimination of lattice curvature, rendering the crystals nearly strain-free [9].

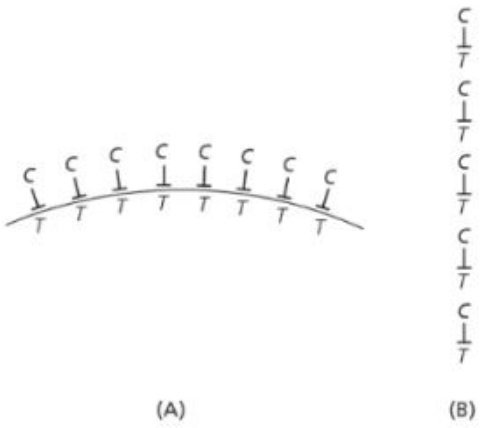

Figure 15: Schematic diagram showing tension (T) and compression (C) of dislocations after polygonization. [9]

In polycrystalline materials subjected to significant deformation, the dislocation structure becomes intricate, involving various Burgers vectors. Two-dimensional networks are formed, the specifics of which depend on the type of dislocations involved. In materials with high stacking fault energies, a three-dimensional cell structure typically develops, where the walls of the cells consist of complex dislocation tangles [8].

Figure 16 depicts a TEM image of 40% cold-worked ultra-low carbon Ti steel annealed at 700 °C for 2 minutes, displaying various recovery stages. Cells a and b exhibit significant dislocation tangles at the edges, while cells d and c have formed into defined sub-grains, with diminished dislocations within. In Figure 16(b), signs of sub-grain combining are visible, indicating the subsequent stage of recovery: sub-grain growth. Similar behaviour can be observed in low C-Mn steel, as shown in Figure 17.

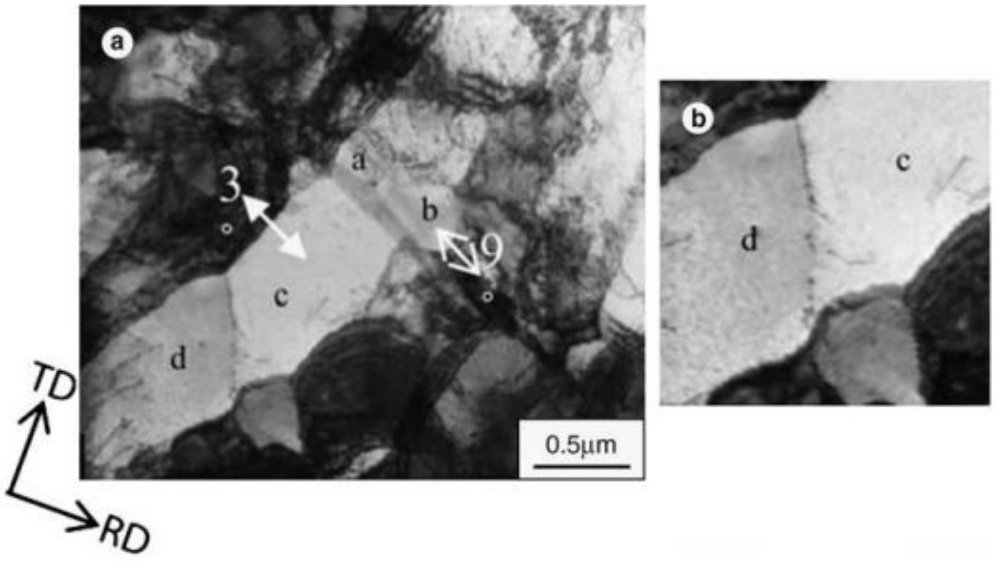

Figure 16: TEM image of 40% cold rolled ultra-low carbon Ti steel annealed at 700 °C for 2 minutes. [13]

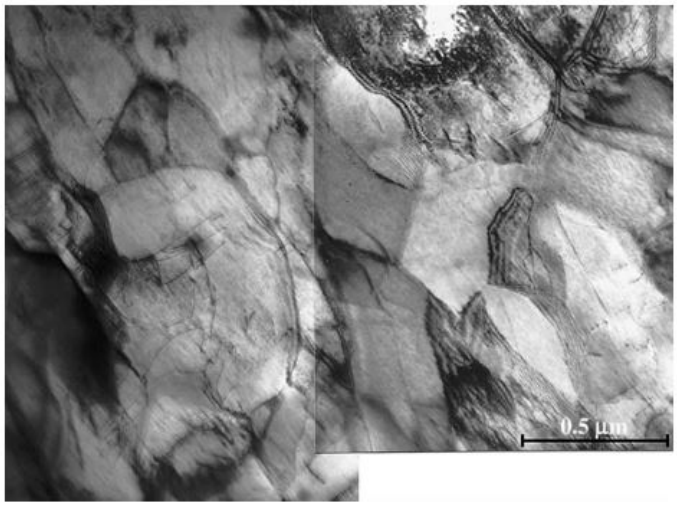

Figure 17: TEM image of 83% cold rolled 0.03% C, 0.19% Mn steel isothermally annealed at 500 °C for 4.8 h. [14]

The transition from dislocation tangles in cell walls to sub-grains can be defined as a distinct stage of recovery. This stage involves the annihilation of redundant dislocations, with the remaining dislocations arranged into low-angle boundaries, as mentioned above. During this process, the yield strength decreases, and the work hardening rate increases.

In certain materials, dynamic recovery occurs to such an extent that the dislocation structure is well-defined, i.e., subgrains form before annealing. Consequently, recovery in these cases only involves sub-grain growth. Factors contributing to this well-defined subgrain structure are [8]:

- High stacking fault energy.
- Low solute content.
- Large strains.
- High temperature of deformation.

2.2.6 Factors affecting recrystallisation rate

Recrystallisation is generally considered very complex, especially in industrial steels which consist of various alloy elements and high deformations [8]. However, there are fundamental concepts known to affect the rate and onset of recrystallisation, including some of the following [9][15][16]:

- **Prior strain:** Higher amounts of deformation lead to an increase in stored energy (Equation 2) and effective nuclei, accelerating recrystallisation.
- **Texture:** The initial and deformed texture influence the driving force and nucleation sites for recrystallisation due to different orientations resulting in changes in active slip systems. This effect is illustrated schematically in Figure 18 for cold-worked iron.

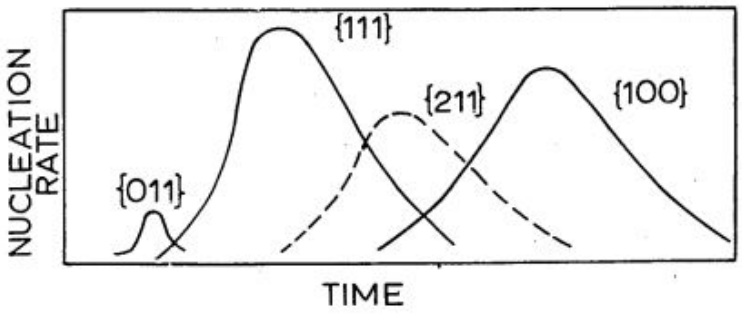

Figure 18: Schematic diagram showing the orientation dependence of the recrystallisation rate of cold-worked iron. [16]

- **Prior grain size:** Smaller grain size increases stored energy and, consequently, accelerates the recrystallisation rate. Inhomogeneities such as shear bands increase with smaller grain sizes, acting as nucleation sites.
- **Annealing temperature and heating rate:** Higher temperature and heating rate accelerate recrystallisation. Lower temperatures and slow heating rates provide more time for recovery, therefore, retard the recrystallisation process.

These factors are not limited to single-phase alloys but, in principle, are also applicable to two-phase alloys, albeit involving additional aspects.

2.2.7 Second phase particles effect on recovery and recrystallisation

The presence of precipitates can either accelerate or retard recovery and recrystallisation because [8][15]:

- **Homogeneity of stored energy:** Precipitates affect the homogeneity of stored energy from deformation, as explained in Section 2.2.2;
- **Dislocation pinning:** Particles present before annealing inhibit dislocation movement by pinning them. This inhibition delays dislocation re-arrangement into a lower energy state by forming low-angle boundaries, effectively retarding recovery. Strong evidence supports the idea that a fine dispersion of second-phase particles pins subgrain boundaries and prevents growth. This theory is based on conventional grain growth during recrystallisation;
- **Particle-stimulated nucleation (PSN):** Large precipitates (diameter greater than $\sim$1 μm) already present in the matrix can coarsen further during annealing and act as nucleation sites for recrystallisation through the mechanism known as particle-stimulated nucleation (PSN);
- **Sequential or simultaneous recrystallisation with fresh precipitates:** Recrystallisation can occur sequentially or simultaneously with the nucleation of fresh precipitates due to supersaturation and/or transformation of metastable precipitates, resulting in a complex situation.

Figure 19 shows a simplified schematic diagram indicating whether recrystallisation will be accelerated

or retarded by second-phase particle dispersion. The position of line AB depends on the ease of dynamic recovery, i.e., more dynamic recovery moves the line to the right, while less recovery moves it to the left.

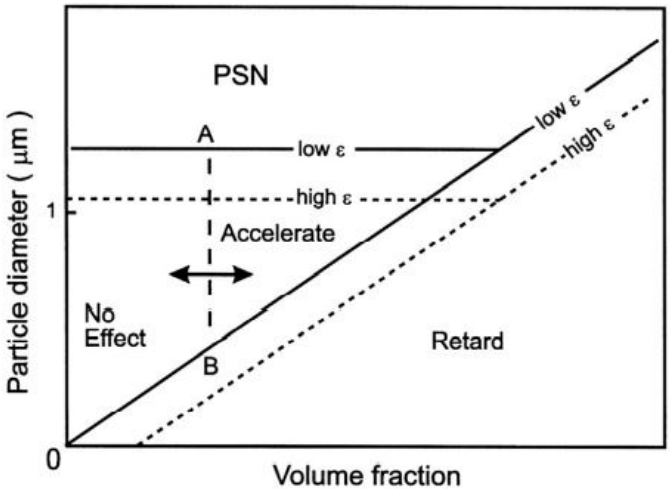

Figure 19: Schematic diagram illustrating the effect of particle size, volume fraction and prior strain effect on recrystallisation kinetics. [17]

Zener defined the retarding force of precipitates on recrystallisation due to boundary pinning as follows [8]:

$$P_{SZ} = \frac{3\gamma}{2}\left(\frac{V_v}{r}\right) \tag{4}$$

where γ is the surface energy per unit area of the grain boundary, V_v is the volume fraction of the second phase, and r is the particle radius. This equation assumes that all particles are on grain boundaries and have the same size. It is well known that closely spaced second-phase particles delay recrystallisation due to Zener drag [18].

The effects of solute atoms and concurrent or subsequent precipitation on boundary movement are complex. Many authors have observed initial retardation with high concentrations of solutes, followed by acceleration during subsequent precipitation of particles and coarsening [15][19][20]. At higher temperatures, recrystallisation precedes precipitation, therefore having no effect on the onset of recrystallisation. However, at low temperatures, precipitation can occur before recrystallisation, resulting in a retarding effect. This is illustrated schematically in Figure 20 whereby for:

- $T > T_1$: Recrystallisation is only affected by segregation; no precipitation occurs.
- $T_1 > T > T_2$: Recrystallisation is only affected by segregation; precipitation occurs after recrystallisation.
- $T < T_2$: Precipitation affects the re-arrangement of dislocations and movement of the recrystallisation front.

Whether recrystallisation will be retarded or accelerated depends on various factors, but it always in-

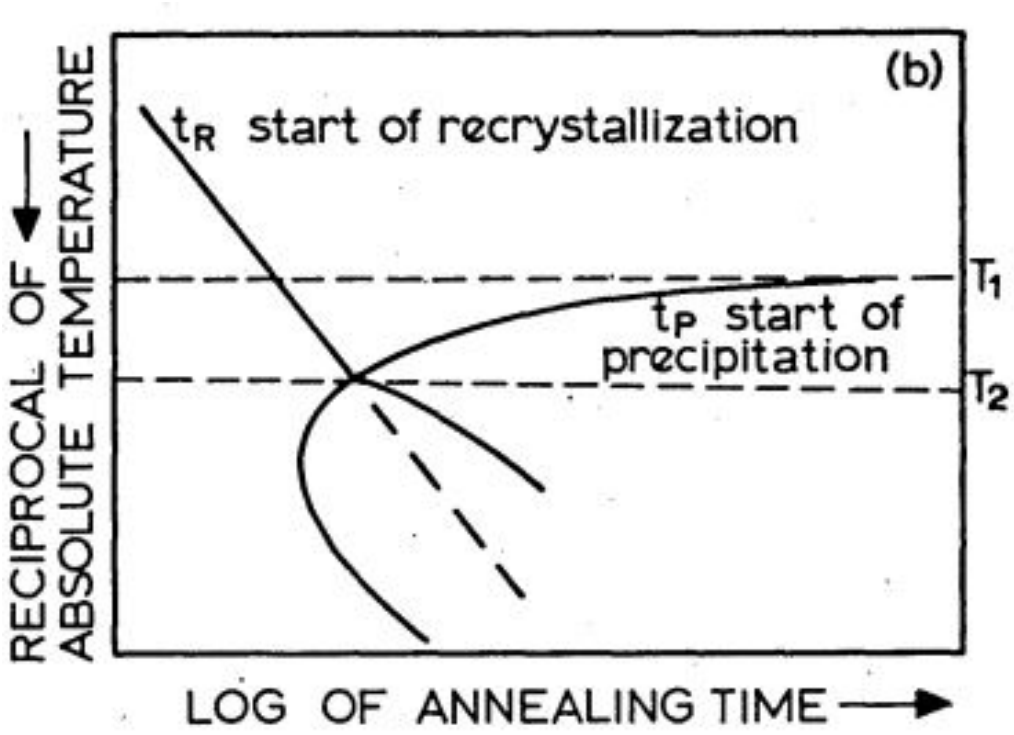

Figure 20: Schematic diagram of time and temperature effect on precipitation start t_P and recrystallisation start t_R. [20]

volves a balance between driving and retarding forces for recrystallisation. The dislocation density serves as the stored energy, E_D, which acts as the driving force P_d for recrystallisation and can be approximated as follows:

$$P_d = E_D = \alpha \rho G b^2 \tag{5}$$

where, α is a constant typically around 0.5, ρ represents the dislocation density, G is the shear modulus, and b is the Burgers vector of the dislocation. When particles are precipitating from a supersaturated solution or metastable precipitates are transforming into stable ones, there is an additional driving force P_c. For an ideal solution and small concentrations, the driving force can be approximated as follows [8]:

$$P_c = \Delta G_s = RT \ln K_s \tag{6}$$

where, R is the gas constant, T is the absolute temperature, and K_s is the solubility product. The condition for discontinuous recrystallisation, i.e., movement of the recrystallisation front, is given by [8]:

$$P_d + P_c > P_{SZ} \tag{7}$$

where P_{SZ} is derived from Equation 4. However, the prerequisite for the occurrence of discontinuous recrystallisation is the presence of a grain boundary capable of migration. This boundary can be formed by dislocation re-arrangement (recovery). Precipitates that form reduce segregation at dislocations, thus facilitating dislocation re-arrangement. Studies have shown that dislocation re-arrangement is

controlled by the growth of large particles and the dissolution of small particles, which pin dislocations and dislocation groups, i.e., dislocation-free regions correspond to particle distances [20]. Classical grain growth principles apply to subgrains, as illustrated in Figure 21.

As evident, immobile grain boundaries cannot produce a recrystallisation front. Additionally, dislocation re-arrangement is influenced by the growth of particles; as particles coarsen, the subgrain size and orientation difference increase, indicated by the thickness of lines. Furthermore, when smaller particles dissolve, the subgrains coalesce, as shown in Figure 21(c) through Y-node motion (A) or rotation (B). Defect-free areas and the angles between them increase with time. Although the conditions for discontinuous recrystallisation have not been met, this process is termed continuous recrystallisation.

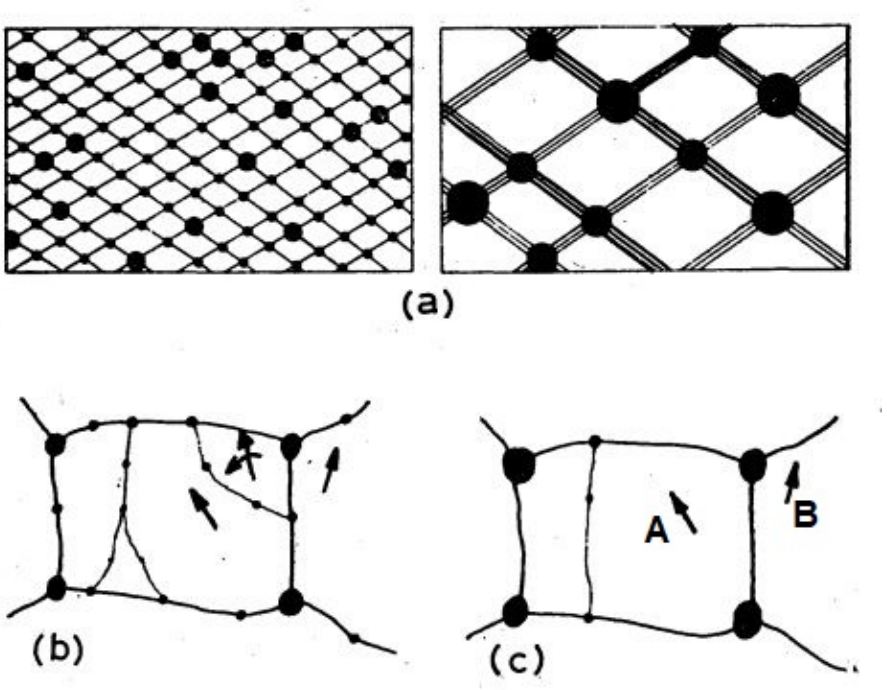

Figure 21: Schematic diagram showing continuous recrystallisation with precipitates. [20]

2.3 Nucleation of recrystallisation

2.3.1 Classical nucleation

Much work has been dedicated to understanding the mechanism of how recrystallisation initiates. It's essential to note that when referring to "nucleation" and recrystallisation, there is no direct nucleation of entirely new grains.

Burke and Turnbull suggested that the classical nucleation theory for phase transformations could be applied to recrystallisation [21]. According to this theory, recrystallisation occurs when random atomic fluctuations result in the formation of a small crystallite with a high-angle grain boundary. This can only happen when the energy difference between the deformed state and the recrystallised state is larger than the interface energy produced by the formation of the nucleus. While this theory can account for some

aspects of recrystallisation, such as an incubation period and preferred nucleation, it is often discounted due to the low driving force energy for recrystallisation compared to phase transformations, and the interfacial energy of a high-angle boundary is relatively large. Estimates indicated that the size of the critical radius would be so large that the rate of nucleation is negligible [8]. Therefore, it is concluded that recrystallisation originates from small volumes already present in the deformed microstructure and are not ”nuclei” in the traditional thermodynamic sense. Recrystallising grains must emerge as an outcome of recovery and polygonization of the deformed structure, as explained by Cahn [22].

2.3.2 Abnormal subgrain growth (AsGG)

A mechanism similar to normal grain growth is abnormal subgrain growth (AsGG), which serves as a nucleus for recrystallisation. As discussed in Section 2.2.3, plastic deformation results in nonuniformly stored dislocations (Figure 13(a)), followed by cell formation (Figure 13(b)). When this cell structure recovers, it typically leads to a subgrain structure where the boundaries are atomically sharp, similar to normal grain boundaries but with smaller lattice misorientations, a phenomenon known as polygonization (Figure 13(c)(d)). Coarsening of the subgrain structure, which leads to recrystallisation, can be observed as abnormal grain growth of the subgrain structure. Several models and theories were developed by authors to explain recrystallisation by AsGG [23][8]. Models combining AsGG with other nucleation mechanisms such as PSN and SIBM provided reasonable predictions of the final grain size after recrystallisation [24][25].

Work done by Hughes (1997) found that the average misorientation between cells and subgrains increases monotonically with strain [26]. In their study, aluminium with cold works ranging from 5 to 50% showed that the average misorientation was proportional to the square root of strain. Power law relationships were defined for two types of misorientations, i.e., GNB and IDB, as seen in Figure 22.

From subgrain network analysis, it is concluded that the probability of abnormal growth increases significantly with an increase in average misorientation [8]. Misorientation reflects the spread in orientation; therefore, the larger the average misorientation, the larger the orientation spread from which it is derived. Increasing grain orientation spread (GOS) results in a higher number of grains that deviate sufficiently far from their neighbours to have high mobility boundaries. If the grain is in a growth configuration, it will grow abnormally large due to its high mobility perimeter, which effectively acts as a nucleus for recrystallisation. Wang *et al.* showed that nucleus density together with subgrain size explains how the recrystallised grain size is strongly dependent on prior strain (which controls the amount of misorientation) [8].

2.3.3 Strain-induced boundary migration (SIBM)

Strain-induced boundary migration (SIBM) involves the bulging of a preexisting grain boundary. The region behind the migrating boundary has a lower dislocation density, as shown schematically in Figure 23. A distinctive feature of SIBM is that the new grains have similar orientations to the grains from

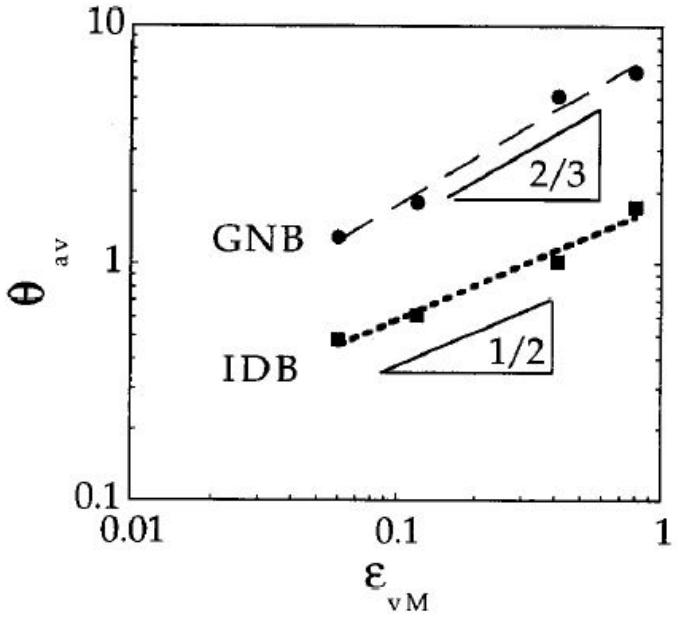

Figure 22: Power law relationships between the average misorientation angles and the applied strain for GNB and IDB on aluminium with cold works ranging from 5 to 50 %. [26]

which they originated [8]. SIBM is mainly observed in materials with very low reductions, with the first reported study indicating a mechanism change at reductions greater than 40% in pure aluminium [27]. The driving force for SIBM is suspected to arise from the dislocation density difference of neighbouring grains. This can be a direct result of the deformation process, as dislocation storage may be dependent on grain orientation [28].

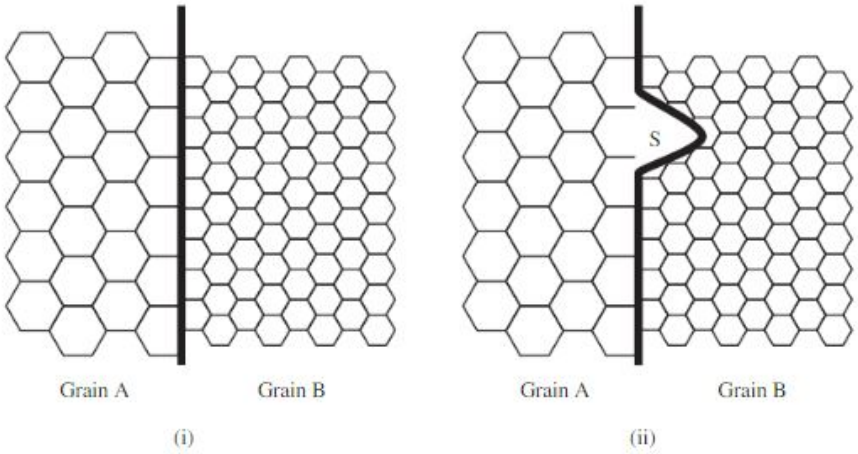

Figure 23: Schematic diagram of SIBM (i) Grain A has lower stored energy than Grain B, (ii) migrating boundary S dragging dislocation structure resulting in a new dislocation free grain. [29]

If a material has a well-recovered subgrain structure, SIBM may originate at a single large subgrain, as shown schematically in Figure 24. In contrast to multiple subgrain SIBM, there is no need for a stored energy difference between the grains; only a subgrain with a critical size adjacent to the grain boundary

is required [8]. However, a difference in stored energy decreases the critical size of the subgrain required for SIBM. Therefore, the viability of single subgrain SIBM is dependent on the size distribution, size, and boundary energies (misorientation) of subgrains in the two grains. Figure 25 shows the effect of subgrain sizes and misorientation in two grains on the critical subgrain size for SIBM.

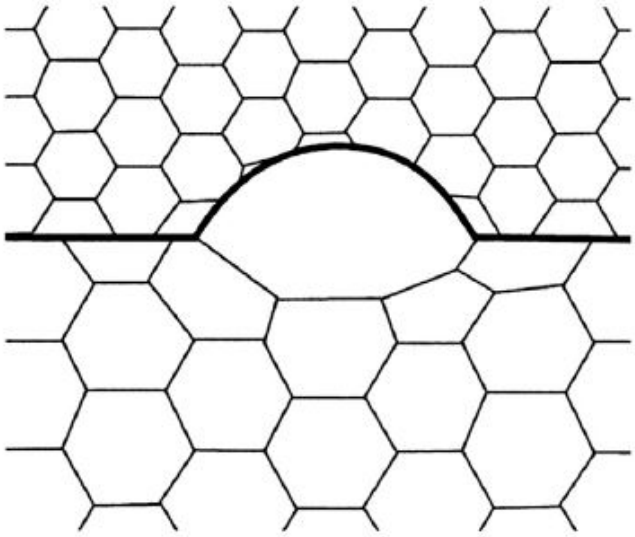

Figure 24: Schematic diagram of SIBM from one large subgrain. [29]

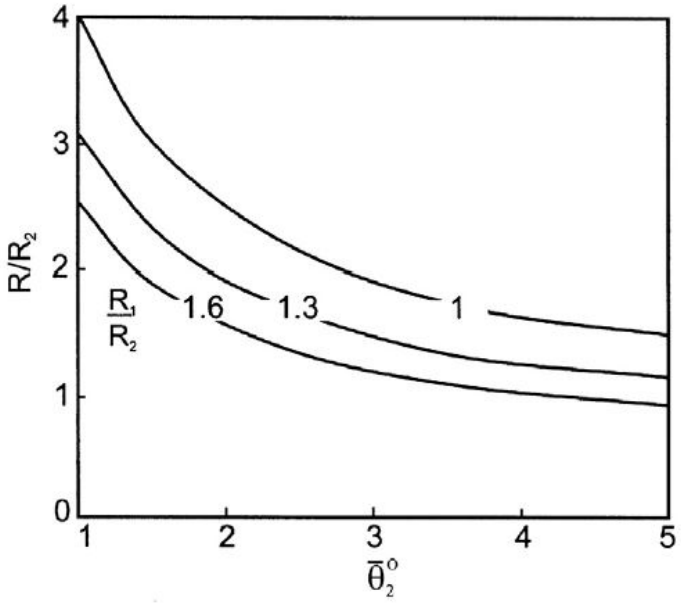

Figure 25: The critical size *R* for a large subgrain in grain 1 R_1 to undergo SIBM as a function of mean subgrain misorientation $\bar{\theta}_2°$ in grain 2 R_2 and relative sizes of subgrains in the two grains (R_1/R_2). [8]

Despite the importance of SIBM and recrystallisation, there is still much work required to clarify the mechanism and conditions under which SIBM occurs.

2.3.4 Preformed nucleus model

As discussed above, the high-angle boundary required for recrystallisation already exists; however, in many cases, recrystallisation occurs in regions where there is no such boundary. It is established that recrystallisation occurs from dislocation cells or subgrains present in the deformed microstructure. Although there is still uncertainty, the following aspects are known [8]:

1. The orientation of the nucleus is present in the deformed structure. No new orientations are formed during or after nucleation, except in the case of twinning;
2. Nucleation occurs through normal or abnormal subgrain growth. There is no evidence that subgrain coalescence plays a significant role, but only low-angle boundary migration;
3. An orientation gradient must be present to produce a high-angle boundary by rapid recovery. It should be noted that higher stored energy is always associated with a region with a large orientation gradient because accommodating the misorientation geometrically necessitates dislocations or low-angle boundaries.

2.4 Quantification of the recovery process

2.4.1 Recovery kinetics

A single parameter is the simplest means of measuring recovery kinetics, such as hardness, yield strength, heat evolution, or resistivity. From the annealed condition X_R, the rate of recovery dX_R/dt may be defined experimentally. However, the relationship of X_R to microstructure and different stages of recovery that can occur simultaneously makes it difficult to gain fundamental insight. Empirical relationships have been defined for X_R and t, but only include time under isothermal conditions. To determine the optimal temperature and time required for desired properties, a parameter R can be defined as follows for any property:

$$R = \frac{X_m - X}{X_m - X_0} \tag{8}$$

where X_m is the property in the cold work condition, X_0 is the property in the fully annealed condition, and X is the property after recovery annealing [3].

2.4.2 Calorimetry

Measuring the release of stored energy during heating provides valuable information on the reactions that occur. The development of highly sensitive differential scanning calorimetry has enabled the study of annealing phenomena in metals. It involves heating a fully annealed sample as a reference and comparing it to a deformed sample. The power required to heat the deformed sample will be less than that for the annealed sample. The released stored energy increases the heat flow [9].

The information obtained using calorimetry is not always simple to analyse, as seen in studies conducted on pure aluminium. Figure 26 shows two clear points of high energy release: the first peak is

from recovery, and the second is due to recrystallisation. In Figure 27, the peaks are not as defined, and a gradual release of energy is observed, indicating the concurrent occurrence of recovery and re-crystallisation [10].

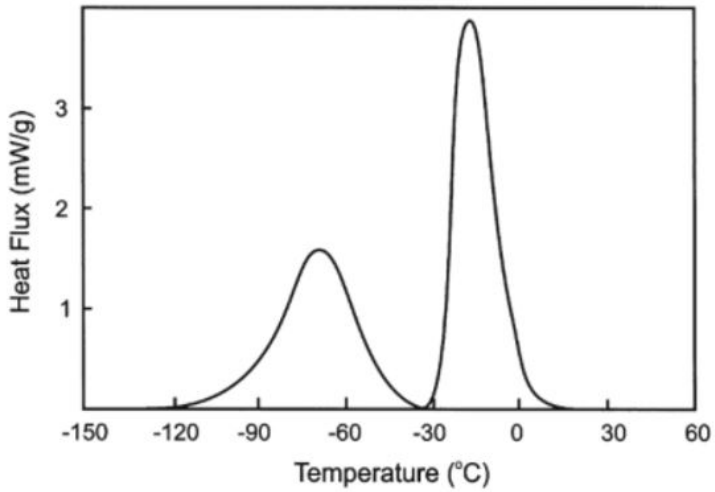

Figure 26: Heat flux vs. temperature of 99.999% Al deformed to a true strain of 6.91 at 77 K using differential scanning calorimetry. [9]

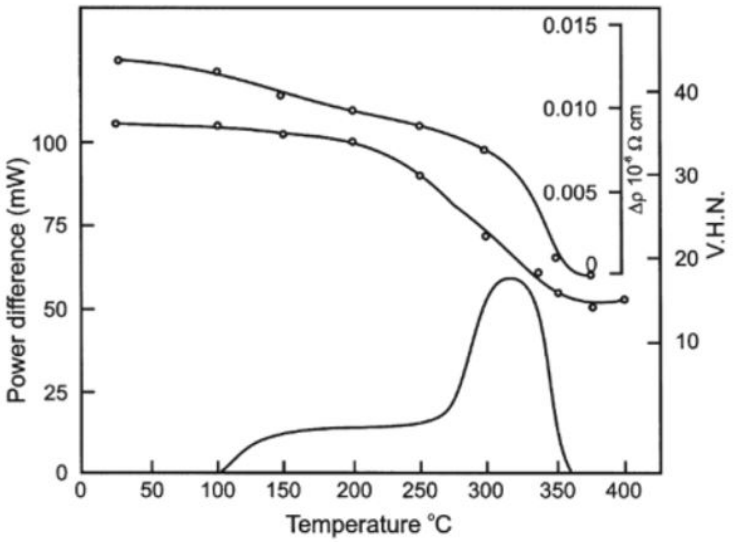

Figure 27: Power difference, electrical resistivity and hardness changes during heating of 75% compression deformed 99.998% Al at 6 °C/min. [10]

2.4.3 The Johnson-Mehl-Avrami-Kolmogorov (JMAK) Model

The well-known JMAK (Johnson-Mehl-Avrami-Kolmogorov) model [30][3] is an important tool in the analysis of restoration kinetics. The shape of the curve seen in Figure 28 is the typical shape for many transformation reactions. It phenomenologically describes the constituent's nucleation and growth processes [8].

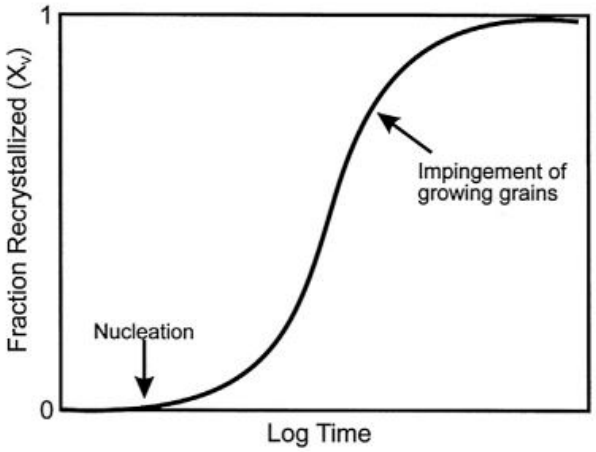

Figure 28: Schematic of typical recrystallisation kinetics during annealing. [8]

The general form of the JMAK equation, assuming nuclei form at a rate of $\dot{N}$ and the grain growth rate is linear at a rate of $\dot{G}$, is given by:

$$X = 1 - \exp(-bt^n) \tag{9}$$

where X is the fraction recrystallised at time t, n is the JMAK exponent, and $b = f\dot{N}\dot{G}t^4/4$. The derivation is provided in the appendix (Section D).

2.4.4 Dislocation density

The increase in dislocation density results in an increase in stress required for plastic flow. The authors B. Dutta *et al.* [31] modelled the relationship between the change in flow stress and dislocation density as follows:

$$\sigma_f = C_1 + C_2\sqrt{N_d} \tag{10}$$

or

$$(\sigma_f - \sigma_0) = \alpha M G_m b\sqrt{N_d} \tag{11}$$

where $(\sigma_f - \sigma_0)$ is the degree of work hardening from yield strength to flow stress, α is a constant equal to 0.15, M is the Taylor factor, G_m is the shear modulus, b is the Burgers vector, and N_d is the dislocation density.

The most robust technique to determine dislocation density is the line intercept method, which consists of measuring the thickness of the TEM foil and counting the number of dislocations intersected by a grid of lines [32][33]. It should be noted that determining dislocation density accurately is notoriously difficult, especially if the foil thickness needs to be determined [34][35]. Figure 29(a) is a TEM micrograph of tempered and crept X20 steel. In this condition, the dislocation density is low at $\rho_{\text{TEM}} = 0.30 \pm 0.36 \times 10^{14}$ m^{-2}, therefore the number of dislocation intercepts can be easily identified. In Figure 29(b), a TEM micrograph of martensitic X20 steel shows a complex dislocation network with high dislocation density $\rho_{\text{TEM}} = 9.26 \pm 1.95 \times 10^{14}$ m^{-2}, making counting intercepts more diffi-

cult. However, it can still be done if the micrograph is observed under an optical microscope [35]. An alternative method is to use XRD, as described in Section 2.4.7.

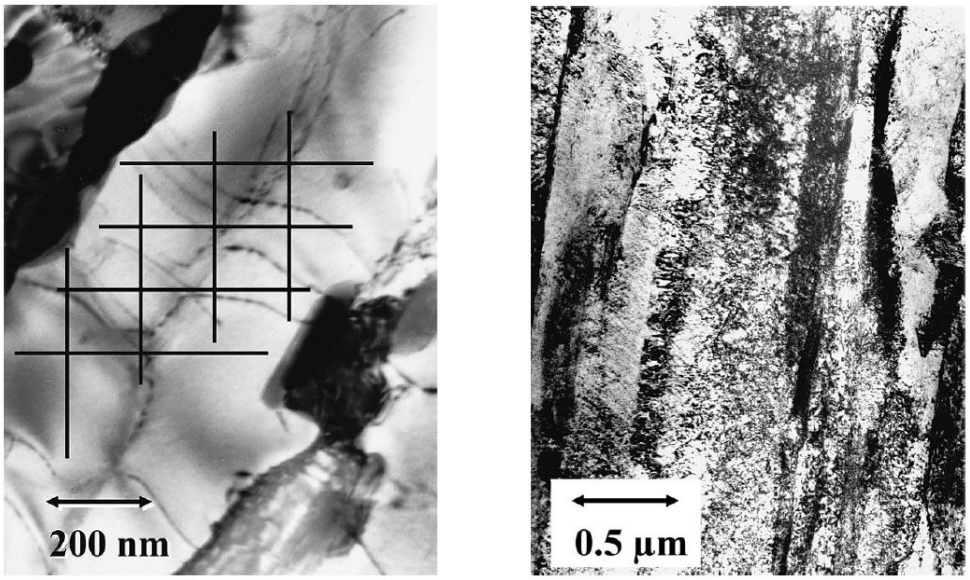

(a) Tempered X20 steel crept at 650 °C and 120 MPa with 1.2 % plastic strain.

(b) Martensitic X20 steel austenitized at 1050 ° for 1 h followed by air cooling.

Figure 29: TEM micrographs of X20 steel with (a) low dislocation density and (b) high dislocation density. [35]

2.4.5 Resistivity

All metal consists of a lattice of atoms with freely dissociated electrons. Applying electrical current results in the electrons drifting to the positive terminal. Electrical resistivity is the resistance to the flow of electrons and is dependent on various factors such as temperature, impurities, and the amount of plastic deformation. The arrangement of the crystal lattice structure directly affects resistivity and can therefore be used to quantify recovery and recrystallisation [36]. Work done on deformed Al is shown in Figure 27, where electrical resistivity measurements follow the power difference trend during heating.

2.4.6 Magnetic properties

Magnetic properties can be used to measure recovery and recrystallisation by measuring the change in the coercive field during the heating of ferritic steels [14]. Coercive field, denoted as H_c, is a magnetic property representing the force required to demagnetise a ferromagnetic material, measured in ampere/meter. It has the advantage of being non-destructive and can be related to mechanical properties. From experimentation, some theoretical statements have been found to relate coercive field H_c to dislocation density ρ, as follows [37]:

$$H_c \propto k_1\sqrt{\rho} \tag{12}$$

with k_1 being a constant.

2.4.7 XRD

A simple method using X-ray broadening data can be used to track recovery progress. The line sharpening parameter $\underline{R}$ is defined as follows:

$$\underline{R} = \frac{I_{\text{min}} - I_b}{I_{\text{max}} - I_b} \tag{13}$$

where I_{min} is the minimum intensity between $K_{\alpha 1}$ and $K_{\alpha 2}$ peaks, I_{max} is the maximum intensity of the $K_{\alpha 1}$ peak, and I_b is the background intensity. However, this method does not provide information about cell size or residual stresses but only the extent of recovery. By using $\underline{R}$, the rate of recovery can be determined if measurements are taken at various times [3]. However, various assumptions and approximations are made and are dependent on the type of microstructure, effect of instrument line broadening, fitting parameters, etc. [35].

Work done by G. K. Williamson and R. E. Smallman [38][39][40] found that the dislocation density can be related to the XRD data. Evidence from micro-beam experiments showed that the metal is broken into blocks with dislocations on the boundaries of the blocks (Figure 9(a)). Assuming there are n dislocations per block face, the total dislocation line length is $6nD/2$ (each face shared by 2 blocks), where D is the block dimension. The number of blocks per unit volume is $1/D^3$, therefore the dislocation density can be calculated from the particle size (i.e. block size) as follows [38]:

$$\rho = \frac{3n}{D^2} \tag{14}$$

To use this equation, the value of n must be assumed or determined. Assuming $n = 1$ gives the minimum dislocation density and may be applied when the dislocations are nearly random as with very deformed and fully annealed metals. From XRD line profile measurements, it is possible to obtain the strain distribution ζ. If $\overline{S^2}$ is the mean square strain of the distribution, then the stored energy of the lattice V is [40]:

$$V = \frac{3E\overline{S^2}}{2} = \frac{3EA\zeta^2}{2} \tag{15}$$

where A is a factor dependent on the shape of the strain distribution and E is Young's modulus. The energy of a screw dislocation v_c can be calculated in the absence of interaction with other dislocations as follows:

$$v_c = \frac{\mu \mathbf{b}^2}{4\pi} \ln\left(\frac{r}{r_0}\right) \tag{16}$$

where, **b** is the Burgers vector of the dislocation, μ is the shear modulus, r is the radius of the crystal containing the dislocation, and r_0 is a suitably chosen integration limit (usually 10^{-7} cm). However, dislocations interact, and the strain energy is changed by a factor F, therefore [38]:

$$v_{\text{real}} = v_c F \tag{17}$$

The dislocation density of strain broadening can therefore be calculated as follows [38]:

$$\rho = \frac{k\zeta^2}{F\mathbf{b}^2} \tag{18}$$

where $k = 6\pi EA/\mu \ln(r/r_0)$ for body-centered cubic metals, $k = 14.4$ has been found for **b** along [111]. Equation 18 can only be used when the factor F is known or assumed. The simplest is a model where $F = 1$ and with this assumption, one dislocation coincides with the edge of each block. Therefore, the dislocations have the maximum separation and minimum interaction. This model evidently is also where $n = 1$, which will result in Equations 14 (ρ_s) and 18 (ρ_p) being equal. However, there is an extreme situation where dislocations pile up at barriers in the slip plane, which is the mechanism considered for work hardening. This results in a large increase in strain energy per dislocation, therefore it can be argued that if there are n dislocations in each pile-up, they act as one Burger's vector $n\mathbf{b}$. The strain energy from Equation 16 will increase to $n^2 v_c$. Thus $F = n$ and the dislocation density ρ can be determined as [38]:

$$\rho_p = \frac{3}{D^2}, \quad \rho_s = \frac{k\zeta^2}{\mathbf{b}^2}, \quad \rho = \sqrt{\rho_s \rho_p} \tag{19}$$

J. Pesicka *et al.* compared dislocation densities determined using TEM line intercept method and XRD on X20 steel [35]. Good agreement was found in the martensitic condition in Figure 29(b) with $\rho_{\text{TEM}} = 9.26 \pm 1.95$ vs. $\rho_{\text{XRD}} = 9.40 \times 10^{14}$ m^{-2}. However, with low dislocation density Figure 29(a), the XRD result was approximately half of the TEM result, $\rho_{\text{TEM}} = 0.30 \pm 0.36$ vs. $\rho_{\text{XRD}} = 0.14 \times 10^{14}$ m^{-2}. This large discrepancy is attributed to TEM analysing a very small area, and XRD yielding average values of a much larger volume.

A study done by Gallet *et al.* [41] compared dislocation density measurements using XRD, electron channelling contrast imaging (ECCI), high resolution-EBSD (HR-EBSD) and TEM on duplex stainless steel. The comparisons were done on undeformed and low deformations of 5% and 10%. It was concluded that the imaging techniques, TEM and ECCI, and also XRD mainly give information on SSDs and HR-EBSD on GNBs. The schematic in Figure 30 shows which type of dislocations are visible using the above-mentioned techniques [41].

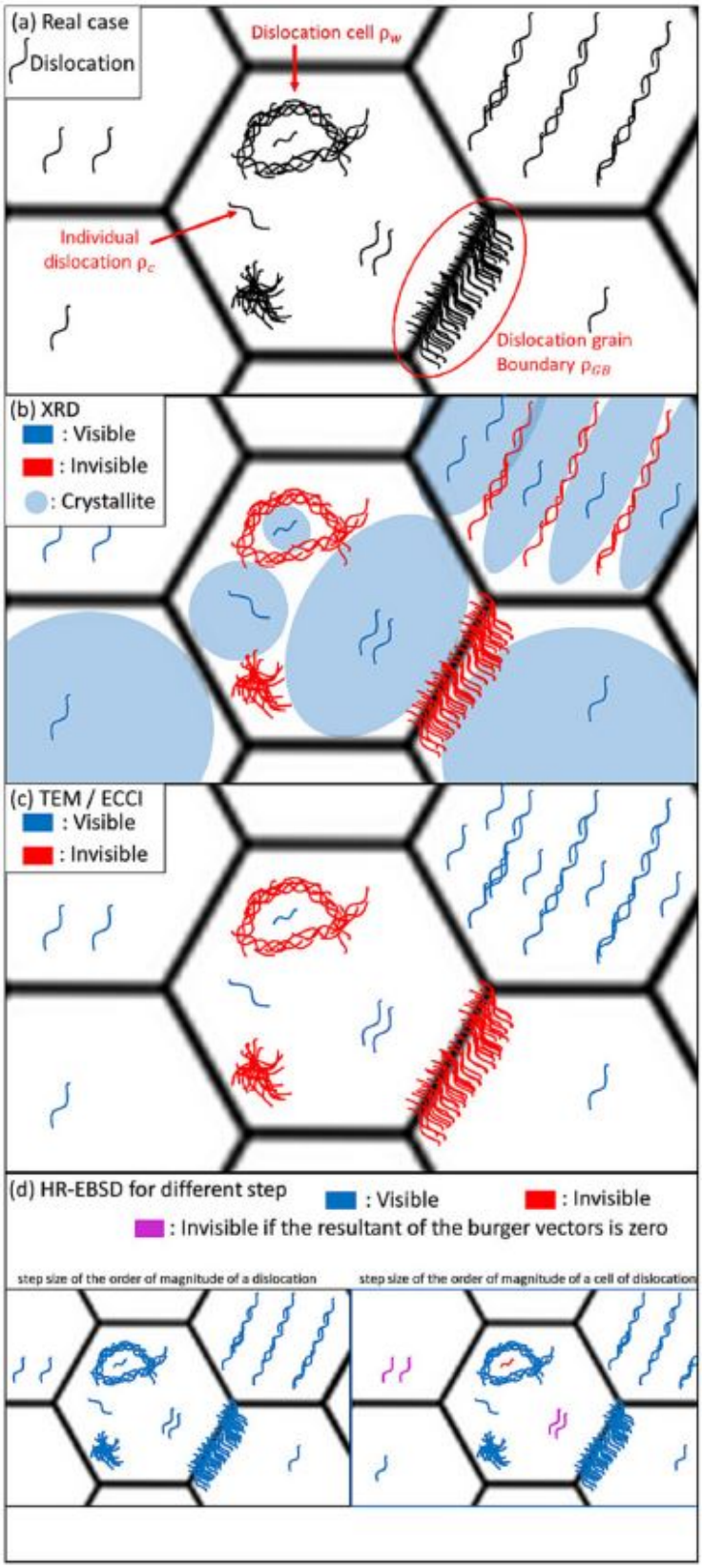

Figure 30: Schematic diagram of grain patterns showing which dislocations are visible using different techniques where ρ_c isolated dislocations, ρ_w dislocations of a cell and ρ_{GB} dislocations of a grain boundary. (a) Real case, (b) XRD, (c) TEM/ECCI and (d) HR-EBSD. [41]

2.5 Back-annealing

A summary of the practical use and challenges of back annealing was done by R. K. Ray, B. Hutchinson, and C. Ghosh [3] and serves as a baseline for this study. Back-annealing is widely used in the aluminium industry for thin sheets and foils with optimised strength-ductility balance for various applications. Recovery and partial recrystallisation annealing have also successfully been used in the production of thin tin plates. Currently, back-annealing is used industrially in the USA with reported yield strengths of 300-800 MPa. The Society of Automotive Engineers (SAE) states that recovery annealed sheets can be used for vehicle outer panels with a yield strength range of 490-830 MPa [42]. In Australia, back-annealing is applied during hot-dip galvanising [3].

Industrial back-annealing is viable only when consistent mechanical properties are obtained. There must be maximum temperature-time flexibility, in both fully recrystallised or recovered regions, as shown schematically in Figure 31 In general, the partial recrystallisation region should be avoided as small changes to temperature or time can result in inconsistent properties. However, some products are deliberately partially recrystallised depending on industrial applications. The aim is to increase the temperature range of the recovery annealing window. Increasing the amount of cold work in plain low-C steels increases the recovery and recrystallisation rates making it difficult to widen the window, especially in thin sheets. Reducing the amount of cold work is impractical since it limits the final thickness. High percentages of cold work coupled with V, Ti or Nb microalloy additions, as suggested by the SAE, retards the softening processes and helps to produce a thin gauge back-annealed sheet [3].

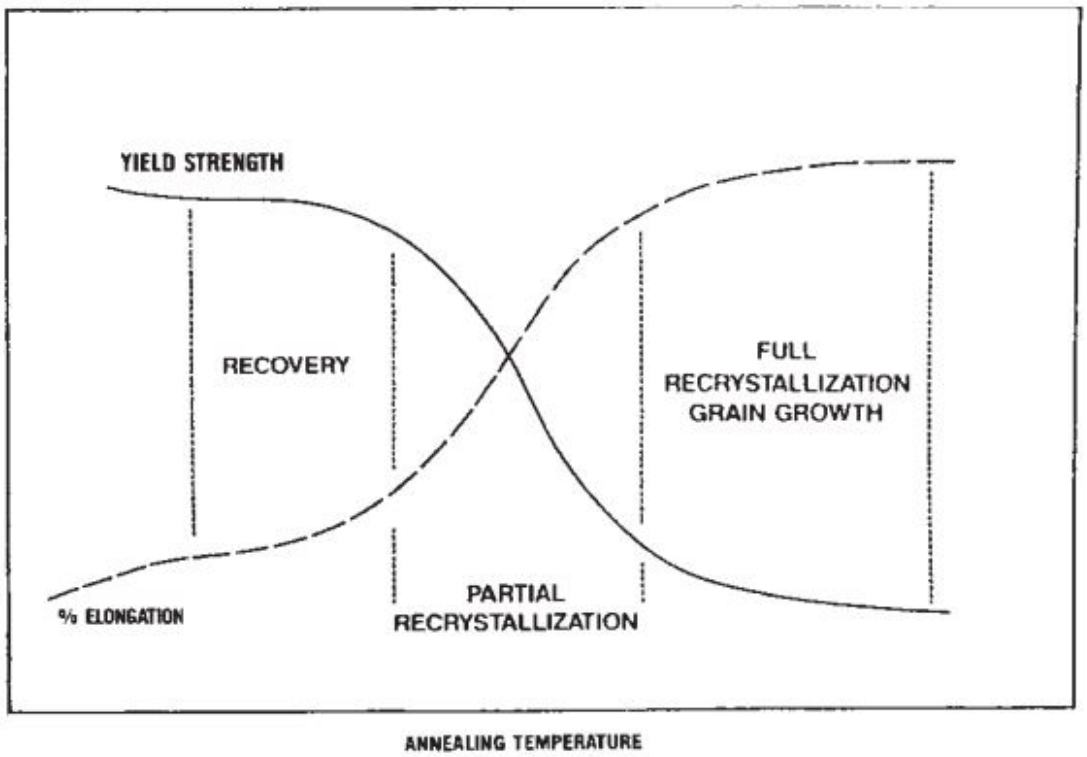

Figure 31: Schematic diagram showing the change of mechanical properties with increasing annealing temperature. [3].

In order to successfully produce low carbon recovery annealed steel with optimised mechanical properties, the following parameters should always be considered [3]:

- Steel chemistry (C, Mn, Al, Si, Nb, V, Ti);
- Hot rolling parameters (finishing and coiling temperature);
- Cold reduction and;
- Annealing (heating rate, time, maximum temperature and overageing).

Figure 32 shows the effects of Ti and Nb microalloying on the recrystallisation kinetics in low C. The carbon content of steels in this work varied between 0.08 and 0.12%. As may be seen, it appears that Ti is superior to Nb in retarding the recrystallisation and recovery processes. On the contrary, in interstitial free (IF) steels, Nb appears to be a stronger inhibitor of the recrystallisation process than Ti, Figure 33.

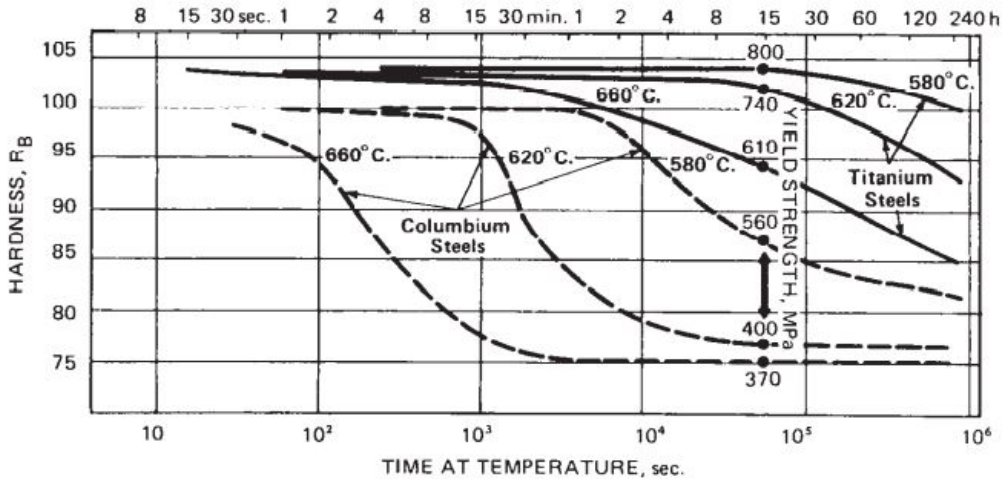

Figure 32: The effect of Ti and Nb (Columbium) addition on the recovery and recrystallisation kinetics of a low carbon steel. [3]

It is clear from Figures 32 and 33 that microalloying elements are beneficial for back-annealing because they contribute to subgrain, grain refinement and precipitation strengthening after cold rolling and back-annealing.

The amount of cold work affects the final strength and back-annealing properties. For every 10% cold reduction, there is an increase of approximately 50 MPa in tensile strength. However, smaller amount of cold work makes recovery and recrystallisation sluggish as was shown in work done on Nb steel by W. D. Kenny *et al*. for the development of back-annealed steels for automotive bumper reinforcements. Figure 34 shows annealing curves at various cold reductions for a 0.09C, 0.6Mn, 0.33Si, 0.02Nb steel [43]. As may be seen, smaller percentages of cold work extend the back-annealing window slightly, except for the 40% cold work where a significant extension is observed. In this work, the steel thicknesses ranged between 1.4 and 1.6 mm, which is relatively thick compared to the present-day requirements for automotive and roofing. Although smaller amounts of cold work are a viable option to optimise back-annealing, the limitation on the final thickness makes it unattractive.

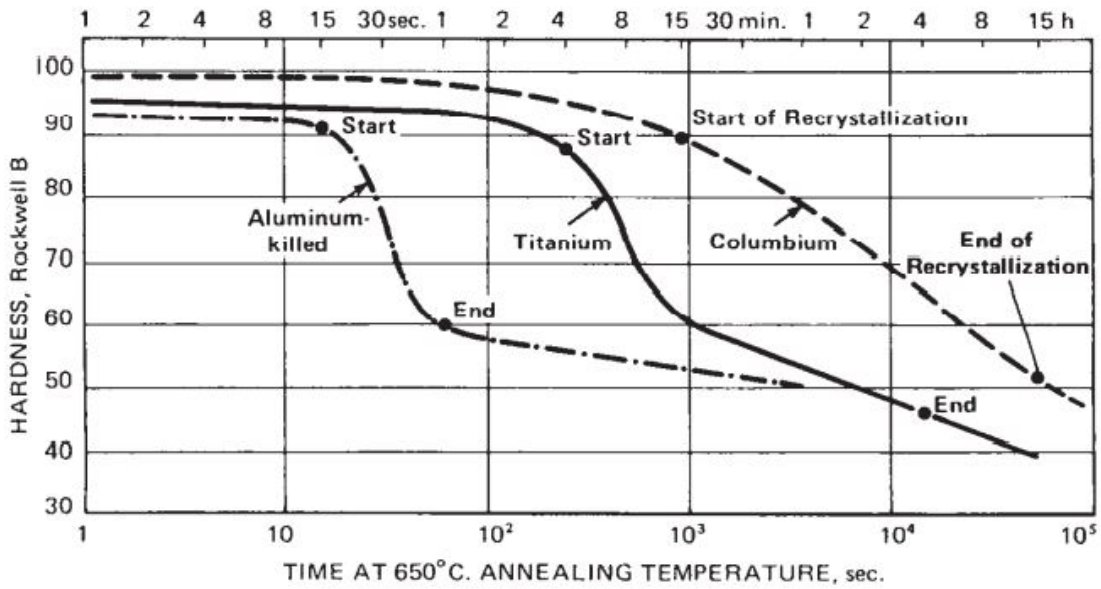

Figure 33: The effect of Ti and Nb (Columbium) addition on the recovery and recrystallisation kinetics of an IF steel. [3]

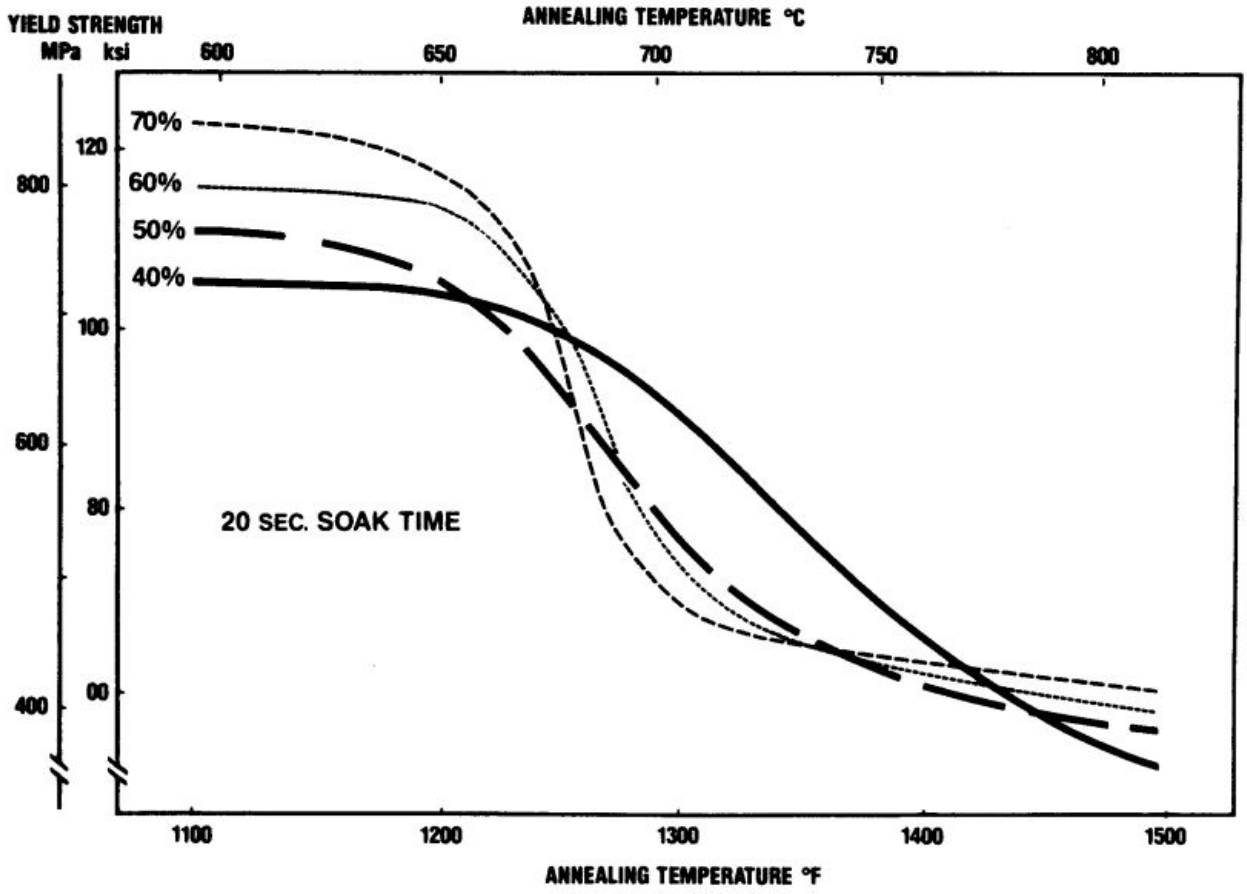

Figure 34: Yield strength of Nb 0.02% steel vs. annealing temperature with various degrees of cold works. [43]

The annealing time and temperature are the final means to control the mechanical properties of back-annealed products. To effectively compare data, Larsen and Salmos [3][44] defined a factor M which combines both time and temperature:

$$M = (T + 273)(logt + 20) \times 10^{-3} \tag{20}$$

where T is temperature in °C and t time in seconds. M_{rs} is defined as the recrystallisation start condition, Ray et al. [3] reported the following regarding M_{rs}:

- Plain carbon steel 18.7-19.7.
- Nb steel 19.3-20.8.
- V-N steel 19.6-20.8.

When optimising the back-annealing window the M_{rs} value can be used to compare different parameters and steels. Figure 35 is an M plot of 70 % cold worked 0.03V-0.009N, 0.10V-0.009N and plain carbon steel. This data has been replotted from an unpublished report [3]. Both the prior hot rolling processing conditions and the amount of carbon content of the plain carbon steel are not known but the results give a good insight into the effect of vanadium additions on M_{rs}. Even small additions of vanadium increase the M_{rs} to ∼19.8 compared to the M_{rs} of the plain carbon which is ∼18.7. However, microalloying elements do not improve the softening slope after recrystallisation has started [3]. Again, this emphasises the fact that to apply back-annealing commercially, good control during annealing is essential for M_{rs} not to be exceeded. An exception is the case of partially recrystallised products which require more stringent design and control.

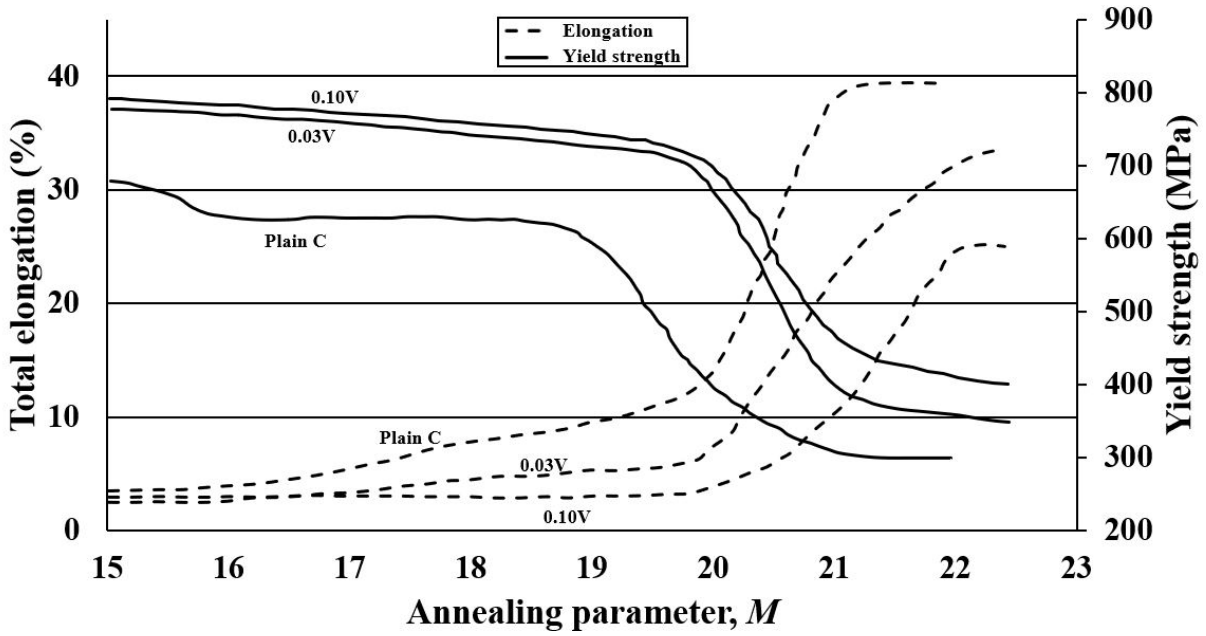

Figure 35: Yield strength and elongation vs. *M* for 70 % cold worked plain carbon, 0.03V-0.009N and 0.10V-0.009N steels. [3]

Ray *et al*. showed how various strength-ductility combinations can be obtained by back annealing using data from various sources, Figure 36. For 70% cold work continuous annealed vanadium high strength low alloy (HSLA) steels, yield strengths of 610 to 820 MPa and elongations of 3 to 12% are achievable with back annealing.

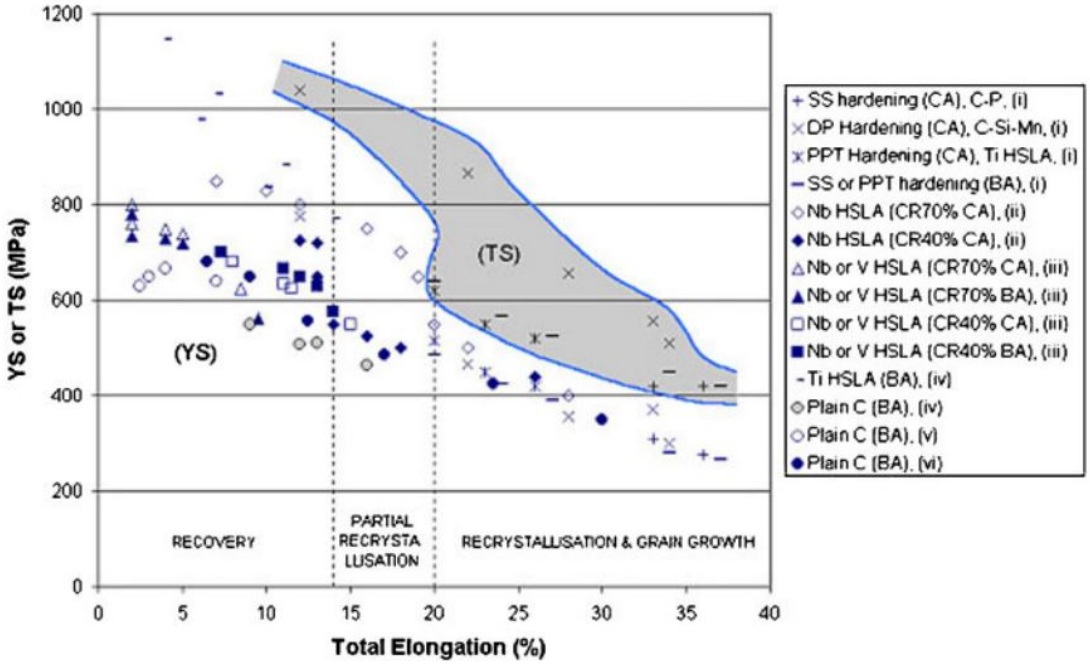

Figure 36: Strength-ductility combinations of various steels subjected to various processing conditions. [3][45][46][47]

Chapter 3: Experimental procedure

3.1 Materials and industrial processing conditions

Tables I, II, and III shows the chemical compositions, processing conditions, and hot rolling temperatures of the investigated steels.

Table I: Chemical compositions of steels used in study.

Steel	C	Mn	V	Al	Si	N	Nb	Ti
1	0.078	0.730	0.001	0.039	0.00	0.0070	0.020	0.025
2	0.079	0.887	0.054	0.030	0.19	0.0102	0.001	0.002
3	0.062	0.410	0.000	0.047	0.01	0.0040	0.000	0.001
4	0.146	1.312	0.049	0.003	0.46	0.0097	0.000	0.001

Table II: Alloy systems and manufacturing conditions of steels.

Steel	Alloy system	Condition
1	Low C-Nb-Ti	Industrial cast and rolled
2	Low C-V-N	Industrial cast and lab rolled
3	Plain low C	Industrial cast and rolled
4	C-Mn-V-N	Lab cast and rolled

The manufacturing processes for the steels were as follows:

- Steel 1 was industrially hot-rolled to a thickness of 3.5 mm from an initial thickness of 240 mm. This process was followed by industrial descaling of oxide film by both mechanical and chemical methods. Subsequently it was cold-rolled to thicknesses of 1.56 mm and 0.53 mm.
- Steel 2 was industrially cast and hot-rolled using a laboratory hot-rolling mill. A sample of the industrial cast was cut into sections of 95 mm thickness which was hot rolled to a thickness of 8.5 mm. The mill setup involved no controlled cooling, with a hot rolling finishing temperature of approximately 900 °C. The steel was then air-cooled at an average rate of 5 °C/s to room temperature and further cold-rolled in a mini mill to 1.0 mm.
- Steel 3 was industrially hot-rolled to a thickness of 2.2 mm from an initial thickness of 240 mm. This process was followed by industrial descaling of oxide film by both mechanical and chemical methods. Subsequently is was cold-rolled to thicknesses of 0.76 mm and 0.38 mm.
- Steel 4 was laboratory-melted using a laboratory induction furnace and casted in a 100 mm diameter mould and underwent similar laboratory hot rolling conditions as steel 2 it was however also cold rolled to 3.8 mm.

3.2 Annealing simulations

Section of 10×6 mm were cut from the middle of flat cold rolled samples. Laboratory back-annealing simulations, based on an industrial HDG plant, were conducted using a Bähr Deformation Dilatometer

Table III: Rolling parameters of steels.

Steel	Reheat temperature (°C)	Hot rolling finish T (°C)	Coiling T (°C)	Cold reduction %
1	1200	880	625	55, 85
2	1175	900	Air cool	85
3	1200	880	625	66, 83
4	1175	900	Air cool	55, 85

DIL 805A/D. The atmosphere was vacuum thereafter cooled with helium at cooling rates greater than 10°C/s. Type K thermocouple was used to measure temperature and placed in the middle of the sample as shown in Figure 38. Line speeds of 30 and 110-120 m/min were simulated with the 110 m/min cycle outlined in Figure 37, while detailed information on line-speeds and temperatures can be found in Table A.1. T_{max} represents the maximum temperature attained during the simulated annealing cycles, always occurring during the initial heating phase, as illustrated in Figure 37. The M values were calcualted using the T_{max} and the time at distance of 33 m, which is the maximum M value, for 110 m/min the time was 18 s as shown in Figure 37.

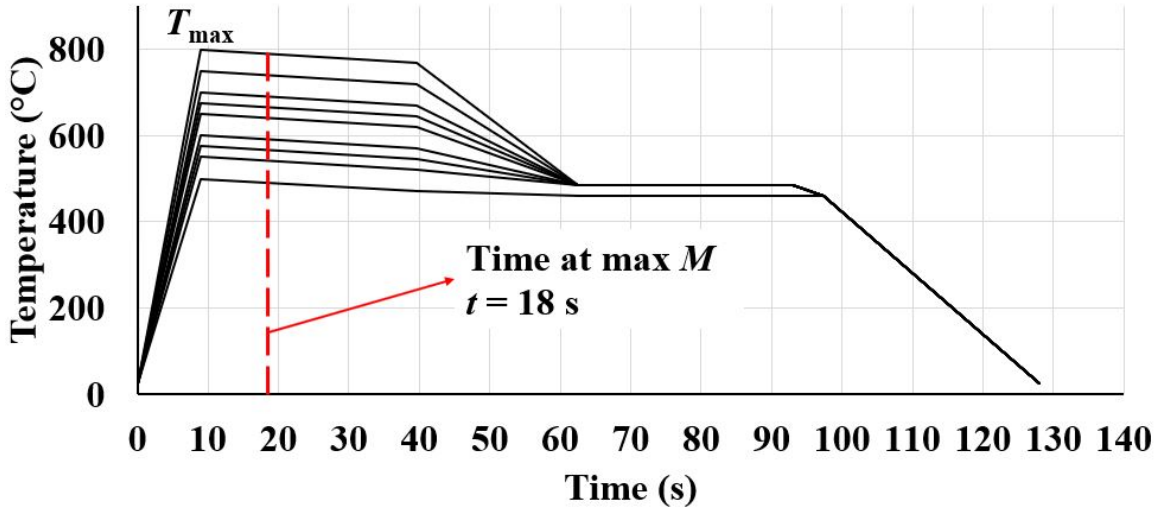

Figure 37: Time and temperature of the 110 m/min annealing cycles simulated in the Bähr dilatometer.

3.3 Sample preparation for hardness and optical microscopy

After annealing, the samples were mounted in bakelite resin, polished, and prepared for metallographic analysis following ASTM E407 standards. Hardness measurements were conducted using a micro Vickers machine with a 500 g load, the hardness reported was the average of three measurements per site. Microstructures were examined using an Olympus BX51M 1 light optical microscope. The analysis directions are depicted schematically in Figure 38.

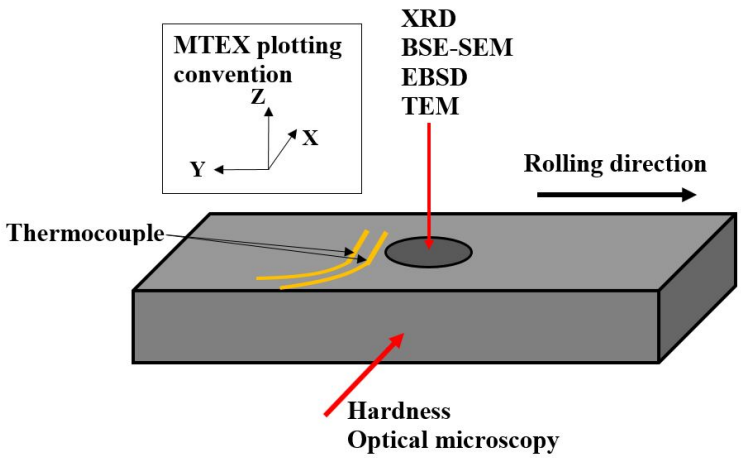

Figure 38: Schematic diagram indicating the position of experimental analyses.

3.4 Fraction recrystallised plots

JMAK type plots (Equation 9) were generated using hardness (H_i) vs. M data from the onset of softening. Third-order polynomials were fitted to the data to obtain H_i as a function of the parameter M. The resulting polynomials were then used to calculate the fraction recrystallized (f_i). Subsequently, plots of $ln(ln(1-f_i))$ vs. $ln(M_i)$ were created, accompanied by fitted linear trend lines.

3.5 Sample preparation for electron microscopy

For XRD, BSE-SEM, and EBSD analyses, 3 mm diameter discs were wire-cut, as illustrated in Figure 38. These discs were subsequently mounted in bakelite resin and polished to a colloidal finish. The polishing process involved using grit papers with increasing fineness (P400, P800, and P1200) and diamond suspensions of 6, 3, 1, and 0.25 µm, in that order. A final polish was achieved using an acid-base solution and a 0.05 µm colloidal silica suspension.

Thin slices of the fully recrystallised samples (5×5 µm and 100 nm) were analysed using an annular dark field scanning transmission electron microscope (ADF-STEM). Additionally, the samples underwent preparation and analysis using the bulk replication technique (BRT). In BRT, the iron matrix surrounding the precipitates was selectively dissolved, leaving the precipitates intact. These isolated precipitates were then embedded in a carbon film, and examined using the TEM. However, BRT has inherent limitations, especially with smaller precipitates, where the extraction efficiency can be compromised [48] (i.e., tiny precipitates may not adhere well to the carbon film).

3.6 Estimation of the dislocation density from XRD data

As discussed in Section 2.4.7, the dislocation density can be estimated using XRD data. Crystallite size and microstrain can be calculated from the peak profile broadening, as explained in Section B in the appendix (refer to the relevant equations provided therein). The underlying assumption is that the peak broadening solely arises from dislocations (microstrain) and crystallite size after subtracting

the broadening due to instrumental effects. Crystallite size represents an area that diffracts coherently and can either be a whole crystallite or a domain within a crystal. Deconvolution of the XRD peak breadths is performed to extract microstrain and crystallite size. In this study, the deconvolution method employed was Rietveld refinement, as described in the works by Ungár [34] and Balzar *et al.* [49].

The XRD patterns were acquired using a laboratory Bruker D2 Phaser diffractometer in Bragg Brentano geometry. The instrument specifications are detailed in Table IV, with a step size of 0.02° used from 2θ values of 20° to 120°. Instrumental line broadening was determined using the LaB_6 NIST 660c standard sample [50], and the resulting pattern was fitted through Rietveld refinement. The angular dependence of the instrument was modelled using TOPAS^{TM}, and the resulting line broadening coefficients were fixed for subsequent sample refinements [51]. Line broadening for the samples was visually inspected for the (110), (200), and (211) peaks.

The XRD data were imported into the TOPAS^{TM} software for the quantitative determination of crystallite size and microstrain. During refinement, an alpha-iron crystal structure with $a_0 = 2.87$ was utilised. Line broadening due to crystallite size was assumed to be Lorentzian, and Gaussian for the strain component. Fundamental parameters line profile fitting (FPPF) was employed in conjunction with Rietveld refinement to fit the peaks. A Chebyshev polynomial of order 3 was fitted to the background XRD data. The crystallite size was obtained as the ”LVol-IB” parameter, and the microstrain was represented as ϵ_0, indicating the total microstrain in the sample. It is important to note that the TOPAS^{TM} software assumes that strain exhibits both Gaussian and Lorentzian characteristics.

To calculate dislocation density using Rietveld refinement, the formula by Soleimanian and Mojtahedi was employed [52]:

$$\rho = \sqrt{\rho_D \rho_S} = \frac{2\sqrt{3}\sqrt{\langle \epsilon^2 \rangle}}{\mathbf{b}\langle D \rangle} \tag{21}$$

where $\langle \epsilon^2 \rangle = \epsilon_0$ and $\langle D \rangle$ is the crystallite size as determined from Rietveld refinement. Equation 21 is based on the foundational work done by Williamson and Smallman and is similar to Equation 19, where ρ_D represents dislocation density derived from crystallite size, ρ_S represents dislocation density due to microstrain, and **b** represents the Burgers vector.

In cases with low dislocation densities and large crystallite sizes, such as in fully recrystallized structures, the technique becomes less sensitive to the microstructure. Consequently, small changes in dislocation density and crystallite size do not significantly alter XRD peak width and may not be detected during fitting. However, in situations with large dislocation densities and small crystallite sizes, as seen in cold-rolled conditions, even minor changes are highly sensitive and can be detected [49].

3.7 EBSD analysis

The EBSD scan was done at 250× magnification with a step size of 0.5 μm and 1000× magnification with a step size of 0.1 μm. The indexing success rate was >95%. Subsequent analyses on the EBSD data was conducted using the MATLAB®-based MTEX toolbox [53][54][55], with the plotting convention

Table IV: Specifications of instrument used during XRD analysis.

Aspect	Value
Geniometer - primary and secondary radii (mm)	70.7
Detector - Linear PSD 2θ angular range (°)	3.242
Slits - Secondary Söller (°)	2.5
X-ray source Co $K_{\alpha 1}$ (Å)	1.789
X-ray source Co $K_{\alpha 2}$ (Å)	1.793
Operational setting	30 kV, 10 mA

illustrated in Figure 38. The phase identified was BCC Alpha Fe ($a_0 = 2.866$ Å). Grains consisting of 5 or fewer pixels were excluded. Grain boundaries were defined as misorientations greater than 15° and subgrain boundaries were between 2 and 15°. The resulting data was used to create subgrain plots showing grain boundaries as solid black lines and subgrain boundaries thinner blue lines.

Grain misorientations were calculated by comparing each grain's orientation with the grain reference orientation (GROD-OA), representing the average grain orientation. Grain orientation spread (GOS) maps were generated, indicating the averaged misorientation angle of the reference orientation deviations. Subsequently, pole orientation plots were created in the (001), (101), and (111) directions. The MATLAB®-based MTEX toolbox code used is in appendix E.

3.8 TEM analysis

The ADF-STEM technique was employed to qualitatively image dislocation structures in the steel samples. The analysed area measured 5x5 µm^2, resulting in 2048x2048 pixel images. The STEM-probe convergence semi-angle was set at 18 mRad, and an annular dark field (ADF) detector was utilised. The camera length was adjusted to capture signals within collection angles of 20 mRad (inner) and 47 mRad (outer).

In addition, energy-filtered TEM (EFTEM) was utilised to map the precipitates on extraction replica samples. Signals for N (red), V (green), and Ti (blue) were overlaid to produce RGB (red, green, and blue) composite images.

3.9 Industrial trial

An industrial trial followed the laboratory annealing simulations, where the optimal annealing temperature, determined based on hardness, was identified. The trial material had a chemistry similar to that of Steel 2 (Table I). The parameters of the hot strip mill and the amount of cold work applied are summarised in Table V. The hot-rolled strip thickness was 2.5 mm, and it was further cold-rolled to thicknesses of 0.47 mm and 0.55 mm. Samples were obtained both before and after galvanising, taken from the front ends of the coils, for subsequent hardness, tensile tests, and microstructural analysis.

Table V: Rolling parameters applied during the industrial trial.

Coil	Hot rolling finish T (°C)	Coiling T (°C)	Cold reduction %
1	880	625	81
2	840	575	81
3	880	625	78
4	840	575	78

3.10 Tensile tests of industrial samples

Tensile tests were performed using a 100 kN MTS tensile machine. Specimens were wire cut into tensile specimens with 75 mm gauge length. The 75 mm gauge length elongation was converted to 80 mm gauge length elongation using the Oliver equation [56]. The ramp rates during tensile testing were 1.125 mm/min in the elastic region and 30 mm/min in the plastic region as in ASTM E8.

Chapter 4: Results

The results of the partial annealing and restoration processes of the steels are presented in this chapter. Section 4.1 compares the effect of deformation on recrystallisation rates for steels 1, 3, and 4. Section 4.2 is the comparison of restoration processes in highly deformed (85%) steels 1, 2, and 3. Subsequent sections (4.3, 4.4, 4.5) compare the microstructures of the highly deformed (85%) Nb-Ti steel 1 and V-N steel 2 using optical, EBSD, and TEM techniques, respectively. Dislocation density results obtained from XRD data are compared between steels 1 and 2 in Section 4.6. The outcomes of the industrial trial are discussed in Section 4.7.

4.1 Influence of the amount of deformation on the back-annealing process

Figure 39 shows the change in hardness of Nb-Ti steel 1, plain C steel 3 and V-N steel 4 after high cold reductions of 83-85% versus low cold reductions of 55-66% with increasing M value. As may be seen, the higher cold reductions are harder than the low cold reductions with the C-Mn-V-N showing the highest hardness due to the increased precipitation strengthening from the high amount of C. There is an increase in hardness during the back-annealing process and was found to be higher in high-deformation samples. The higher dislocation density in the higher deformation samples served as extra driving force for the nucleation of fine precipitates which rendered the steel harder. This is evident from the plot of change in hardness versus M between M values of 0 to 16, Figure 39. As expected, on the contrary, the plain C steel did not exhibit this type of behaviour.

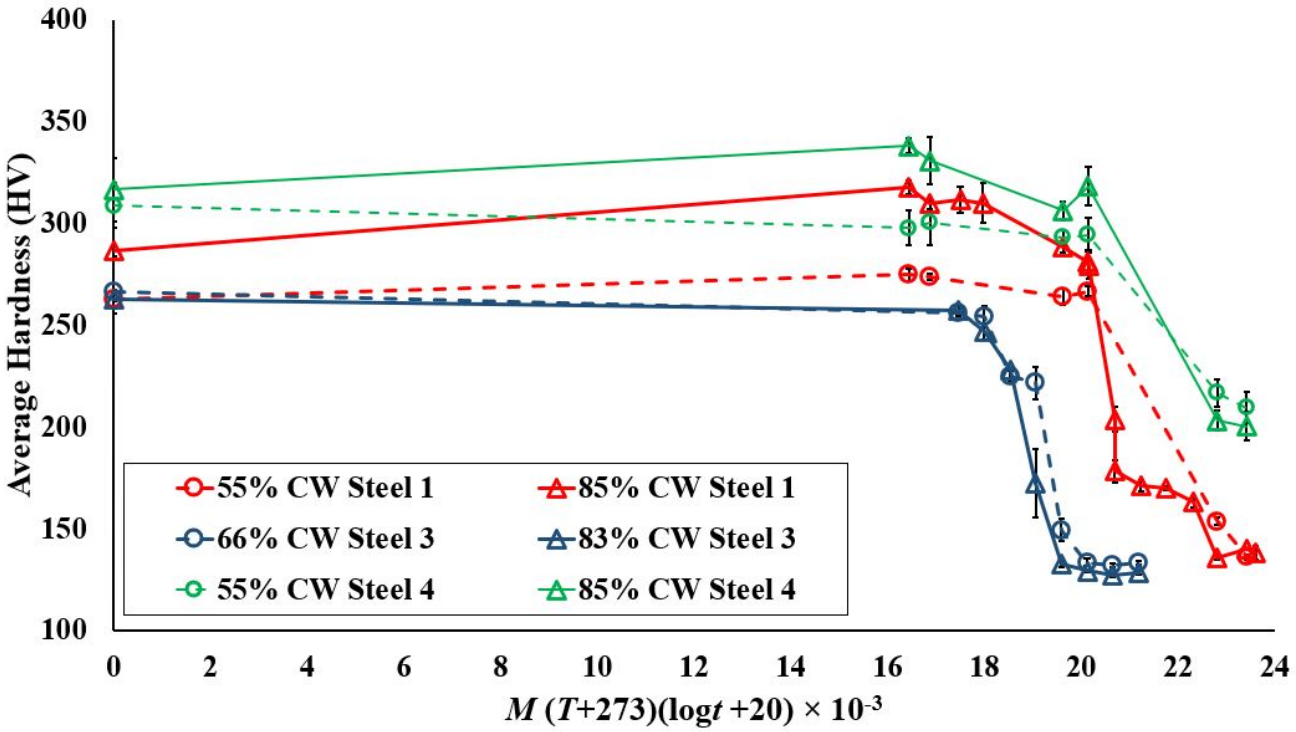

Figure 39: Annealing simulations: hardness vs. M for the Nb-Ti steel 1, plain C steel 3 and V-N steel 4 with low 55-66% and high 83-85% cold work. Time t in seconds.

4.2 A comparison of the restoration process of V-N versus plain C and Nb-Ti steels

Figure 40 shows the change in hardness with increasing M value of the studied steels after 83-85% cold working and annealing simulations. The Nb-Ti steel exhibited a higher as-cold-rolled hardness compared to V-N steel and this could be attributed to the differences in the contribution of the precipitation strengthening. The jagged nature of the curves at the onset of softening of the microalloyed steels could be due to the alternating softening and strengthening mechanisms of recovery and precipitation [3]. The restoration rate in the partial recrystallisation region is somewhat comparable between the three steels with rapid softening occurring after M_{rs} i.e. full recrystallisation region follows thereafter with, the Nb-Ti steel exhibiting some recrystallisation arrest at M value of 21.3, which could be attributed to precipitation of Nb(C,N). Consequently, the V-N steel reaches full recrystallisation earlier at M of 21.3 compared to 22.8 for Nb-Ti.

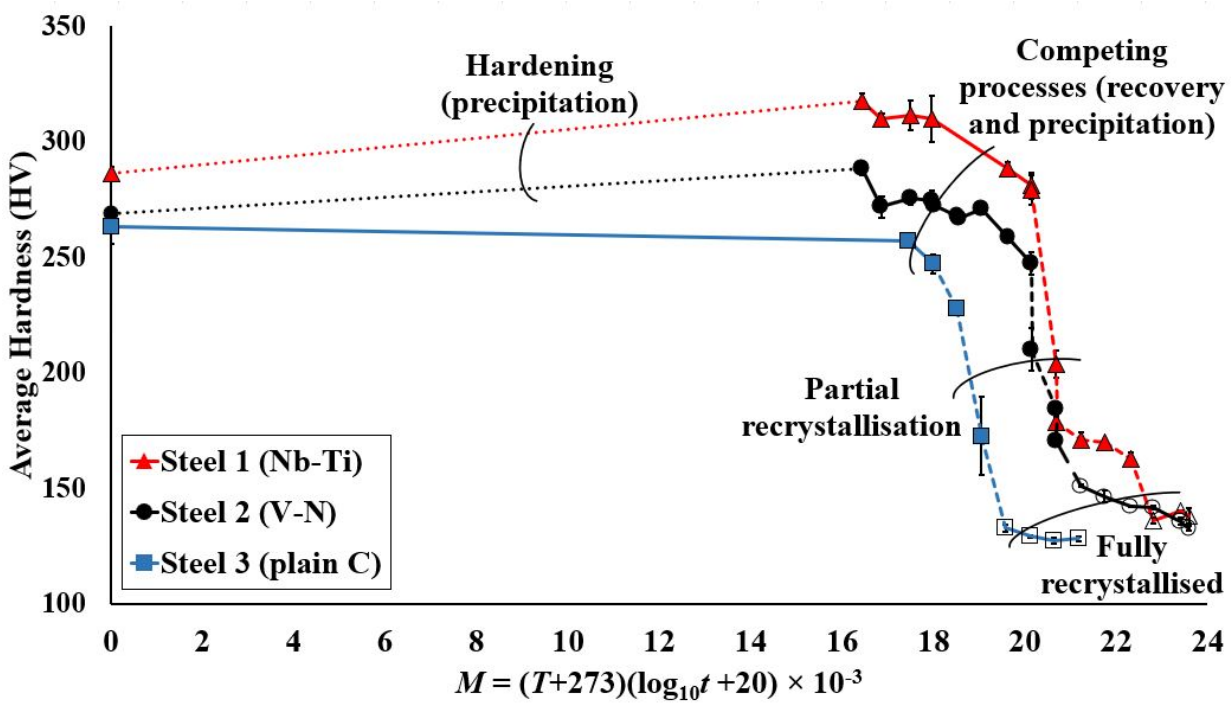

Figure 40: Annealing simulations: hardness vs. parameter *M* for steels 1, 2 and 3 with 85% cold work showing different stages of the restoration process. Time *t* in seconds.

Figure 41 highlights the critical area of recovery in Figure 40 and shows M_{rs} values of the steels. It is quite clear that the microalloying elements substantially extend the recovery window, with M_{rs} of 20.1 for Nb-Ti and V-N steels as opposed to 18.0 for plain C steel. The M_{rs} of V-N and Nb-Ti agrees with ranges observed by R. K. Ray et al.[3].

Figure 42 is derived from 3rd order polynomials fitting to the data for the plain C and V-N steel in Figure 41. The Nb-Ti steel was excluded because of the recrystallisation arrest since JMAK could not account for it. As expected, the V-N steel exhibited temper resistance due to the precipitation strengthening from the V(C,N) [4].

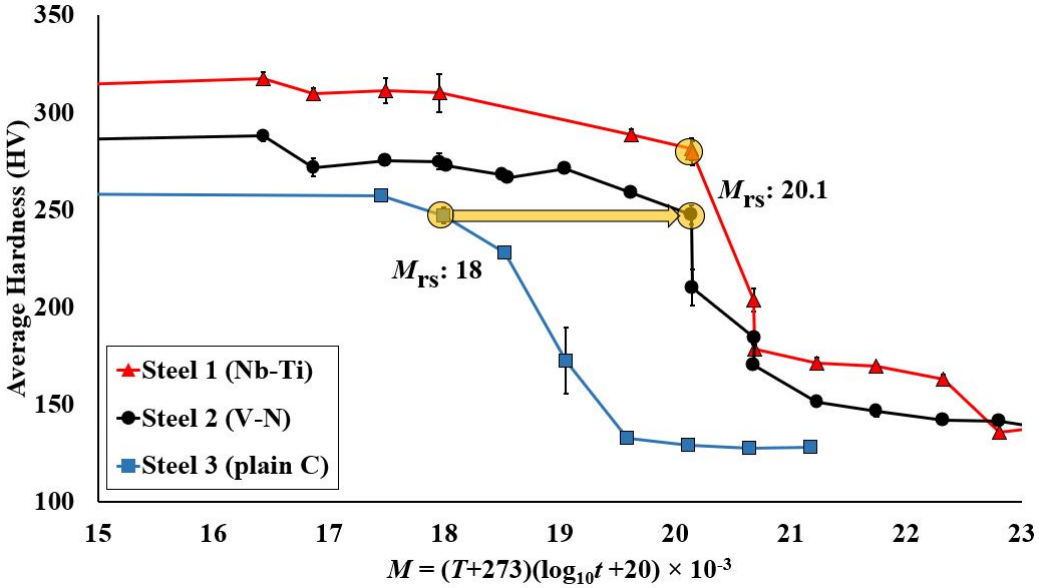

Figure 41: Annealing simulations: hardness vs. *M* of steels 1, 2 and 3 with high amounts of cold work showing the magnified recovery region in Figure 40. Time *t* in seconds.

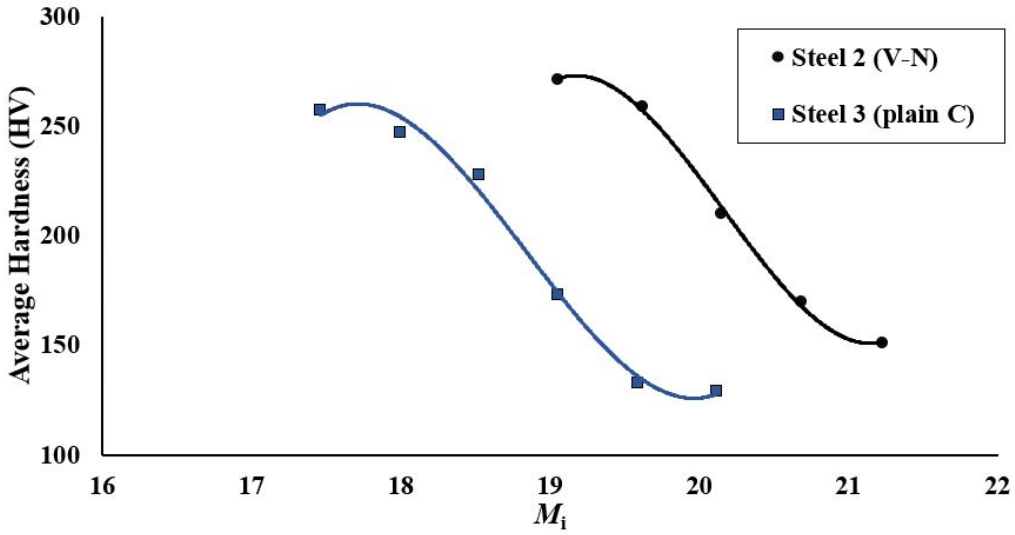

Figure 42: Polynomial fit done to hardness vs. *M*.

Table VI: Polynomial constants.

	A	B	C	D
Steel 2 (V-N)	31.74615	-1920.07694	38617.35088	-258058.72667
Steel 3 (plain C)	23.44818	-1325.06320	24870.56574	-154845.49060

The resulting JMAK plots from the polynomials are seen in Figure 43. The higher y-intercept of -129 for the plain C compared to -164 for V-N indicates an earlier recrystallisation start. The slope for the V-N steel is higher at 54 compared to 44 for plain low C which is an indication that the V-N steel recrystallisation rate is slightly faster which is also observed in the *M* plot, Figure 41. As suggested by others this is due to the initial retardation effect of precipitates followed by acceleration due to increased stored energy and PSN as discussed in Section 2.2.7.

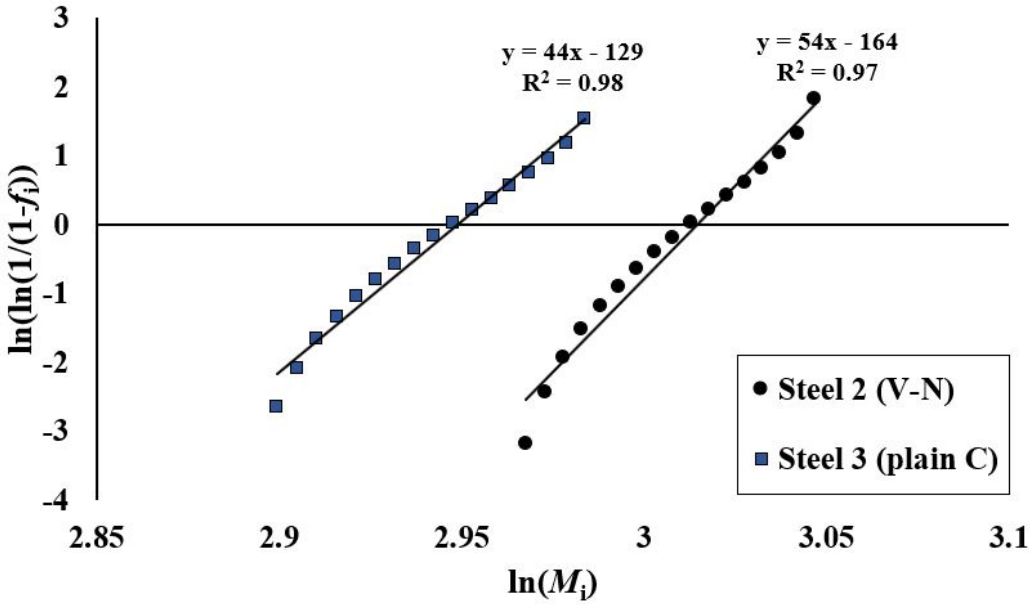

Figure 43: JMAK plots.

As expected, Figure 44 shows that the temperature-hardness trends are similar to those found in the M plots for both simulated line-speeds of 30 and 110 m/min, Figure 41. Compared to plain C, the V-N and Nb-Ti steels exhibited an increase in the recrystallisation start temperature by 50 °C, while the Nb-Ti steel with the faster line speed of 110 m/min increased by 100 °C. As may be seen, the rapid annealing cycles, *i.e.* shorter residence times, do not affect the recrystallisation start temperature significantly. The S700GD UTS range of 750 to 910 MPa (converted to hardness [57]) can be achieved with a T_{max} range of 550 to 650 °C using the V-N steel.

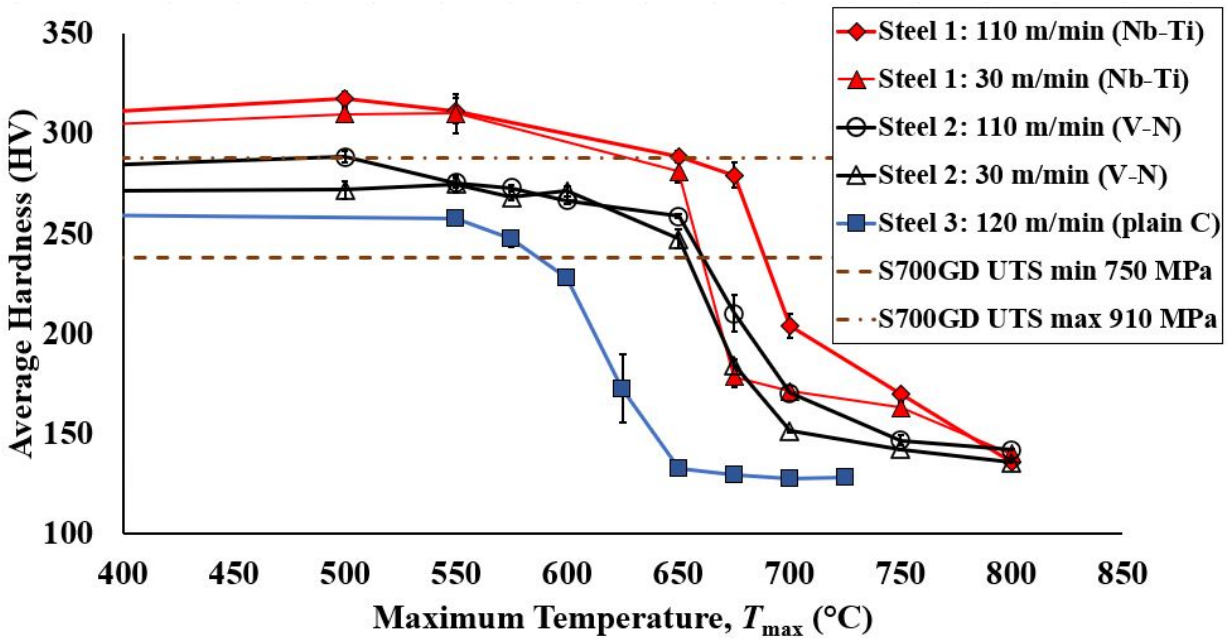

Figure 44: Annealing simulations: hardness vs. T_{max} in steels 1, 2 and 3 with linespeeds of 30 and 110 m/min.

4.3 Microstructural analysis

Figure 45 shows the evolution of the annealed microstructure as a function of T_{max} for the V-N steel at a constant line-speed of 110 m/min. From the as-cold-rolled condition up to a T_{max} of 600 °C, no significant changes to the highly deformed morphology were optically observed. At 650 °C there is evidence of new grains starting to form in the deformed matrix. The material was partially recrystallised at 675 °C and fully recrystallised at 700 °C. Grain coarsening commenced at 750 and 800 °C. During recovery, there were no substantial changes to the microstructures with regard to the formation of new grains. Some degree of softening occurred at 650 °C with no significant changes to the microstructures providing evidence that recovery occurred and that some degree of formability was restored while still retaining the high strength inherited from cold rolling.

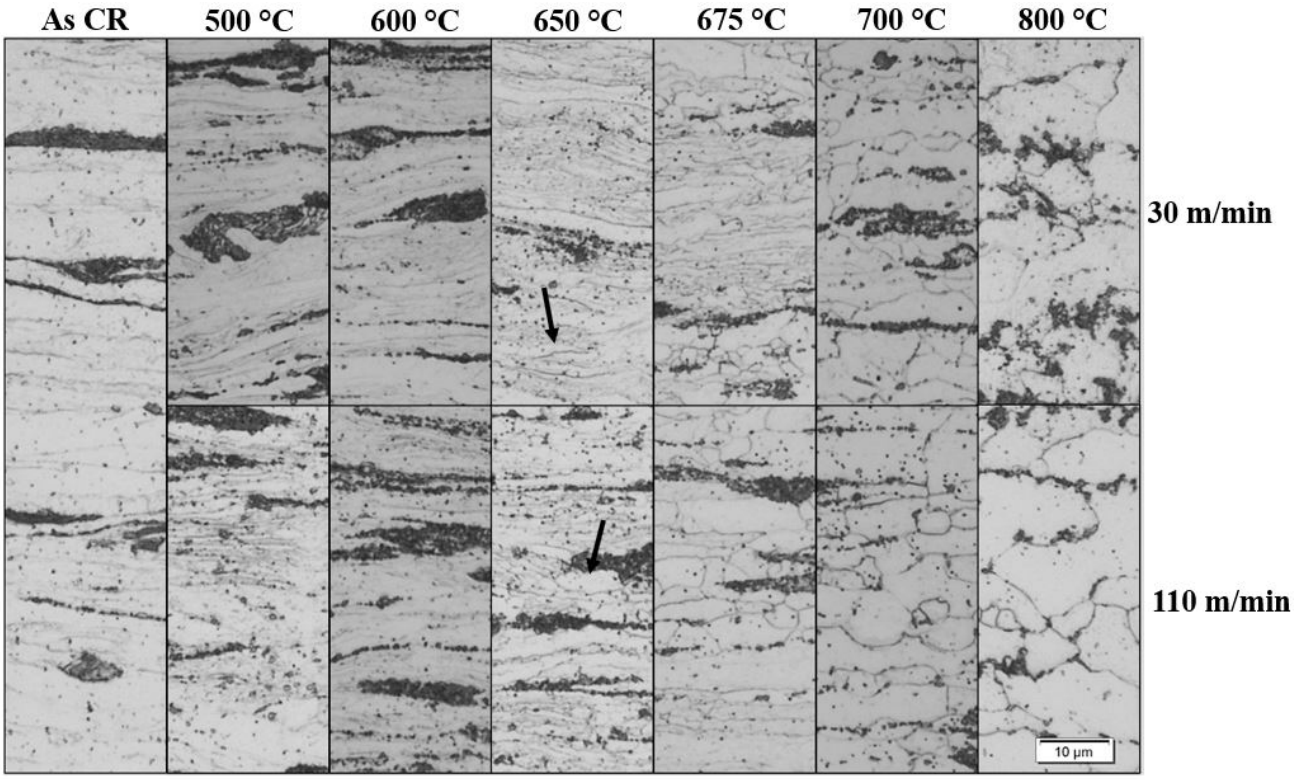

Figure 45: Annealing simulations: optical micrographs showing the evolution of microstructures with annealing temperature in V-N steel at simulated line-speed of 30 and 110 m/min respectively; the arrows indicate newly formed grains at 650 °C.

Similarly, the Nb-Ti only showed evidence of recrystallisation starting at 650 °C, Figure 46. The lower hardness observed in Figure 44 at a simulated line-speed of 30 m/min corresponds with a recrystallised structure in Figure 46, this is possibly due to insufficient time available for precipitation of Nb(C,N) at a simulated line-speed of 110 m/min.

From an internal investigation at IMMRI a similar arrest in hardness was found at a temperature of 700 °C on a 60% cold worked 0.08C-0.049Nb-0.019Ti steel during annealing simulations [58]. It was attributed to ferrite grain boundary mobility being inhibited due to solute drag and precipitate pinning. Bellavoine found on a 50% cold rolled 0.075C-0.028Nb-0.027Ti that with faster heating rates

as is the case with 110 m/min the recrystallisation temperature was shifted higher and could be due to less time available for precipitation, resulting in a decreased effect of precipitate pinning on retarding recrystallisation [59].

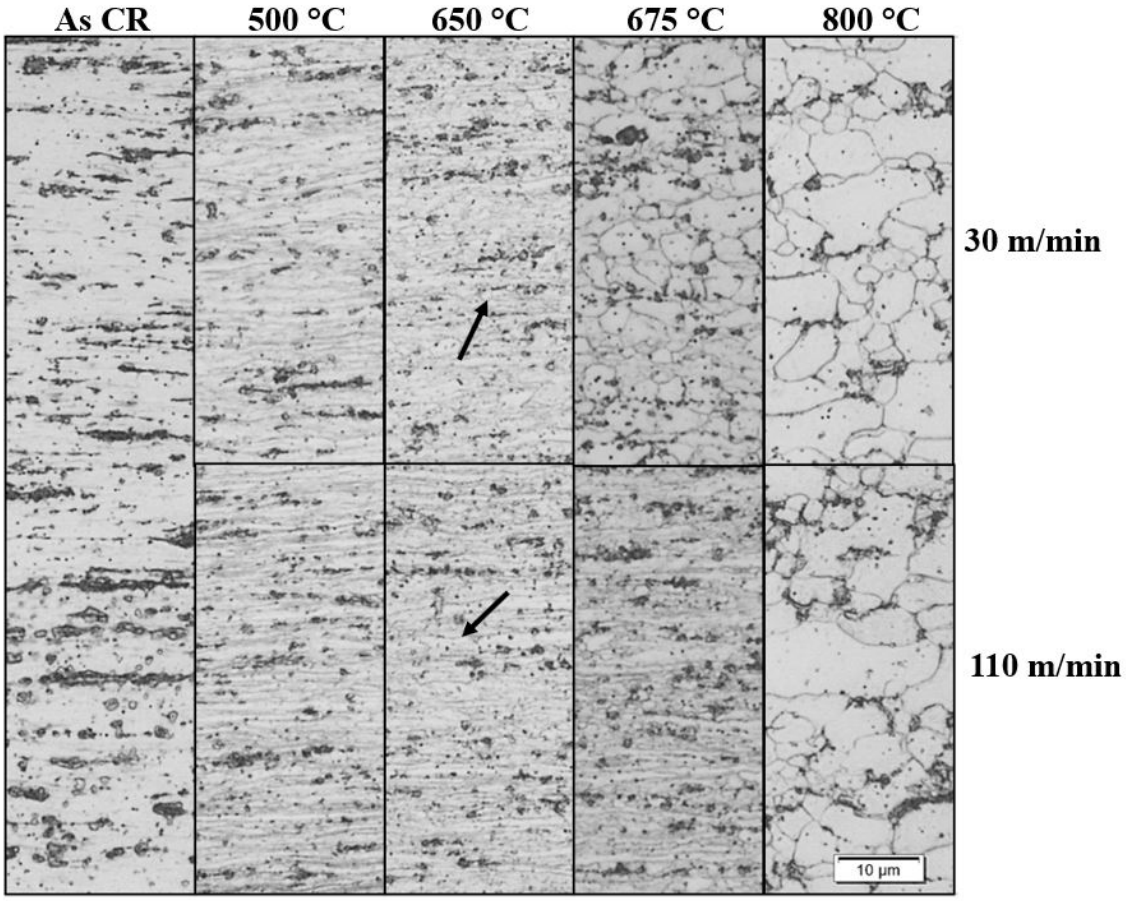

Figure 46: Annealing simulations: optical micrographs showing the evolution of microstructures with annealing temperature in Nb-Ti steel at simulated line-speeds of 30 and 110 m/min respectively; the arrows indicate newly formed grains at 650 °C.

As may be seen for both V-N and Nb-Ti steels, both the microstructures and the subsequent hardness values are only sensitive to the simulated line-speed when the annealing temperature exceeds 650 °C. Otherwise, between 550 and 650 °C, i.e. within the recovery window, both the microstructures and the resulting hardness values were found to be insensitive to the simulated line-speeds, Figures 44, 45 and 46. This is advantageous because it minimises the scatter in the mechanical properties during the production of these steels.

4.4 EBSD analysis

Figure 47a, b, d and e shows EBSD grain structure plots in the as-cold-rolled condition, annealed at 675 °C and at a simulated line-speed of 110 m/min for steel 1 (Nb-Ti) and steel 2 (V-N). Additionally in Figure 47c, f, and g similar plots are shown for steel 1 (Nb-Ti) annealed at 650, 675 and 800 °C at a simulated line-speed of 30 m/min. Figure 48 shows the associated fraction of LAGB segments.

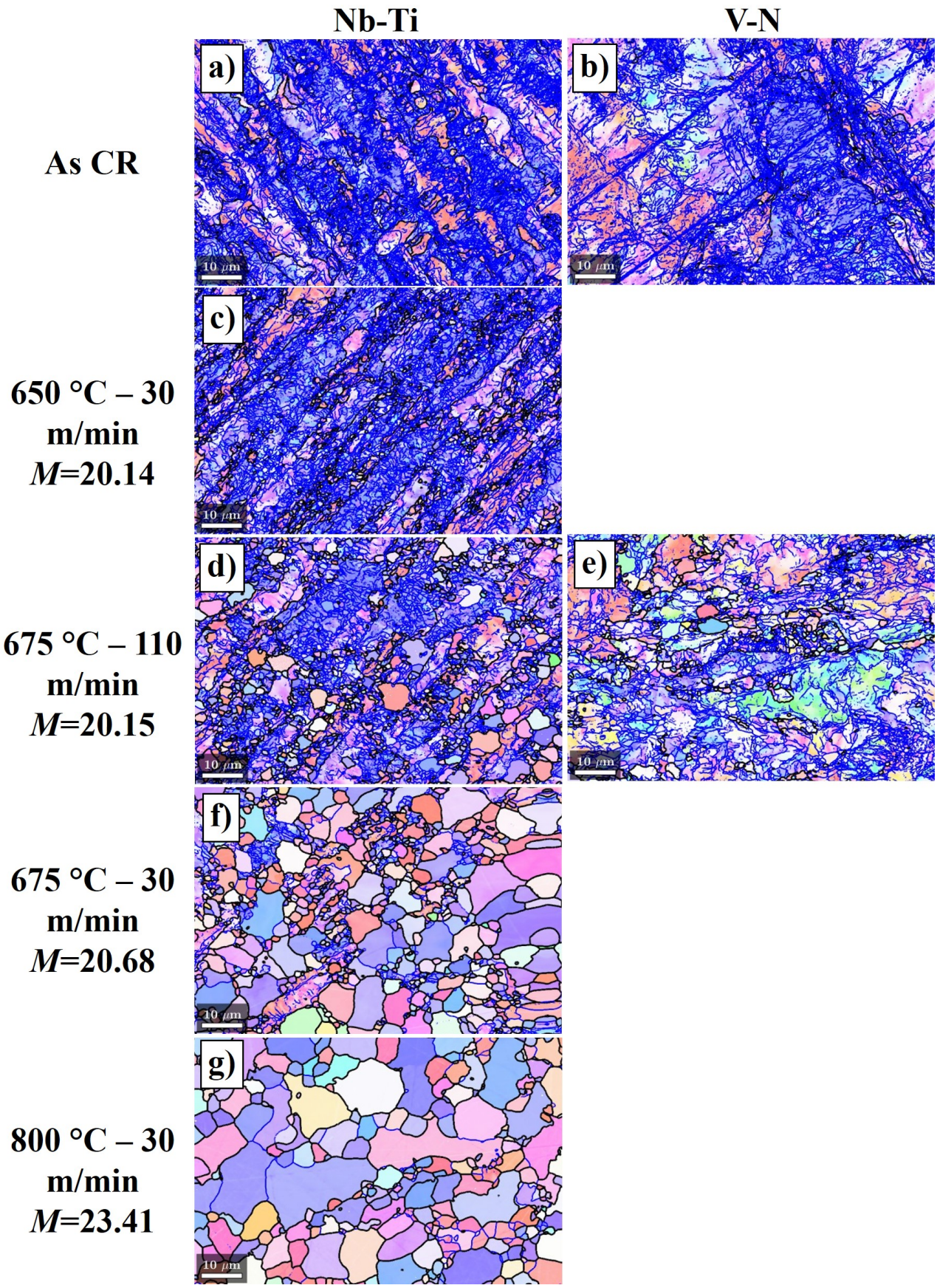

Figure 47: EBSD: plots showing HAGB segments with black lines (misorientations >15°) and LAGB segments (subgrains) as blue lines (misorientations >2° and <15°).

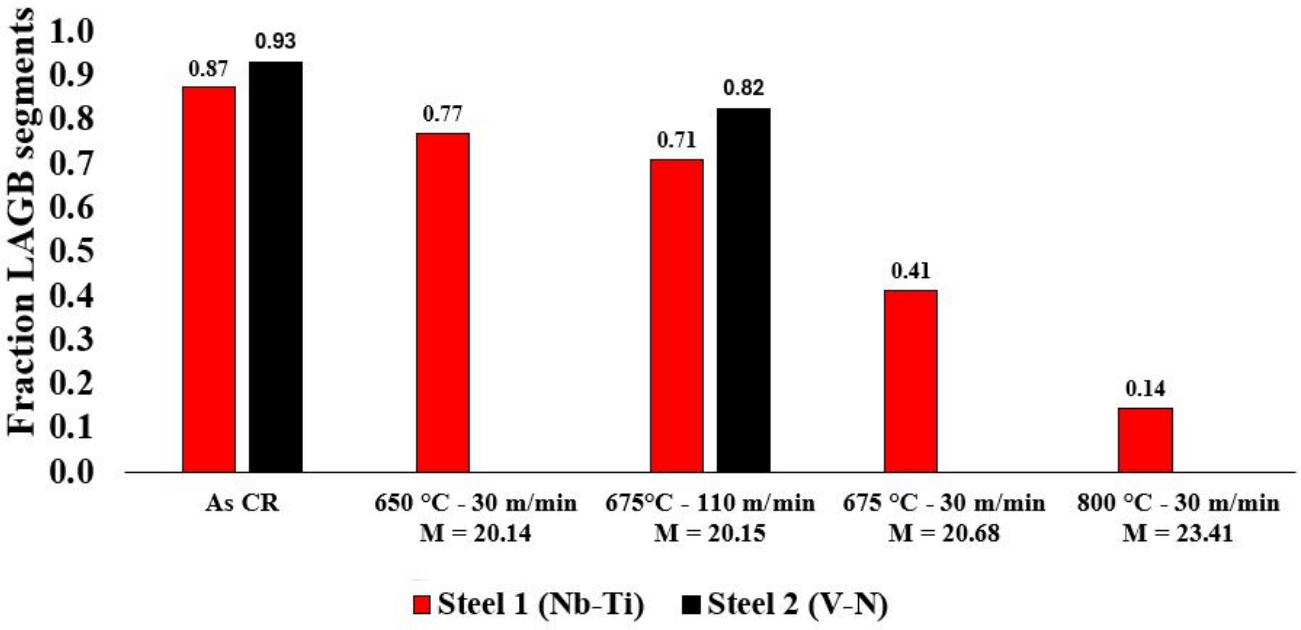

Figure 48: EBSD: fraction LAGB segments

The grain/subgrain size of V-N is larger compared to Nb-Ti and this is attributed to the effective grain/-subgrain boundary pinning by Nb precipitates in the latter. Therefore, the Nb-Ti is more recrystallised at 675 °C, Figure 47d, compared to V-N, Figure 47e, under similar conditions. This is confirmed in Figure 48 with the fraction LAGB segemnts of Nb-Ti being 0.11 lower than that of V-N at $M = 20.15$.

Figure 49 shows the grain orientation spread (GOS) maps of the Nb-Ti and V-N steels respectively, in the as-cold-rolled condition and annealed at 675 °C and a simulated line-speed of 110 m/min. The Nb-Ti steel exhibited more misorientated grains, Figure 49a, compared to the V-N steel, Figure 49b, in the as-cold-rolled condition. However, in the partially annealed condition at a temperature of 675 °C and simulated line-speed of 110 m/min the misorientation in the Nb-Ti steel, Figure 49c, has mostly diminished but the V-N, Figure 49d, is comparable to its as-cold-rolled condition.

The EBSD pole figure plots shown in Figure 50 further support the observations in Figure 49. In the as-cold-rolled condition, there is a significant difference between Nb-Ti, Figure 50a, and V-N, Figure 50b, with Nb-Ti showcasing a clear preferred orienation compared to V-N. In the partially annealed condition at a temperature of 675 °C and simulated line-speed of 110 m/min the Nb-Ti, Figure 50c, mostly kept the same texture, although slightly evening the distribution. With the V-N steel in the simulated annealed condition, Figure 50d, the distribution has almost completely disappeared. It is possible that more recovery occurred in the V-N steel compared to the Nb-Ti steel due to Nb(C,N) precipitates being more effective in delaying recovery by boundary pinning. Similar results on isotropy were reported by Banks *et al.* on as-hot-rolled V-N steels with equivalent chemistry [60].

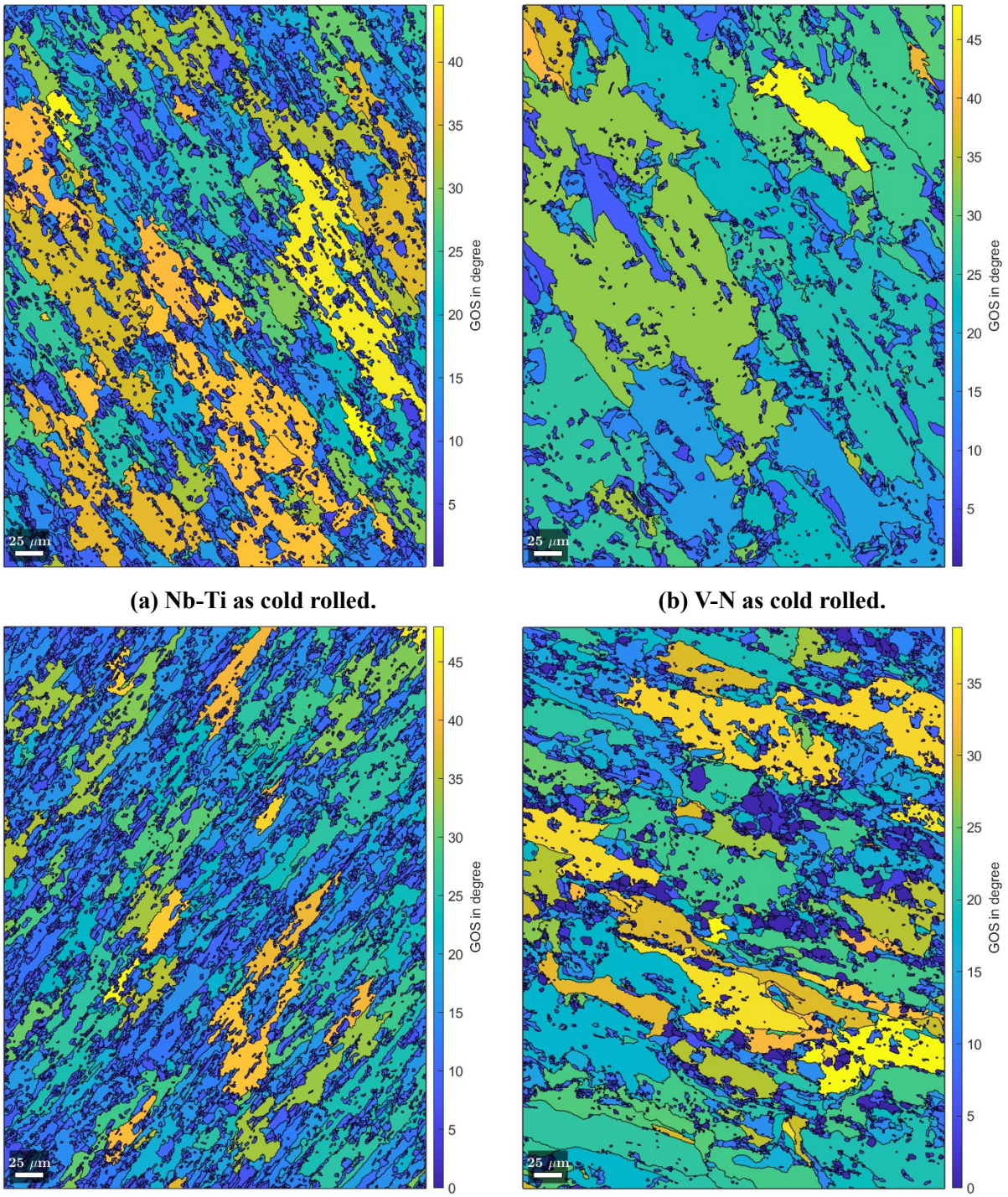

(a) Nb-Ti as cold rolled.

(b) V-N as cold rolled.

(c) Nb-Ti 675 °C - 110 m/min.

(d) V-N 675 °C - 110 m/min.

Figure 49: EBSD: GOS maps of Nb-Ti and V-N steel in the as cold rolled (a), (b) and annealed at 675 °at simulated line-speed of 110 m/min (c), (d).

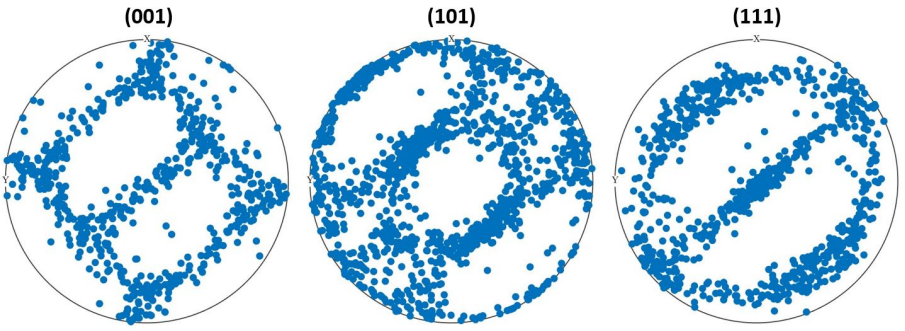

(a) Nb-Ti as cold rolled.

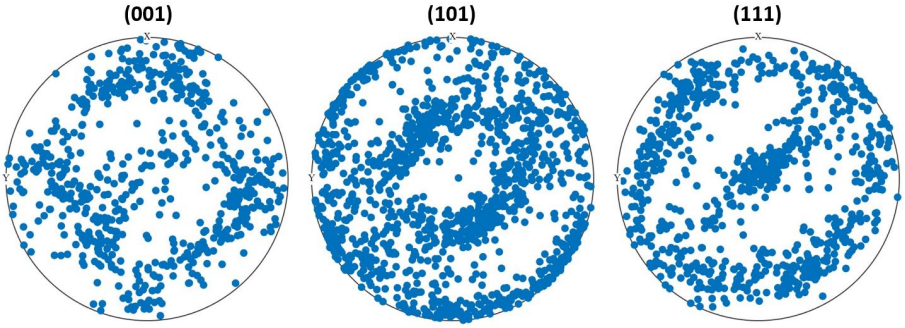

(b) V-N as cold rolled.

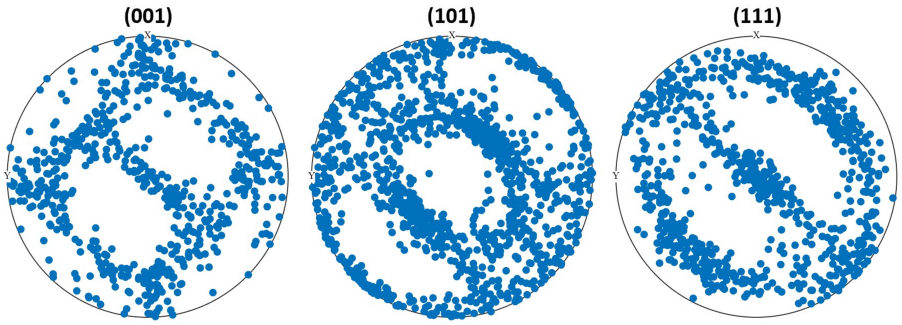

(c) Nb-Ti 675 °C - 110 m/min.

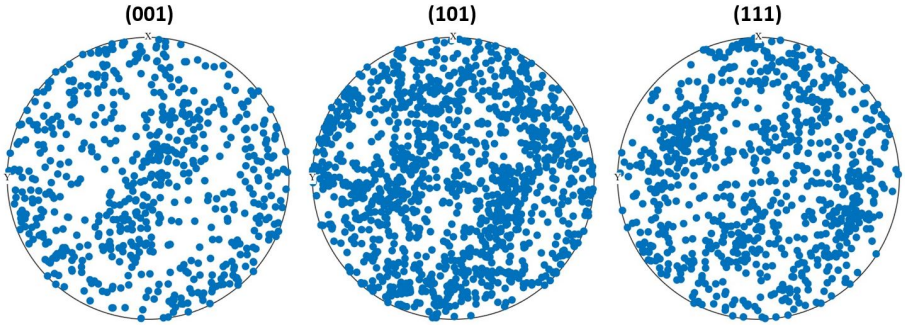

(d) V-N 675 °C - 110 m/min.

Figure 50: EBSD: pole orientation plots of Nb-Ti and V-N steel in the as cold rolled (a), (b) and annealed at 675 °at simulated line-speed of 110 m/min (c), (d).

4.5 TEM

Figure 51 shows ADF-STEM images of the Nb-Ti steel in the (a) as-cold-rolled, (b) 650 ° C at simulated line-speed 30 m/min and fully annealed at 800 °C at simulated line-speed of 30 m/min. The as-cold-rolled structure, Figure 51(a), shows shear bands and dislocation boundaries. Figure 51(b) consists of clearly defined subgrains and evidence of subgrain coalescence, which indicates the end of recovery [13]. The fully annealed structure (Figure 51(c)) shows grain boundaries with some free dislocations within the grains.

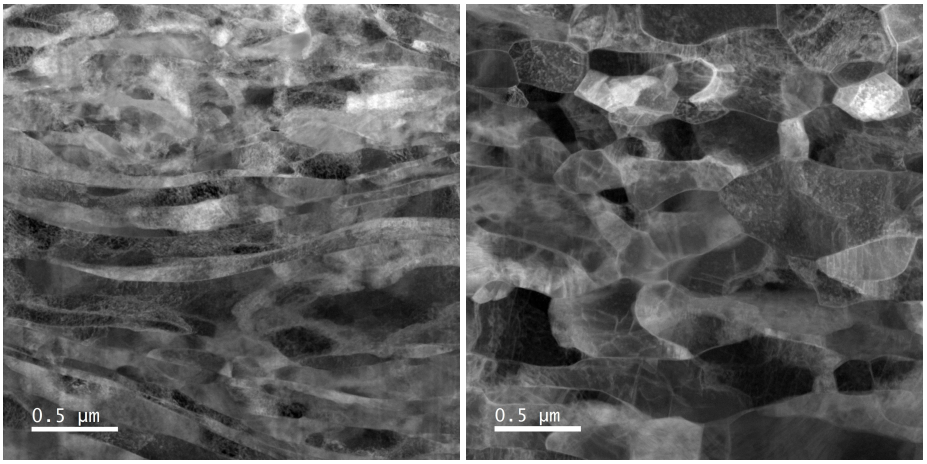

(a) As-cold-rolled. **(b) 650 °C and 30 m/min.**

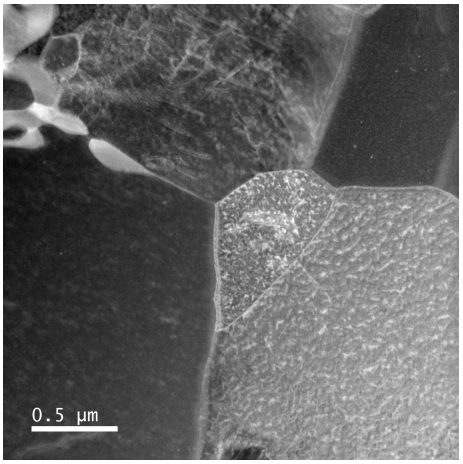

(c) 800 °C and 30 m/min.

Figure 51: ADF-STEM micrographs of 85 % cold-worked Nb-Ti steel (steel 1).

Figure 52 shows the precipitates found in the Nb-Ti and V-N samples in the fully annealed condition (800 °C at simulated line-speed 30 m/min). Large rectangular Ti(C,N) measuring 160 to 360 nm in length and fine ($\sim$ 76 nm diameter) spherical Nb(C,N) were observed, Figure 52a. Figure 52b shows fine V-N precipitates which were found to be less than 50 nm and were difficult to observe. Figure 52b also shows coarse AlN particles in the range of 260 to 370 nm.

Using energy-filtered transmission electron microscopy (EFTEM), the distributions of elements V, N and Ti can be seen in Figure 53. In the V-N steel, the V and N tended to agglomerate around the AlN

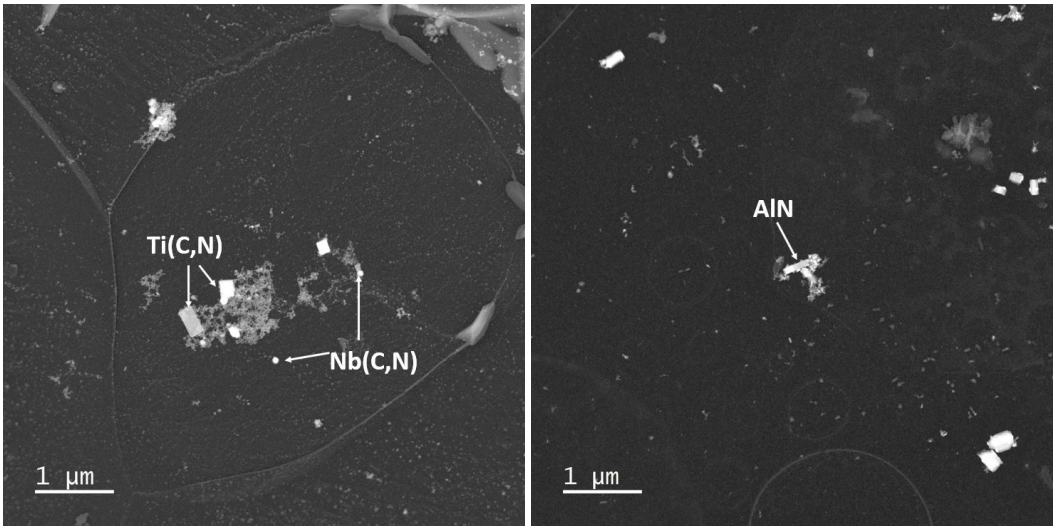

(a) Nb-Ti (steel 1). (b) V-N (steel 2).

Figure 52: High-resolution transmission electron microscopy (HRTEM) micrographs after annealing at 800 °C at a simulated line-speed of 30 m/min.

precipitates with a few small isolated V concentrations which are <50 nm, Figure 53b.

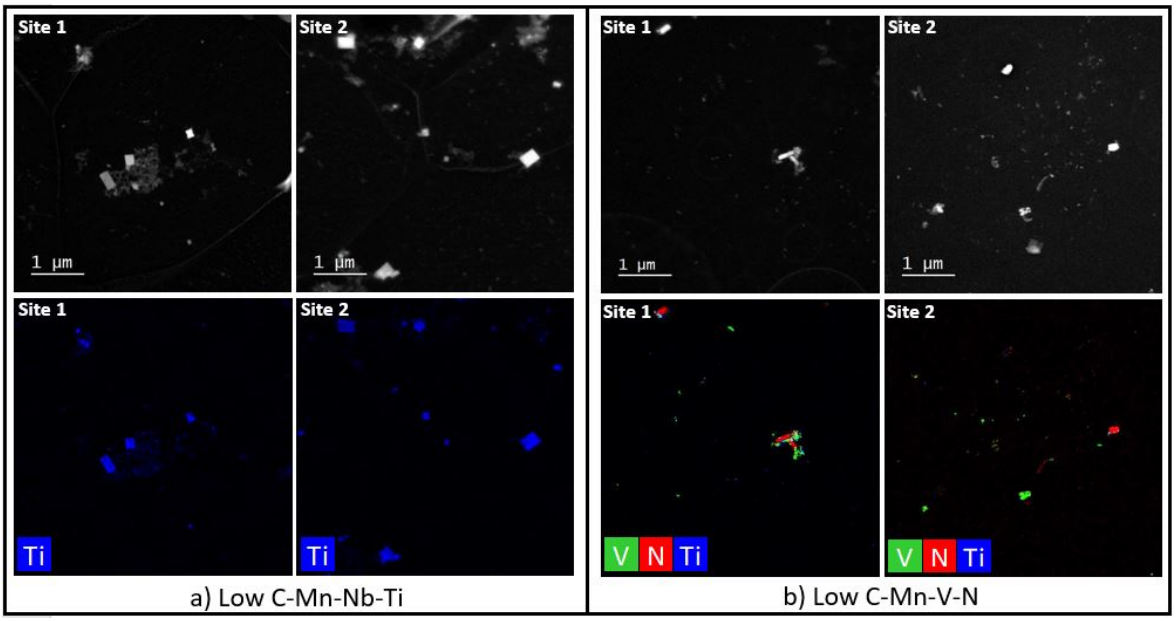

Figure 53: EFTEM images showing elemental distributions of elements V, N and Ti.

4.6 XRD dislocation density calculations

Figure 54 shows calculated dislocation densities using Equation 21 at different M values (data in Table C.1). Higher as-cold-rolled hardness in the Nb-Ti steel corresponds with a higher dislocation density of 1.05^{15} m^{-2} compared to 8.35^{14} m^{-2} for the V-N, which agrees with the earlier observation regarding the Nb-Ti steel having increased dislocation density due to superior boundary pinning. With increasing M, similar linear dislocation density trends are observed in both Nb-Ti and V-N.

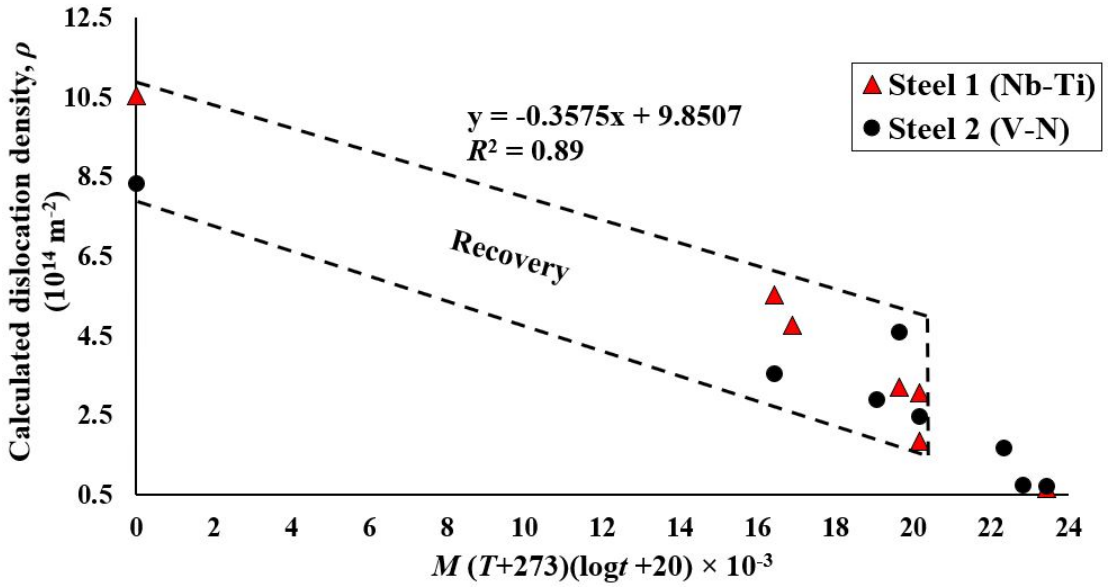

Figure 54: Calculated dislocation density with linear trend vs. *M* for Nb-Ti and V-N steels, showing recovery region.

Figure 55 shows the correlation between the hardness and the square root of the dislocation density as suggested by Dutta *et. al.* [31]. The R^2 value is 0.556, with the poor correlation being attributed to the XRD technique mainly measuring SSDs [41].

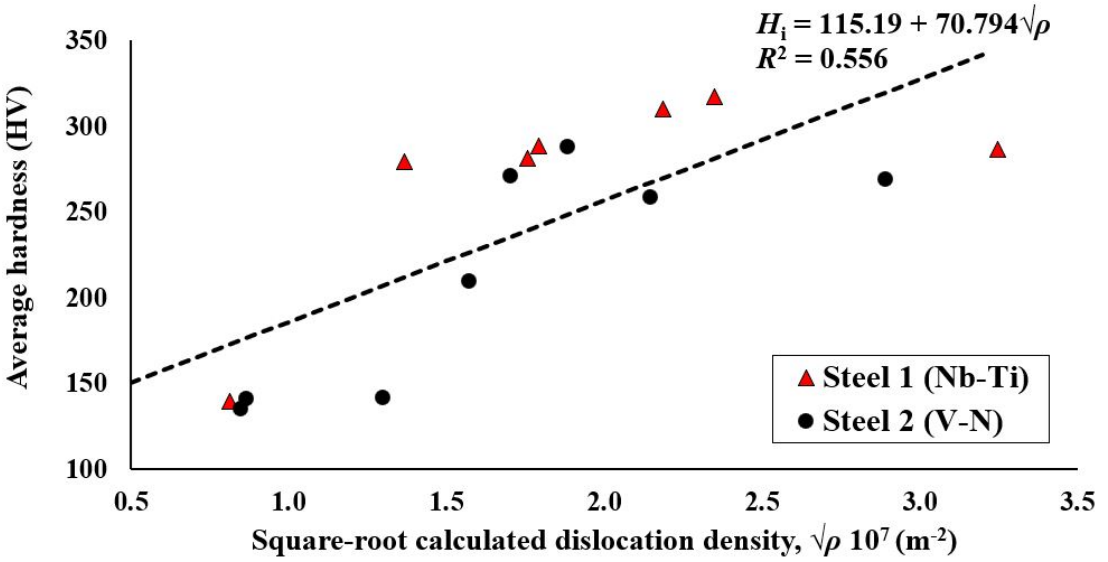

Figure 55: Average hardness vs. calculated dislocation density for Nb-Ti and V-N steels.

4.7 Industrial trial at the continuous hot dip galvanising plant

Table VII provides a summary of the processing parameters and mechanical properties in the rolling direction of industrially galvanised trial coils. Figure 56 illustrates the stress-strain curves of the industrially back-annealed coils using these process parameters. The choice of a T_{max} of 640 °C was based on

the laboratory results in Figure 40 because 650 °C provided the optimal strength before recrystallisation starts. The line speed was maintained at a constant 101 m/min.

The average T_{max} ranged between 630 and 640 °C in the radiant tube furnace (RTF), with T_{max} within the range of 625 and 645 °C. Notably, only coil 2, finished at 840 °C and coiled at 575 °C, exhibited an A_{80} above 10%, while the elongation in the other coils ranged between 2.9 and 4%. Although coil 2 had a significantly lower 0.2% yield strength at 767 MPa compared to the other coils, which exceeded 800 MPa, its ultimate tensile strength (UTS) of 803 MPa still fell within the 750 to 910 MPa specification, as shown in Figure 56.

Table VII: Processing parameters and mechanical properties in the rolling direction of industrially galvanised trial coils.

Coil	Cold work [%]	Finish T [°C]	Coiling T [°C]	HDG T_{max} [°C]	0.2 yield strength [MPa]	UTS [MPa]	Elongation A_{80} [%]	Hardness [$HV_{0.5kg}$]
1	81	880	625	645	869	894	2.9	296
2	81	840	575	645	767	803	10.8	264
3	78	880	625	633	855	876	4.0	298
4	78	840	575	625	817	846	3.4	292

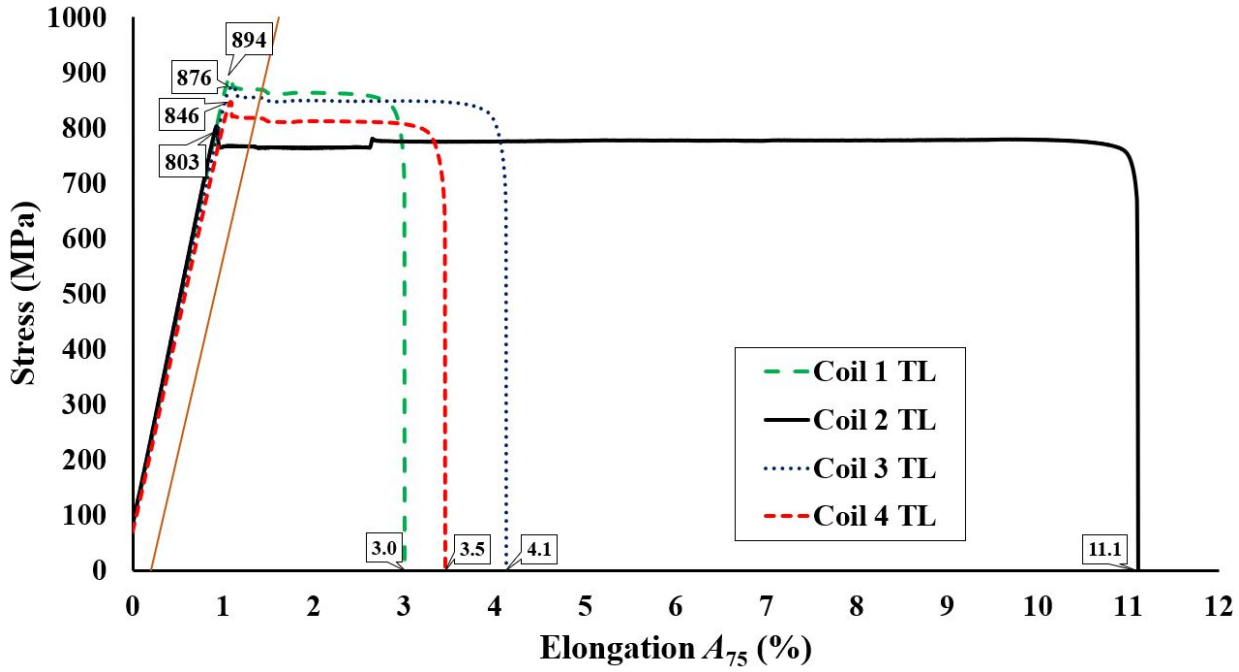

Figure 56: Stress strain curves of industrially back-annealed coil samples.

Figure 57 reveals disparities between laboratory and industrial hardness results for a given T_{max}, except for coil 2. These differences can be attributed to variations in the hot rolling conditions between the laboratory and industrial settings.

The precipitation of carbonitrides significantly influenced the stored energy during cold rolling [8].

Coil 2, with a coiling temperature of 575 °C, as indicated in Figure 6, led to the most effective grain refinement. This possibly resulted in a higher dislocation density compared to the higher coiling temperature of 625 °C. The higher volume fraction of precipitates available for pinning delayed recovery and created a stronger driving force for recrystallisation.

Figure 58 displays the microstructures obtained after industrial processing, indicating no partial recrystallisation except for coil 2, which exhibited a small fraction of newly recrystallised grains. The microstructures of coil 2 were similar to those after laboratory annealing simulations at 650 °C, albeit with a larger subgrain size, Figure 45. The lower hot rolling finish temperatures in coils 2 and 4 produced a finer subgrain structure due to optimal precipitation after hot rolling, where almost all V was utilised for precipitation. Coil 4 with similar hot rolling conditions as coil 2 experienced limited recovery due to the low T_{max} of 625 °C, resulting in elongation of only 3.4 %.

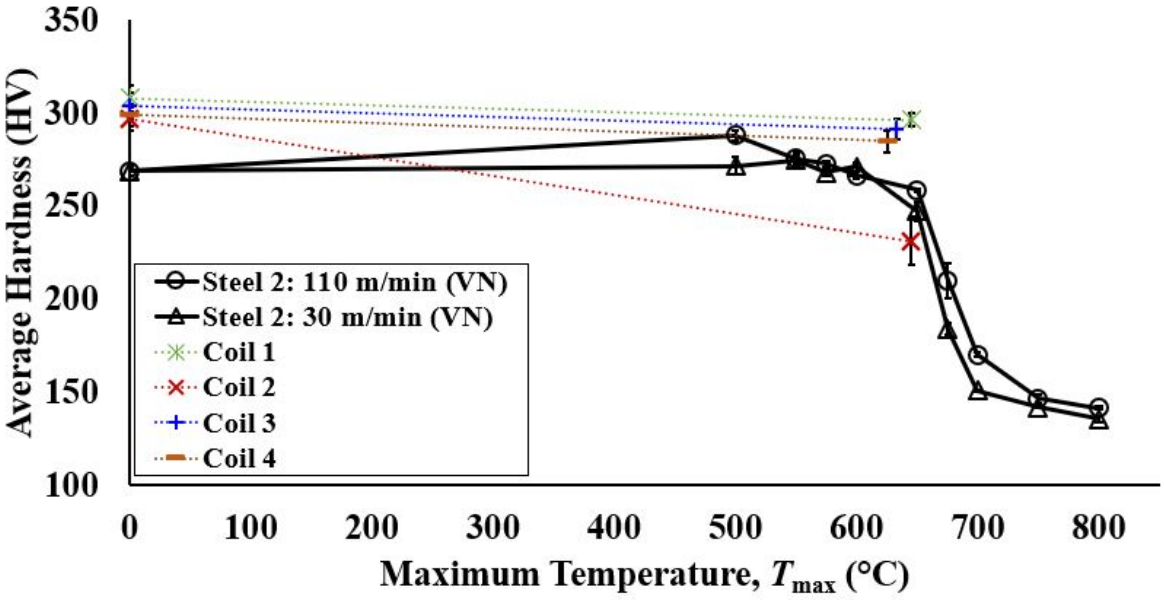

Figure 57: Hardness vs. T_{max} plots for the V-N steel after laboratory annealed (simulated line-speeds 30 and 110 m/min) and industrial back-annealing (coils 1 to 4).

In summary, a significant elongation of 10.8% with high strength was achieved industrially in coil 2. The choice of hot rolling temperatures, both finish, and coiling, had an influence on the subsequent back-annealing behaviour. Despite the relatively low elongations, ranging from 2.9% to 4.0% in coils 1, 3, and 4, the stress-relieved material exhibited improved formability compared to the as-cold-rolled condition. These findings emphasise the necessity of experimentation on the specific to determine the optimal annealing temperature to ensure stable production.

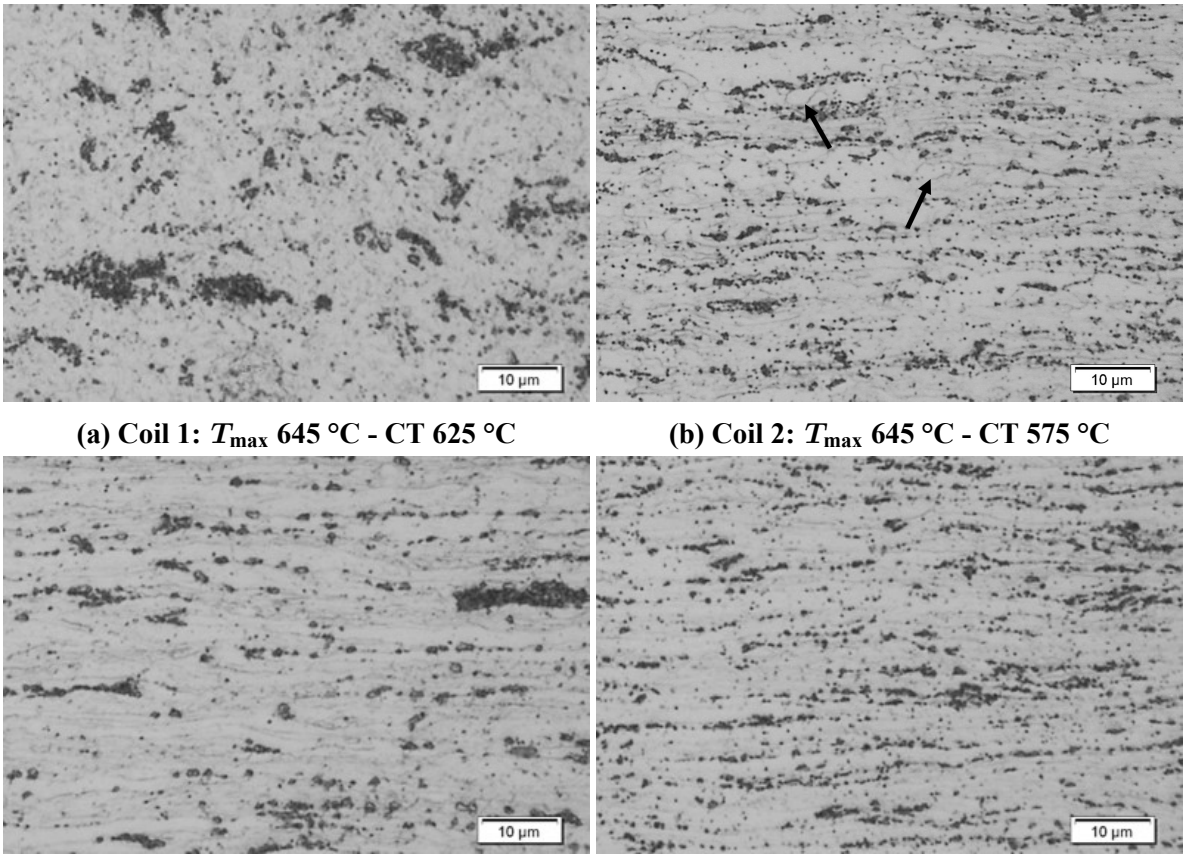

(a) Coil 1: T_{max} 645 °C - CT 625 °C

(b) Coil 2: T_{max} 645 °C - CT 575 °C

(c) Coil 3: T_{max} 633 °C - CT 625 °C

(d) Coil 4: T_{max} 625 °C - CT 575 °C

Figure 58: Microstructures of industrially back-annealed coils. Arrows indicate newly formed grains in coil 2.

Chapter 5: Discussion

5.1 Influence of amount of deformation on back-annealing process

From Figure 39, it can be observed that the amount of deformation, ranging between 55% and 85%, does not significantly affect the recrystallisation start, M_{rs}, for a given time and temperature. This behaviour is expected because the SIBM, as mechanism for restoration, is dominant at lower reductions, specifically less than 40% and the mechanism transitions to the dislocation-free pre-existing embryos at higher reductions. This phenomenon was initially postulated by Beck and Sperry based on their work on pure aluminium [27].

In another study conducted by Ray *et al.* [3] on 0.02% Nb steels, cold reductions ranging from 40% to 70% were examined. The study revealed a transition between 40% and 50% reductions, where the recrystallisation start temperature (M_{rs}) increased substantially at 40% reduction. However, there was no significant difference observed between 50% and 70% reductions, as shown in Figure 34. This is advantageous because, during real-life plant cold rolling and back-annealing, the amount of deformation could vary from one run to the next without necessarily affecting the properties for cold reductions greater than 55%. This would result in less scatter in the properties of the final product.

While microstructures and initial hardness might influence peak hardness (Figure 39), the recrystallisation start (M_{rs}) did not appear to be significantly affected by the prior conditions of the steel, at least when comparing 55% and 85% reductions in V-N and Nb-Ti steels. Similar observations were made in the 66 and 83% reduction plain C steel samples. This was attributed to the observation made by Ray et al. [3] that beyond 40% deformation, the recrystallisation start is insensitive to the amount of deformation. In other words, the driving force is high enough to overcome the varying levels of the Zener pinning of the crystallisation front. This only occurs until the driving force decline to such a level whereby the Zener pinning becomes greater than the former leading to the retardation of the recrystallisation process and depending on the coiling temperature, complete recrystallisation arrest. Industrially, this implies that thinner gauge material can be produced with flexibility in the initial thickness of the hot band. Similarly, cold mills with limited amount of reductions, mill load capacity and width can still be used to achieve the mechanical properties as long as the cold reductions are within 50 and 85%.

Although this study did not specifically investigate the effects of alloy contents, such as variations in the amounts of V, Nb, Ti, and C, previous research by Ray *et al.* [3] comparing 0.031% and 0.060% Nb on 70% cold work showed only a minor shift in M_{rs} from 19.4 to 19.6. Similarly, in the case of 70% cold worked V-N steels (Figure 35), the increase in M_{rs} was not significant, rising from 19.8 to approximately 19.9 when the V content increased from 0.03% to 0.10%, (Equation 7). For a V content of 0.05% in the present study, the resulting M_{rs} was 20.1, falling within the range of values reported by Ray et al. However, this was not observed at lower reductions of 40% indicating at higher deformations, as was in this study, the driving force was more than the Zener pinning force, Equation 7. Additionally, work conducted by Ferry *et al.* [61] found that for a 70% cold worked 0.02% and 0.05% C – 0.3% Mn

steel, the onset of recrystallisation only slightly increased from 660 to 670 °C with the lower C content of 0.02%. A similar observation was made in an internal plant investigation on HDG annealing [62], where 78% cold worked 0.023%C-0.33Mn% and 0.07C%-0.45Mn% steels resulted in an increase in the recrystallisation start temperature from 575 to 600 °C with corresponding M_{rs} values of 18 and 18.5, respectively, which is pretty close. Implying that there are still subtle differences at low C contents under plant conditions. However, by and large, these subtle difference may not have substantial impact on the mechanical properties as long as the C content is kept below 0.08%.

5.2 Recovery kinetics and subsequent properties: Nb-Ti versus V-N

The recrystallisation kinetics of the Nb-Ti and V-N steels exhibited similarities regarding initial hardening and fast initial recrystallisation rate. The delayed onset of recrystallisation compared to the plain C steel establishes that both Nb-Ti and V-N steels are viable options for back-annealing, as evidenced by the increase in M_{rs}, Figure 41. Figure 40 shows that both Nb-Ti and V-N steels exhibit similar trends up to M value of 20.7. However, beyond this point, an arrest in hardness drop was observed in Nb-Ti due to the dislocation pinning by NbC particles. This happened due to the dwindling of the driving force for recrystallisation as the recrystallised fraction increased i.e. when the driving force was less than the pinning force, Equation 7. However, this arrest is outside the back-annealing window of interest as the strength is way below the desired limits of between 750 and 910 MPa. This is also advantageous because it would be challenging to control the mechanical properties if precipitation occurred within the back-annealing window.

As may be seen from Figure 40, the V-N steel is fully annealed at a lower M of 21.2 compared to 23.0 for the Nb-Ti steel. To ensure fully annealed Nb-Ti steel, it has to be annealed at higher temperatures and/or at longer times. The Nb-Ti steel displayed a large deviation between the two heating rates, i.e. 30 and 110 m/min at 675 °C, Figure 44. This is confirmed in the microstructures in Figure 46 and subgrain plots in Figure 47. It was observed in a study by Bellavoine [59] that faster heating rates could lead to less time available for NbC precipitation which is observed when comparing Figure 47c and d. With M values, 20.14 and 20.15, the faster heating rate of 110 m/min resulted in more recrystallisation as seen in the signifncant decrease of subgrain segments, Table **??**. This suggests that Nb-Ti has inherent instability with regards to recrystallisation start, M_{rs}, and further softening during later stages of the annealing process. Here, the V-N steel exhibited an advantage over the Nb-Ti steel. This together with ease of hot rolling i.e. reduced re-heat temperature and lower rolling forces makes V-N steels attractive compared to Nb-Ti.

5.3 Limitations of estimating dislocation density during back-annealing process

Figure 54 shows estimations of the dislocation density using XRD data, which showed that in the as-cold-rolled the smaller subgrain size of Nb-Ti corresponded to an increased dislocation density which makes sense as the crystallite size is smaller (Figure 30(b)). This resulted in increased stored energy

for recrystallisation prior to the arrest by the NbC particles. Interestingly, these trends do not align with the hardening and subtle softening observed in the hardness vs. M plots, emphasising that recovery did indeed occur.

This discrepancy opens up the possibility of tracking recovery progression more effectively using XRD since changes at low temperatures can be observed. Despite the many limitations of using XRD to determine dislocation [35][41], this technique can still be used to track the recovery and recrystallisation progress. As can be seen in Figure 54, there is a linear trend with an R^2 value of 0.89 when considereing both V-N and Nb-Ti. The recovery region shown in Figure 54 is in contrast with the hardness vs. M in Figure 40 where there was little change in hardness in the recovery region.

The observation made by Gallet [41] that mainly SSDs are visible with XRD makes it an ideal technique to quantify recovery progression due to annihilation of these SSDs during the recovery process i.e. polygonization [9][10].

5.4 Industrial application of the optimised back-annealing conditions

The industrial trial conducted on the V-N steel validated the successful application of back-annealing to obtain high-strength steel strips during HDG. It emphasises the selection of appropriate hot rolling parameters to effectively utilise V(C,N) precipitates to retard the onset of recrystallisation.

In order to meet the S700GD specification, a low finish temperature of 840 °C and a low coiling temperature of 575 °C was employed. This strategy increased the availability of V(C,N) for subgrain pinning, extending the recovery process window and allowing more time for recovery rather than recrystallisation. Consequently, this approach led to the optimisation of both the strength and elongation i.e. an elongation of 10.8% and a yield strength of 767 MPa.

The significance of the mechanical properties of the other coils should not be overlooked. Despite not meeting the S700GD specification in terms of elongation, there was still a degree of recovery that took place, leading to elongations in the range of 2.9 to 4.0%. The recovery rendered these coils superior mechanical properties to the typical un-annealed galvanised material. The material effectively underwent a stress relief treatment, resulting in enhanced spring back and shape characteristics, indicating potential value in specific applications.

Chapter 6: Conclusions

The back-annealing of hot dip galvanised strip steel microalloyed with vanadium was investigated in this work using the Nb-Ti and plain low C steels as benchmarks and the following conclusions can be made:

- V-N steel exhibited superior back-annealing and full annealing characteristics compared to Nb-Ti. The interference of NbC precipitation during annealing had a significant impact on the resulting mechanical properties and microstructure with Nb-Ti steel, making the process more challenging to control.
- Both V-N and Nb-Ti steels extend the recovery annealing window by 50 °C when compared to low C steels. The recrystallisation start temperature was increased resulting in a M_{rs} value of 20.1 for both micro-alloyed steels compared to 18 in the plain low C grade.
- The EN 10346 S700GD specification was achieved industrially by processing a V-N steel with a 0.2% yield strength of 767 MPa, UTS of 803 MPa and A80 of 10.8% under the following conditions: low finishing temperature of 840 °C and coiling temperature of 575 °C followed by back-annealing 81% cold worked strip to a maximum temperature of 645 °C.
- Calculated dislocation densities using XRD and Rietveld refinement in both V-N and Nb-Ti steels exhibited a linear decrease with increasing M, with an R^2 value of 0.89. This method proved useful for quantifying recovery progression, as it allowed the observation of subtle changes that occur, unlike using hardness alone.
- Large rectangular Ti(C,N) precipitates, measuring 160 to 360 nm, and very small spherical Nb(C,N) precipitates, measuring an average of 76 nm, were observed in the fully annealed Nb-Ti steel. Large rectangular AlN precipitates, measuring 260 to 370 nm, were observed in the fully recrystallised V-N sample. The EFTEM revealed fine V(C,N) precipitates, less than 50 nm in size, in the V-N steel.

References

[1] P. Suwanpinij, "The synchrotron radiation for steel research. advances in materials science and engineering," *Advances in Materials Science and Engineering*, vol. 2016, 2016.

[2] B. Beetz, J. Guth, C. Dieu, and H. Campos, "Reducing the environmental impact of pv mounting structures," *pv-magazine*, Feb. 10, 2022. [Online]. Available: `https://www.pv-magazine.com/webinars/reducing-the-environmental-impact-of-pv-mounting-structures/`.

[3] R. Ray, B. Hutchinson, and C. Ghosh, "'back-annealing' of cold rolled steels through recovery and/or partial recrystallisation," *International materials reviews*, vol. 56, no. 2, pp. 73–97, 2011.

[4] R. Lagneborg *et al.*, "The role of vanadium in microalloyed steels," Sweden, 2014.

[5] S. Zajac, R. Lagneborg, and T. Siwecki, "The role of nitrogen in microalloyed steels," *Materials Science and Engineering*, vol. 2, no. 6, pp. 285–302, 1967.

[6] S. Zajac *et al.*, "Strengthening mechanisms in vanadium microalloyed steels intended for long products," *ISIJ International*, vol. 38, pp. 1130–1139, 1998.

[7] H. Bhadeshia and R. Honeycombe, *Steels - Microstructure and Properties 4th Edition*. Asia: Elsevier, 2017, p. 257.

[8] J. Humphreys, G. Rohrer, and A. Rollett, *Recrystallization and Related Annealing Phenomena*. Oxford: Elsevier, 2017, pp. 1–79, 199–359.

[9] R. Abbaschian, L. Abbaschian, and R. E. Reed-Hill, *Physical metallurgy principles*. Stamford: Cengage Learning, 2010, pp. 216–232.

[10] A. Rollett *et al.*, *Recrystallization and Related Annealing Phenomena*. Stamford: Cengage Learning, 2010, pp. 169–213.

[11] P. Lam, "Intergranular corrosion of extruded AlMgSi (Cu, Zn) alloys," M.S. thesis, NTNU, 2016.

[12] H. Gleiter and E. Hornbogen, "Precipitation hardening by coherent particles, review paper," *Microalloying*, no. 95, pp. 321–340, 1995.

[13] A. Samet-Meziou *et al.*, "Tem study of recovery and recrystallization mechanisms after 40 % cold rolling in an if-ti steel," *Scripta Materialia*, vol. 53, pp. 1001–1006, 2005.

[14] A. Martinez-de-Guerenu *et al.*, "Recovery during annealing in a cold rolled low carbon steel.part i: Kinetics and microstructural characterization," *Acta Materialia*, vol. 52, pp. 3657–3664, 2004.

[15] C. Siyasiya, "Effect of sulphur content on the recrystallisation behaviour of cold worked low carbon aluminium-killed strip steels," 2007.

[16] W. Hutchinson, "Development of textures in recrystallization," *Metal Science*, vol. 8, no. 1, pp. 185–196, 1974.

[17] J. Humphreys, G. Rohrer, and A.Rollett, *Recrystallization and Related Annealing Phenomena*. Oxford: Elsevier, 2017, pp. 251–359.

[18] R. Doherty *et al.*, "Current issues in recrystallization: A review," *Materials Science and Engineering*, vol. 238, no. 2, pp. 219–274, 1997.

[19] W. Leslie, "Iron and its dilute substitutional solid solutions," *The American Society for Metals*, vol. 3, pp. 5–26, 1971.

[20] U. Köster, "Recrystallization involving a second phase," *Metal Science*, vol. 8(1), pp. 151–160, 1974.

[21] J. Burke and D. Turnbull, "Recrystallization and grain growth," *Progress in Metal Physics*, vol. 3, pp. 220–244, 1952.

[22] R. Cahn, "A new theory of recrystallization nuclei," *Proceedings of the Physical Society. Section A*, vol. 63, pp. 323–336, 1950.

[23] E. Holm, M. Miodownik, and A. Rollett, "On abnormal subgrain growth and the origin of recrystallization nuclei," *Acta Materialia*, vol. 51, pp. 2701–2716, 2003.

[24] H. Vatne *et al.*, "Modelling of recrystallization after hot deformation of aluminium," *Acta Materialia*, vol. 11(11), pp. 4463–4473, 1996.

[25] X. Duan and T. Sheppard, "Simulation of substructural strengthening in hot flat rolling," *Materials Processing Technology*, vol. 125–126, pp. 179–187, 2002.

[26] D. Hughes *et al.*, "Scaling of microstructural parameters: Misorientations of deformation induced boundaries," *Acta Materialia*, vol. 45, pp. 105–112, 1997.

[27] P. Beck and P. Sperry, "Strain induced grain boundary migration in high purity aluminum," *Journal of Applied Physics*, vol. 21, pp. 150–152, 1950.

[28] J. Baily and P. Hirsch, "The recrystallization process in some polycrystalline metals," *Proceedings of the royal society*, vol. 267, pp. 11–30, 1962.

[29] P. Rios *et al.*, "Nucleation and growth during recrystallization," *Materials Research*, vol. 8, pp. 225–238, 2005.

[30] M. Avrami, "Kinetics of phase change. ii transformation-time relations for random distribution of nuclei," *J. Chem. Phys*, vol. 8, pp. 212–224, 1939.

[31] B. Dutta, E. Valdes, and C. M. Sellars, "Mechanism and kinetics of strain induced precipitation of Nb(C, N) in austenite," *Acta metall mater*, vol. 40, no. 4, pp. 653–662, 1992.

[32] Y. Meng, X. Ju, and X. Yang, "The measurement of the dislocation density using tem," *Materials Characterization*, vol. 175, 2021.

[33] S. Monteiro *et al.*, "Novel methods for dislocation density estimation in highly compacted tangles," *Journal of Materials Research and Technology*, vol. 9, pp. 2072–2078, 2020.

[34] T. Ungár, "Dislocation densities, arrangements and character from x-ray diffraction experiments," *Materials Science and Engineering*, vol. A309–310, pp. 14–22, 2001.

[35] J. Pesicka *et al.*, "The evolution of dislocation density during heat treatment and creep of tempered martensite ferritic steels," *Acta Materialla*, vol. 51, pp. 4847–4862, 2003.

[36] W. Callister and D. Rethwisch, *Material science and engineering*. Asia: John Wiley and Sons, 2011, pp. 728–730.

[37] M. Sablik, "Modeling the effect of grain size and dislocation density on hysteretic magnetic properties in steels," *Journal of Applied Physics*, vol. 89, pp. 5610–5613, 2001.

[38] G. K. Williamson and R. E. Smallman, "Iii. dislocation densities in some annealed and cold-worked metals from measurements on the x-ray debye-scherrer spectrum," *Philosophical magazine*, vol. 1, no. 1, pp. 34–46, 1956.

[39] S. Murugesan *et al.*, "X-ray diffraction rietveld analysis of cold worked austenitic stainless steel," *Materials letters*, vol. 67, pp. 173–176, 2011.

[40] G. K. Williamson and R. E. Smallman, "X-ray line broadening from filed aluminium and wolfram," *Acta Metallurgica*, vol. 1, no. 1, pp. 22–31, 1953.

[41] J. Gallet *et al.*, "Experimental measurement of dislocation density in metallic materials: A quantitative comparison between measurements techniques (xrd, r-ecci, hr-ebsd, tem)," *Materials Characterization*, vol. 199, 2023.

[42] S. International, "Categorization and properties of dent resistant, high strength, and ultra high strength automotive sheet steel j2340," Warrendale, 1999.

[43] W. Kenny *et al.*, "Development of ultra-high strength galvanized steel for automotive bumper reinforcements," *SAE Transactions*, vol. 94, pp. 681–689, 1985. (visited on 08/07/2022).

[44] P. Lake and J. Grenawalt, "Partially annealed high strength cold rolled steels," *SAE Transactions*, vol. 86, pp. 718–729, 1977. (visited on 08/07/2022).

[45] C. Adams and W. Williams, "The partial annealing of low-carbon steel strip," *Canadian Metallurgical Quarterly*, vol. 9, no. 3, pp. 475–484, 1970.

[46] J. D. Messemaeker, B. Verlinden, and J. V. Humbeeck, "Structural evolution of if steel during annealing after ecap," *Materials Science Forum*, vol. 467–470, pp. 1295–1300, 2004.

[47] M. S. Devgun, S. Garber, and J. F. Hill, "Mechanical and magnetic properties of partially annealed low-carbon mild steel sheet," *Metals Technology*, vol. 11, pp. 369–370, 1984.

[48] G. Marx, "Quantitative microstructural evaluation of 12cr creep aged steels after welding," 2016.

[49] D. Balzar *et al.*, "Size-strain line-broadening analysis of the ceria round-robin sample," *Applied Crystallography*, vol. 37, pp. 911–924, 2004.

[50] N. I. of Standards and Technology, "Line position and line shape standard for powder diffraction (lanthanum hexaboride powder)," 2015.

[51] J. Perl *et al.*, "Topas: An innovative proton monte carlo platform for research and clinical applications," *Medical Physics*, vol. 39, pp. 6818–6837, 2012.

[52] V. Soleimanian and M. Mojtahedi, "A comparison between different x-ray diffraction line broadening analysis methods for nanocrystalline ball-milled fcc powders," *Applied Physics A*, vol. 119 (3), pp. 977–987, 2015.

[53] F. Bachmann, R. Hielscher, and H. Schaeben, "Texture analysis with mtex – free and open source software toolbox," *Solid State Phenomena*, vol. 160, pp. 63–68, 2010.

[54] R. Hielscher and H. Schaeben, "A novel pole figure inversion method: Specification of the mtex algorithm," *Applied Crystallography*, vol. 41, pp. 1024–1037, 2008.

[55] F. Bachmann, R. Hielscher, and H. Schaeben, "Grain detection from 2d and 3d ebsd data—specification of the mtex algorithm," *Ultramicroscopy*, vol. 111, pp. 1720–1733, 2011.

[56] I. O. of Standardization, "Steel - converstion of elongation values - part1: Carbon and low alloy steels," 1999.

[57] "Efunda." (2024), [Online]. Available: `https://www.efunda.com/units/hardness/convert_hardness.cfm?HD=Approx%2E%20TS&Cat=Steel#ConvInto`.

[58] R. Maubane, "Internal report," Pretoria, 2020.

[59] M. Bellavoine *et al.*, "Modelling of recrystallization after hot deformation of aluminium," *Metallurgical and materials transactions A*, vol. 49A, pp. 2865–2875, 2018.

[60] K. Banks *et al.*, "Development of thin v-n microalloyed s355mh strip," Pretoria, 2023.

[61] M. Ferry, D. Muljono, and D. Dunne, "Recrystallization kinetics of low and ultra low carbon steels during high-rate annealing," *ISIJ International*, vol. 41, pp. 1053–1060, 2001.

[62] J. Steyn, "Internal report," Vanderbijlpark, 2021.

[63] W. H. Hall, "X-ray line broadening in metals," *Proceedings of the Physical Society. Section A*, vol. 62, no. 11, pp. 741–743, 1949.

Appendix

A Simulated annealing cycle details

Table A.1: Simulated annealing cycles detail for line-speeds 30, 110 and 120 m/min.

110 m/min		Cycle1		Cycle2		Cycle3		Cycle4		Cycle5		Cycle6		Cycle7		Cycle8		Cycle9	
Time (s)	Time Acc (s)	Heating Rate (C/s)	Temp (C)	Heating Rate (C/s)	Temp (C)	Heating Rate (C/s)	Temp (C)	Heating Rate (C/s)	Temp (C)	Heating Rate (C/s)	Temp (C)	Heating Rate (C/s)	Temp (C)	Heating Rate (C/s)	Temp (C)	Heating Rate (C/s)	Temp (C)	Heating Rate (C/s)	Temp (C)
0	0	0	25	0	25	0	25	0	25	0	25	0	25	0	25	0	25	0.0	25
9.1	9.1	85.6	800	80.1	750	74.5	700	71.8	675	69.0	650	63.5	600	60.7	575	58.0	550	52.5	500
30.5	39.6	-1.0	770	-1.0	720	-1.0	670	-1.0	645	-1.0	620	-1.0	570	-1.0	545	-1.0	520	-1.0	470
22.9	62.5	-12.4	485	-10.3	485	-8.1	485	-7.0	485	-5.9	485	-3.7	485	-2.6	485	-1.5	485	-0.4	460
30.5	93.1	0.0	485	0.0	485	0.0	485	0.0	485	0.0	485	0.0	485	0.0	485	0.0	485	0.0	460
4.4	97.4	-5.7	460	-5.7	460	-5.7	460	-5.7	460	-5.7	460	-5.7	460	-5.7	460	-5.7	460	0.0	460
30.5	128.0	-14.2	25	-14.2	25	-14.2	25	-14.2	25	-14.2	25	-14.2	25	-14.2	25	-14.2	25	-14.2	25

30 m/min		Cycle1		Cycle2		Cycle3		Cycle4		Cycle5		Cycle6		Cycle7		Cycle8		Cycle9	
Time (s)	Time Acc (s)	Heating Rate (C/s)	Temp (C)	Heating Rate (C/s)	Temp (C)	Heating Rate (C/s)	Temp (C)	Heating Rate (C/s)	Temp (C)	Heating Rate (C/s)	Temp (C)	Heating Rate (C/s)	Temp (C)	Heating Rate (C/s)	Temp (C)	Heating Rate (C/s)	Temp (C)	Heating Rate (C/s)	Temp (C)
0	0	0	25	0	25	0	25	0	25	0	25	0	25	0	25	0	25	0.0	25
33.2	33.2	23.3	800	21.8	750	20.3	700	19.6	675	18.8	650	17.3	600	16.6	575	15.8	550	14.3	500
112	145.2	-0.3	770	-0.3	720	-0.3	670	-0.3	645	-0.3	620	-0.3	570	-0.3	545	-0.3	520	-0.3	470
84	229.2	-3.4	485	-2.8	485	-2.2	485	-1.9	485	-1.6	485	-1.0	485	-0.7	485	-0.4	485	-0.1	460
112	341.2	0.0	485	0.0	485	0.0	485	0.0	485	0.0	485	0.0	485	0.0	485	0.0	485	0.0	460
16	357.2	-1.6	460	-1.6	460	-1.6	460	-1.6	460	-1.6	460	-1.6	460	-1.6	460	-1.6	460	0.0	460
112	469.2	-3.9	25	-3.9	25	-3.9	25	-3.9	25	-3.9	25	-3.9	25	-3.9	25	-3.9	25	-3.9	25

120 m/min		Cycle1		Cycle2		Cycle3		Cycle4		Cycle5		Cycle6		Cycle7		Cycle8	
Time (s)	Time Acc (s)	Heating Rate (C/s)	Temp (C)	Heating Rate (C/s)	Temp (C)	Heating Rate (C/s)	Temp (C)	Heating Rate (C/s)	Temp (C)	Heating Rate (C/s)	Temp (C)	Heating Rate (C/s)	Temp (C)	Heating Rate (C/s)	Temp (C)	Heating Rate (C/s)	Temp (C)
0	0	0	25	0	25	0	25	0	25	0	25	0	25	0	25	0	25
8.3	8.3	84.3	725	81.3	700	78.3	675	75.3	650	72.3	625	69.3	600	66.3	575	63.3	550
28	36.3	-1.1	695	-1.1	670	-1.1	645	-1.1	620	-1.1	595	-1.1	570	-1.1	545	-1.1	520
21	57.3	-10.0	485	-8.8	485	-7.6	485	-6.4	485	-5.2	485	-4.0	485	-2.9	485	-1.7	485
28	85.3	0.0	485	0.0	485	0.0	485	0.0	485	0.0	485	0.0	485	0.0	485	0.0	485
4	89.3	-6.3	460	-6.3	460	-6.3	460	-6.3	460	-6.3	460	-6.3	460	-6.3	460	-6.3	460
28	117.3	-15.5	25	-15.5	25	-15.5	25	-15.5	25	-15.5	25	-15.5	25	-15.5	25	-15.5	25

B Wiliamson-Hall method XRD

As discussed in section 2.4.7 crystallite size and microstrain are required to estimate dislocation density. To obtain crystallite size and microstrain from XRD data the Wiliamson-Hall method was used [63]. Broadening of X-ray peak profiles when analysing metals is mainly the result of crystallite size, effective strain and instrumental effects. Other defects in the metal such as stacking faults also affect the peak breadths.

Using the Scherrer equation the peak line breadth β_P from crystallite size ϵ is related to x-ray wavelength λ and Bragg angle θ as follows:

$$\beta_P = \frac{K\lambda}{\epsilon \cos\theta} \tag{22}$$

K is a shape factor dependent on the shape of the crystals usually taken between 0.9-1. The breadth from pure stress β_S is related to effective strain η and Bragg angle as follows:

$$\beta_S = \eta \tan\theta \tag{23}$$

The breadths are additive, therefore $\beta = \beta_P + \beta_S$. Using $K = 0.9$ particle size ϵ and strain η was calculated from the XRD data. Using lattice parameter for α-iron as 0.286 nm to calculate b^2 and k as 14.4 the dislocation density was estimated using Equation 19.

C Crystallite size and microstrain data from XRD

Table C.1: Crystallite size and microstrain data obtained using XRD.

Sample	Line Speed	PMT (°C)	Average $HV_{0.5kg}$	$HV_{0.5kg}$ Std Dev	Time at max M (s)	M $(T+273)(\log t+20)$E-3	Crystallite size (LVol-IB) (nm)	Crystallite size Error (nm)	Strain (GS)	Strain (GS) Error	e0	ρ(m-2)
Low C-Mn-Nb-Ti_85CW	As CR	As CR	286	3	0	0.000	30.72091	0.39498	5E-04	2E-05	0.001054	1.05E+15
	110	500	318	3	18	16.430	44.44381	0.65776	3E-04	1E-05	0.000552	5.52E+14
	30	500	310	3	66	16.867	51.32958	0.66514	3E-04	1E-05	0.000478	4.78E+14
	110	550	311	6	18	17.493						
	30	550	310	10	66	17.957						
	110	650	288	3	18	19.619	61.46734	0.55206	2E-04	1E-05	0.000321	3.21E+14
	30	650	281	6	66	20.139	62.27244	0.63744	2E-04	1E-05	0.000309	3.09E+14
	110	675	279	6	18	20.150	74.62335	0.57368	1E-04	1E-05	0.000187	1.87E+14
	110	700	204	6	18	20.681						
	30	675	178	5	66	20.685						
	30	700	171	3	66	21.230						
	110	750	170	1	18	21.744						
	30	750	163	3	66	22.321						
	110	800	136	1	18	22.807						
	30	800	140	0	66	23.412	188.84179	3.53689	8E-05	0	6.6E-05	6.60E+13
	20	800	138	3	99	23.601						
Low C-Mn-V-N_85CW	As CR	As CR	269	2	0	0.000	40.56024	0.61215	6E-04	1E-05	8.35E-04	8.35E+14
	110	500	288	3	18	16.430	64.5679	0.58911	3E-04	1E-05	3.55E-04	3.55E+14
	30	500	272	5	66	16.867						
	110	550	275	3	18	17.493						
	30	550	275	4	66	17.957						
	110	575	273	2	18	18.024						
	30	575	268	1	66	18.503						
	110	600	267	2	18	18.556						
	30	600	271	2	66	19.048	88.71457	1.29238	3E-04	1E-05	0.00029	2.90E+14
	110	650	259	1	18	19.619	53.40072	0.57674	3E-04	1E-05	0.00046	4.60E+14
	30	650	247	5	66	20.139						
	110	675	210	9	18	20.150	94.49236	1.19256	3E-04	1E-05	0.000247	2.47E+14
	30	675	184	3	66	20.685	204.43029	2.4725	0	2E-05		
	110	700	170	1	18	20.681						
	30	700	151	0	66	21.230						
	110	750	146	2	18	21.744						
	30	750	142	0	66	22.321	78.56907	1.3931	9E-05	2E-05	0.000168	1.68E+14
	110	800	142	1	18	22.807	242.8184	4.89695	2E-04	0	7.48E-05	7.48E+13
	30	800	136	2	66	23.412	194.44582	11.68393	1E-04	1E-05	7.17E-05	7.17E+13
	20	800	133	1	99	23.601						
Low C-Mn_83CW	As CR	As CR	263	7	0	0.000						
	120	550	257	3	17	17.462						
	120	575	247	4	17	17.992						
	120	600	228	1	17	18.523						
	120	625	173	17	17	19.053						
	120	650	133	2	17	19.584						
	120	675	129	1	17	20.114						
	120	700	127	1	17	20.645						
	120	725	128	1	17	21.175						

D The Johnson-Mehl-Avrami-Kolmogorov (JMAK) model derivation

Assuming that the nuclei form at rate of $\dot{N}$ and the grain growth rate is linear at a rate of $\dot{G}$. With time, the material's recrystallised fraction X_V increases rapidly initially until the grains start impinging on each other resulting in a decrease in recrystallisation rate as $X_V \longrightarrow 1$.

In a time interval dt, the actual number of nuclei appearing dN is less than $\dot{N}dt$, as nuclei cannot form in the already recrystallised regions. The "phantom" nuclei that would have appeared in the already recrystallised volume is $\dot{N}X_V dt$. The total number of nuclei dN' including the "phantom" nuclei is therefore:

$$dN' = \dot{N}dt = dN + \dot{N}X_V dt \tag{24}$$

If the "phantom" nuclei were real, the fraction material recrystallised would be X_{VEX}. If at time t the recrystallised volume fraction is V, then X_{VEX} which is also known as the extended volume is given by:

$$X_{VEX} = \int_0^t V dN' \tag{25}$$

Assuming the growth rate $\dot{G}$ is constant with time and the growth of a spherical nucleus with radius r occurred between a period $t - \tau$ where τ is the incubation time:

$$\dot{G} = \frac{dr}{dt} = \frac{r - 0}{t - \tau} \tag{26}$$

and

$$r^3 = \dot{G}^3(t - \tau)^3 \tag{27}$$

Assuming three-dimensional growth and incubation time much less than t

$$V = \frac{4}{3}\pi r^3 = f\dot{G}^3 t^3 \tag{28}$$

where $f = 4/3\pi$ and is known as the shape factor. Then for nuclei

$$X_{VEX} = f\dot{G}\int_0^t \dot{N}t^3 dt \tag{29}$$

Assuming $\dot{N}$ is constant

$$X_{VEX} = \frac{f\dot{G}\dot{N}t^4}{4} \tag{30}$$

In a time interval dt, extended volume increases by dX_{VEX}, and the fraction unrecrystallised material is $1 - X_V$. It follows that

$$dX_{VEX} = \frac{dX_V}{1 - X_V} \tag{31}$$

$$X = \int_0^{X_V} dX_{VEX} = \int_0^{X_V} \frac{dX_V}{1 - X_V} = \ln \frac{1}{1 - X_V} \tag{32}$$

$$X_V = 1 - \exp\left(-X_{VEX}\right) \tag{33}$$

Therefore:

$$X_V = 1 - \exp\left(-\frac{f\dot{N}\dot{G}t^4}{4}\right) \tag{34}$$

In a general form:

$$X = 1 - exp(-bt^n) \tag{35}$$

where X fraction recrystallised at time t and n the JMAK exponent, $b = f\dot{N}\dot{G}t^4/4$.

E MATLAB MTEX code used for EBSD analyses

```
% remove one pixel grains
[grains,ebsd.grainId] = calcGrains(ebsd('indexed'));
ebsd(grains(grains.grainSize<5)) = [];

% compute low angle and high angle boundaries
[grains,ebsd.grainId] = calcGrains(ebsd('indexed'),'threshold',[2*
   degree, 15*degree]);

% smooth the grain boundaries
grains = smooth(grains,5)

% plot the ebsd data and grain boundaries
plot(ebsd('indexed'),ebsd('indexed').orientations,'faceAlpha',0.5)
plot(grains.boundary,'linewidth',2)

% compute transparency from misorientation angle
alpha = grains.innerBoundary.misorientation.angle / (5*degree);

% plot the subgrain boundaries
plot(grains.innerBoundary,'linewidth',1.5,'edgeAlpha',alpha,'
   linecolor','b');

% compute the grain reference orientation deviation
grod = ebsd.calcGROD(grains);

% Calculate and plot grain orientation spread
GOS = grainMean(ebsd, grod.angle, grains);
plot(grains, GOS ./ degree)
mtexColorbar('title','GOS in degree')

% pole orientation plots
cs = ebsd('indexed').CS
h = [Miller(0,0,1,cs),Miller(1,0,1,cs),Miller(1,1,1,cs)];
plotPDF(ebsd('indexed').orientations,h,'antipodal')
```